



Contents lists available at ScienceDirect

# Journal of Rock Mechanics and Geotechnical Engineering

journal homepage: [www.jrmge.cn](http://www.jrmge.cn)

## Review

# Effect of H<sub>2</sub>S content on relative permeability and capillary pressure characteristics of acid gas/brine/rock systems: A review

Xiaoyan Zhang<sup>a,b</sup>, Qi Li<sup>a,b,\*</sup>, Mathias Simon<sup>c</sup>, Guodong Zheng<sup>d</sup>, Yongsheng Tan<sup>a,b</sup>

<sup>a</sup> State Key Laboratory of Geomechanics and Geotechnical Engineering, Institute of Rock and Soil Mechanics, Chinese Academy of Sciences, Wuhan, 430071, China

<sup>b</sup> University of Chinese Academy of Sciences, Beijing, 100049, China

<sup>c</sup> Department of Engineering, Durham University, Durham, DH1 3LE, UK

<sup>d</sup> Northwest Institute of Eco-Environment and Resources, Chinese Academy of Sciences, Lanzhou, 730000, China

## ARTICLE INFO

### Article history:

Received 22 June 2021

Received in revised form

18 January 2022

Accepted 15 March 2022

Available online 16 May 2022

### Keywords:

Acid gas geological sequestration

Relative permeability

Capillary pressure H<sub>2</sub>S content

Wettability Interfacial tension

## ABSTRACT

Geological storage of acid gas has been identified as a promising approach to reduce atmospheric carbon dioxide (CO<sub>2</sub>), hydrogen sulfide (H<sub>2</sub>S) and alleviate public concern resulting from the sour gas production. A good understanding of the relative permeability and capillary pressure characteristics is crucial to predict the process of acid gas injection and migration. The prediction of injection and redistribution of acid gas is important to determine storage capacity, formation pressure, plume extent, shape, and leakage potential. Herein, the existing experimental data and theoretical models were reviewed to gain a better understanding of the issue how the H<sub>2</sub>S content affects gas density, gas viscosity, interfacial tension, wettability, relative permeability and capillary pressure characteristics of acid gas/brine/rock systems. The densities and viscosities of the acid gas with different H<sub>2</sub>S mole fractions are both temperature- and pressure-dependent, which vary among the gas, liquid and supercritical phases. Water/acid gas interfacial tension decreases strongly with increasing H<sub>2</sub>S content. For mica and clean quartz, water contact angle increases with increasing H<sub>2</sub>S mole fraction. In particular, wettability reversal of mica to a H<sub>2</sub>S -wet behavior occurs in the presence of dense H<sub>2</sub>S. The capillary pressure increases with decreasing contact angle. At a given saturation, the relative permeability of a fluid is higher when the fluid is nonwetting. The capillary pressure decreases with decreasing interfacial tension at a given saturation. However, the existing datasets do not show a consistent link between capillary number and relative permeability. The capillary pressure decreases with increasing H<sub>2</sub>S mole fraction. However, there is no consensus on the effect of the H<sub>2</sub>S content on the relative permeability curves. This may be due to the limited availability of the relative permeability and capillary pressure data for acid gas/brine/rock systems; thus, more experimental measurements are required.

© 2022 Institute of Rock and Soil Mechanics, Chinese Academy of Sciences. Production and hosting by Elsevier B.V. This is an open access article under the CC BY-NC-ND license (<http://creativecommons.org/licenses/by-nc-nd/4.0/>).

## 1. Introduction

Global climate change due to anthropogenic greenhouse gas emissions, including carbon dioxide (CO<sub>2</sub>), is of a significant concern (Monastersky, 2013). Despite recent advances made in CO<sub>2</sub>-free renewable energy power generation technology (Ma et al., 2018), fossil fuels are likely to continue to play a major role in

energy production for many years, for example in China (Li et al., 2012a; Wei et al., 2021). CO<sub>2</sub> capture and storage can be used to reduce emissions to the atmosphere (Bachu, 2015).

As an increasing number of sour hydrocarbon reservoirs are being exploited worldwide, significant quantities of acid gas, primarily comprised of CO<sub>2</sub> and hydrogen sulfide (H<sub>2</sub>S), are being generated in gas processing plants (Shah et al., 2008a; Zhang et al., 2020). Acid gas injection and storage in geological formations are receiving increasing interest as a way of dealing with waste acid gas generated in exploitation of the sour hydrocarbon reservoirs. Acid gas injection is thought to have less environmental impact than that gas flaring does and is more effective than sulfur recovery (Bachu et al., 2003; British Columbia Geological Survey, 2003; Shah et al., 2008a). On one hand, acid gas injection into geological

\* Corresponding author. State Key Laboratory of Geomechanics and Geotechnical Engineering, Institute of Rock and Soil Mechanics, Chinese Academy of Sciences, Wuhan, 430071, China.

E-mail address: [qli@whrsm.ac.cn](mailto:qli@whrsm.ac.cn) (Q. Li).

Peer review under responsibility of Institute of Rock and Soil Mechanics, Chinese Academy of Sciences.

formations avoids the cost of desulfurization. On the other hand, injection of H<sub>2</sub>S with CO<sub>2</sub> is beneficial to avoid atmospheric emissions of noxious substances and mitigate the effects of global warming.

Successful geological sequestration of acid gas requires a good understanding of how the injected acid gas will interact with and displace the original pore fluids (Bachu and Carroll, 2005; Bennion and Bachu, 2006a, b, 2007). Displacement characteristics strongly control how the gas, liquid and aqueous phases are distributed and the extent to which the injected gas plume migrates and/or is trapped within the geological formation. The relative permeability and capillary pressure are two important characteristics used to describe the displacement process (Zhang et al., 2012; Pini and Benson, 2013) and are the essential input parameters for numerical models used to predict the effectiveness of the acid gas injection (Bennion and Bachu, 2005, 2006b; Shi et al., 2018).

Aside from CO<sub>2</sub>, significant amounts of H<sub>2</sub>S are presented in the acid gas stream stored in geological media. For example, in the acid gas injection projects in western Canada, the composition of the acid gas ranges from 2% H<sub>2</sub>S and 95% CO<sub>2</sub> to 83% H<sub>2</sub>S and 14% CO<sub>2</sub>, with the remaining acid gas being composed of hydrocarbon gases and water vapor. Varying the H<sub>2</sub>S content brings about changes in fluid properties and interactions between the rock, brine and acid gas. As the H<sub>2</sub>S content varies, the thermophysical properties of gas, including density and viscosity, can change significantly (Li and Yan, 2008). The H<sub>2</sub>S content also affects the interfacial tension (IFT) and wettability of the acid gas/brine/rock system (Herrick and Gaines, 1973; McCaffery and Bennion, 1974; Shah et al., 2008a, b; Broseta et al., 2012; Chen et al., 2018). The viscosity, IFT and wettability all have a strong control effect on the relative permeability and capillary pressure characteristics (Mungan, 1966; Lefebvre, 1973; McCaffery and Bennion, 1974; Craig, 1993; Bennion and Bachu, 2005, 2006b, c; Iglauer et al., 2015).

Theoretically, the capillary pressure and relative pressure characteristics depend on five factors: (i) interfacial properties, i.e. IFT and wettability, (ii) pore dimension and morphology, (iii) fluid properties, i.e. fluid viscosities ( $\mu_1$  and  $\mu_2$ ), (iv) temperature and pressure, and (v) external conditions, i.e. mean velocity ( $u$ ) or pressure gradient in the investigated zone (Thomeer, 1960; Lefebvre, 1973; Huang et al., 1997; Silin and Patzek, 2004).

In this article, we reviewed the existing experimental data and mathematical models to understand how the H<sub>2</sub>S content affects the relative permeability and capillary pressure characteristics. As the H<sub>2</sub>S content varies, the interfacial properties and fluid properties will change. Thus, the alterations of the interfacial characteristics of the acid gas/brine/rock system and thermophysical properties induced by changes in the H<sub>2</sub>S content, and how these alterations affect the relative permeability and capillary pressure characteristics are explored firstly. Next, the experimental study is critically examined to investigate the effects of the H<sub>2</sub>S content on the relative permeability and capillary pressure curves of acid gas/brine/rock systems.

## 2. Pressure and temperature conditions of acid gas injection projects

In addition to the fluid composition and rock characteristics, the relative permeability and capillary pressure characteristics that control the geological co-storage of CO<sub>2</sub> and H<sub>2</sub>S depend on the in situ conditions of pressure and temperature (Bachu and Bennion, 2008). To date, there are approximately 85 acid gas injection projects across the world, mostly in western Canada and the United States. In western Canada, approximately 48 projects have been approved to inject acid gas into geological formations (British Columbia Geological Survey, 2003; Bachu and Carroll, 2005;

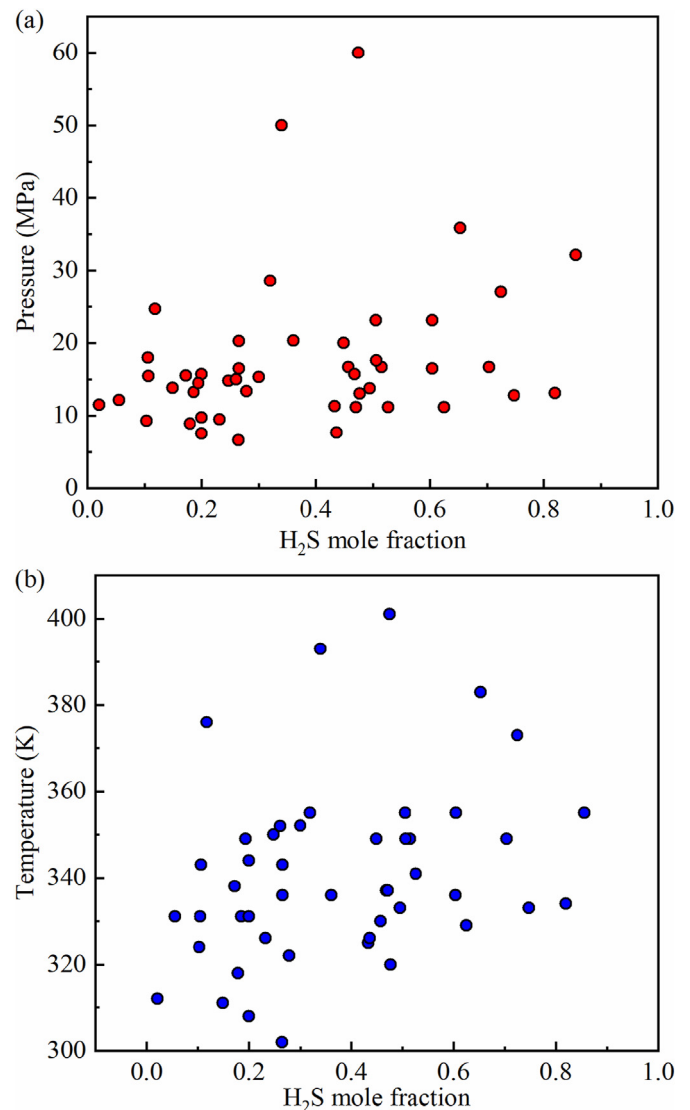


Fig. 1. The variation of (a) Pressure and (b) Temperature with H<sub>2</sub>S mole fraction in acid gas injection projects (Bachu and Carroll, 2005; Trivedi et al., 2005; Stopa et al., 2006; Smith et al., 2008; Jacquemet et al., 2012; Zhang et al., 2020).

Trivedi et al., 2005; Smith et al., 2008, 2009; Carroll et al., 2009). In the United States, the acid gas is injected into deep saline aquifers and depleted oil and/or natural gas reservoirs at nearly 30 sites (Klewicki et al., 2006). Furthermore, projects are being carried out in other prolific hydrocarbon places around the world, such as the Caspian Sea (Jacquemet et al., 2012), Qatar (Wu et al., 2014), Abu Dhabi (Miwa et al., 2002), Iceland (Alfredsson et al., 2013; Aradóttir et al., 2015; Clark et al., 2018, 2020) and Poland (Stopa et al., 2006). Currently, China's first acid gas injection project is in the feasibility study stage (Li et al., 2013; Zhang et al., 2020). Moreover, acid gas injection has broad application prospects in western China and Central Asia (Li et al., 2014; Zhang et al., 2021).

However, only 51 acid gas injection sites are fully characterized in terms of temperature, pressure, and composition (Bachu and Carroll, 2005; Trivedi et al., 2005; Stopa et al., 2006; Smith et al., 2008; Jacquemet et al., 2012; Alfredsson et al., 2013; Gunnarsson et al., 2013, 2018; Aradóttir et al., 2015; Clark et al., 2018., 2020; Zhang et al., 2020). Among them, three projects in Iceland, namely CarbFix 1, SulFix 1, and CarbFix 2, first dissolved acid gas in pure water and injected CO<sub>2</sub>–H<sub>2</sub>S charged water into basaltic sites. Thus,

only 48 cases of acid gas injection projects are presented here. As shown in Fig. 1, the H<sub>2</sub>S mole fraction in acid gas ranges from 2% to 83%. The projects cover pressures from 6.6 MPa to 60 MPa and temperatures from 302 K to 402 K.

### 3. Effect of H<sub>2</sub>S content on thermophysical properties of acid gas

The relative permeability and capillary pressure characteristics for the geological co-storage of CO<sub>2</sub> and H<sub>2</sub>S represent the interactions between the acid gas, reservoir rocks, and brine, which may be influenced by the thermophysical properties of the acid gas. Compared with pure CO<sub>2</sub>, the presence of H<sub>2</sub>S in the acid gas will change the thermophysical properties of the acid gas. In this section, we examined the impact of the H<sub>2</sub>S content on properties that can have substantial effects on the relative permeability and capillary pressure characteristics of acid gas/brine/rock systems.

Thermodynamic properties can be measured directly. However, due to the broad range of temperature, pressure, and H<sub>2</sub>S content encountered in the acid gas projects, experiments alone cannot satisfy the requirements of engineering applications. Therefore, theoretical models are often used to extrapolate these data. Herein, we reviewed both the experimental data and the theoretical models. The influence of the H<sub>2</sub>S mole fraction on its thermodynamic properties was then investigated.

#### 3.1. Phase diagram

In acid gas geological sequestration, it is usually desirable for the fluids to be in a supercritical state (Bachu, 2000; Yang et al., 2010). Under these pressure and temperature conditions, the acid gas has a high density like a liquid but moves like a gas, resulting in complete pore volume utilization and greater mobility within a reservoir. Hence, knowledge of pressure-temperature diagram for the CO<sub>2</sub>–H<sub>2</sub>S mixtures is essential.

For the pure CO<sub>2</sub> and H<sub>2</sub>S, the phase envelopes are the vapor pressure curves. Note that the vapor pressure of the pure CO<sub>2</sub> is greater than that of H<sub>2</sub>S (Fig. 2). For the CO<sub>2</sub>–H<sub>2</sub>S mixtures, the phase envelope is the combined loci of the bubble and dew points, which intersects at a critical point (Bierlein and Kay, 1953). The dew point curves and bubble point curves extend from the vapor pressure curve of CO<sub>2</sub> and terminate at the vapor pressure curve of H<sub>2</sub>S. The critical locus extends continuously from the critical point

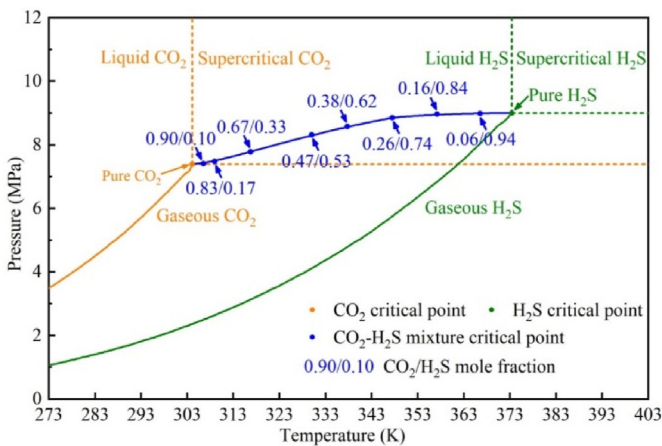


Fig. 2. Temperature-pressure diagram for a CO<sub>2</sub>–H<sub>2</sub>S system (Bierlein and Kay, 1953; Sobocinski and Kurata, 1959).

of CO<sub>2</sub> to that of H<sub>2</sub>S (Fig. 2). Based on the experimental data determined by Bierlein and Kay (1953), two regression curves were calculated to develop empirical correlations that could predict the critical pressure and temperature of a CO<sub>2</sub>–H<sub>2</sub>S mixture. The empirical correlations as functions of the H<sub>2</sub>S mole fraction can be derived as follows:

$$P_c = -4.7906x^3 + 6.6973x^2 - 0.5888x + 7.397 \quad (R^2 = 0.9996) \quad (1)$$

$$T_c = 42.75x^2 + 27.517x + 303.49 \quad (R^2 = 0.9997) \quad (2)$$

where  $P_c$  is the critical pressure (MPa),  $T_c$  is the critical temperature (K),  $x$  is the H<sub>2</sub>S mole fraction, and  $R^2$  is the determination coefficient. As shown in Fig. 3, a good agreement with the experimental data can be observed. At a given H<sub>2</sub>S mole fraction, the critical point of a binary mixture can be estimated to indicate the phase conditions in subsurface formations.

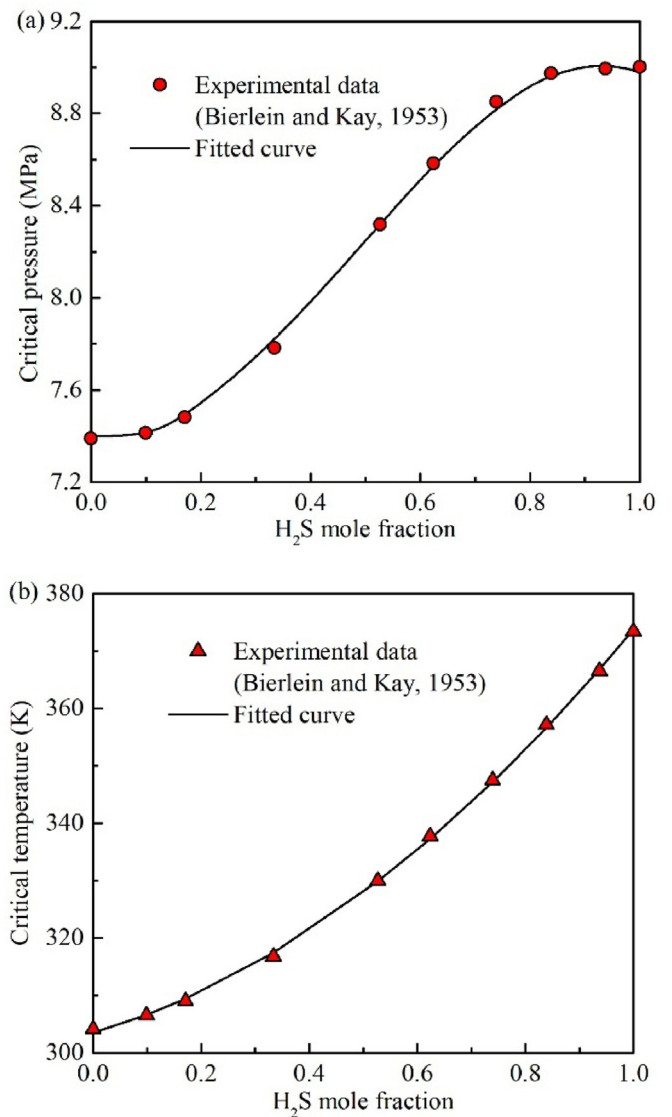


Fig. 3. Verification of proposed empirical correlations for (a) Critical pressure and (b) Critical temperature (Bierlein and Kay, 1953).

### 3.2. Density

Available experimental data of the density of the acid gas are summarized in Table 1, with the corresponding ranges in temperature, pressure, H<sub>2</sub>S content and fluid state. There are many available experimental data on pure CO<sub>2</sub> and H<sub>2</sub>S, covering a wide range of temperature and pressure conditions. However, considering the pressure and temperature conditions given in Fig. 1, there are large gaps between the available experimental data and the data requirements with respect to the density of CO<sub>2</sub>–H<sub>2</sub>S mixtures. Notably, the density measurements have added freedom as the H<sub>2</sub>S content can be varied, in contrast to the density measurements of pure CO<sub>2</sub> or H<sub>2</sub>S. As shown in Table 1, the experimental data for CO<sub>2</sub>–H<sub>2</sub>S mixtures are scarce. Only five binary mixtures of CO<sub>2</sub> and H<sub>2</sub>S are measured, and no experimental data are available for H<sub>2</sub>S mole fractions greater than 50%. Furthermore, most of the density data were measured at pressures below 25 MPa.

Based on the available experimental data, the development of theoretical models to predict the thermophysical properties of acid gas has progressed over the past years. The theoretical model for the gas density, i.e. the equation of state (EOS), is a mathematical relation connecting the volume, pressure, temperature, and H<sub>2</sub>S content of the acid gas. The reliabilities of EOSs for CO<sub>2</sub>–H<sub>2</sub>S mixtures vary for different gas properties and components and environmental conditions (Li and Yan, 2009a, b). Li et al. (2011) and Munkejord et al. (2016) reviewed the theoretical models associated with the thermophysical properties of CO<sub>2</sub> mixtures.

The EOSs of CO<sub>2</sub>–H<sub>2</sub>S mixtures can be classified into families according to their origin: the van der Waals family of cubic equations, such as the Redlich-Kwong (RK) EOS (Redlich and Kwong, 1949), Redlich-Kwong-Soave (SRK) EOS (Soave, 1972), Peng-Robinson (PR) EOS (Peng and Robinson, 1976), modified SRK (SRK-Peneloux) EOS (Pénéroux et al., 1982), Patel-Teja (PT) EOS (Patel and Teja, 1982), and Duan96 EOS (Duan et al., 1996); and a

**Table 1**  
Experimental data of the density of acid gas.

Author	System	x <sub>H<sub>2</sub>S</sub> <sup>a</sup>	Number of points	Temperature (K)	Pressure (MPa)	Fluid state
Span and Wagner (1996)	CO <sub>2</sub>	0	5508	203–1273	0–800	Gas, liquid, supercritical
Lau et al. (1997)	CO <sub>2</sub>	0	44	240–350	1.6–34.5	Gas, liquid, supercritical
Lemmon and Span (2006)	CO <sub>2</sub>	0	734	203–473	0.1–99.8	Gas, liquid, supercritical
Mantilla et al. (2010)	CO <sub>2</sub>	0	49	310–450	1–160	Gas, supercritical
Giri et al. (2011)	CO <sub>2</sub>	0	28	273–423	1–100	Gas, liquid, supercritical
Zhang et al. (2014)	CO <sub>2</sub>	0	303	308–470	1–160	Gas, supercritical
Stouffer et al. (2001)	CO <sub>2</sub> –H <sub>2</sub> S	0.4999	226	220–450	0.1–22.4	Gas, liquid, supercritical
		0.2933	189	230–400	0.1–24.2	Gas, liquid, supercritical
		0.0955	196	230–350	0.1–21.1	Gas, liquid, supercritical
		0.0607	251	220–450	0.1–23.7	Gas, liquid, supercritical
Nazeri et al. (2016)	CO <sub>2</sub> –H <sub>2</sub> S	0.0495	456	273–353	0.3–40.7	Gas, liquid, supercritical
Sakoda and Uematsu (2004)	H <sub>2</sub> S	1	1274	273–548	0.1–171	Gas, liquid, supercritical
Giri et al. (2011)	H <sub>2</sub> S	1	14	373–423	1–75	Gas

<sup>a</sup> Mole fraction.

**Table 2**

Performances of different EOSs for the calculation of the properties of acid gas mixtures.

EOS	Year	Author	Temperature (K)/Pressure (MPa)/ x <sub>H<sub>2</sub>S</sub>	Accuracy (Average absolute deviation <sup>b</sup> , %)	
				Gas molar volume, V <sub>g</sub> <sup>c</sup>	Liquid molar volume, V <sub>l</sub> <sup>d</sup>
RK	1949	Li and Yan (2009b)	273–360/1.5–8.5/0.15–1	8.84	4.95
SRK	1972	Boyle and Carroll (2002)	250–450/0–20/0.06–0.5	0.51 (2.79 <sup>a</sup> )	9.23
		Li and Yan (2009b)	273–360/1.5–8.5/0.15–1	7.34	4.18
PR	1976	Boyle and Carroll (2002)	250–450/0–20/0.06–0.5	1.26 (2.76 <sup>a</sup> )	2.81
		Li and Yan (2009b)	273–360/1.5–8.5/0.15–1	4.71	3.03
SRK-Peneloux	1982	Boyle and Carroll (2002)	250–450/0–20/0.06–0.5	0.65 (2.89 <sup>a</sup> )	5.00
		Li and Yan (2009b)	273–360/1.5–8.5/0.15–1	4.26	4.97
PT	1982	Boyle and Carroll (2002)	250–450/0–20/0.06–0.5	1.02 (2.26 <sup>a</sup> )	2.16
		Li and Yan (2009b)	273–360/1.5–8.5/0.15–1	5.57	2.43
Duan96	1996	Duan et al. (1996)	<2000/<2500	(<2 <sup>a</sup> )	–

<sup>a</sup> In supercritical area.

<sup>b</sup> Average absolute deviation =  $\frac{\sum \text{abs}(\frac{M_{\text{cal}} - M_{\text{exp}}}{M_{\text{exp}}}) \times 100\%}{N}$ , where  $M_{\text{exp}}$  is the experimental data,  $M_{\text{cal}}$  is the calculated data, and  $N$  is the number of data point.

family of extended virial equations, such as the Benedict-Webb-Rubin (BWR) EOS.

The cubic EOSs have simple structures and reasonable accuracy and are popular in engineering applications. The reliabilities of the cubic EOSs have been evaluated for predicting the density of CO<sub>2</sub>–H<sub>2</sub>S mixtures (Duan et al., 1996; Boyle and Carroll, 2002; Li and Yan, 2009b). The performances of these EOSs are summarized in Table 2. The PR EOS and PT EOS are superior in calculation of the density of the acid gas in gas, liquid, and supercritical phases.

To investigate the impact of the H<sub>2</sub>S content on acid gas density, the PR EOS was chosen to calculate the densities of CO<sub>2</sub>–H<sub>2</sub>S mixtures in gas, liquid, and supercritical phases. Fig. 4a compares the densities of different CO<sub>2</sub>–H<sub>2</sub>S mixtures in the gas phase. Meanwhile, the densities of the CO<sub>2</sub>–H<sub>2</sub>S mixtures at temperatures of 380 K and 400 K were investigated. In the gas phase, the impact of the H<sub>2</sub>S content on CO<sub>2</sub>–H<sub>2</sub>S mixture density depends on the molecular weight. The molecular weight of H<sub>2</sub>S is lower than that of CO<sub>2</sub>, and thus the densities of CO<sub>2</sub>–H<sub>2</sub>S mixtures decrease with increasing H<sub>2</sub>S mole fraction (Li and Yan, 2008). However, it is apparent that the H<sub>2</sub>S mole fraction has little effect on the densities of the CO<sub>2</sub>–H<sub>2</sub>S mixtures. In addition, the mixtures' densities are considerably impacted by pressure, but they are only slightly impacted by temperature.

Fig. 4b shows the densities of different CO<sub>2</sub>–H<sub>2</sub>S mixtures in the liquid phase. The densities of the CO<sub>2</sub>–H<sub>2</sub>S mixtures at the temperatures of 380 K and 400 K were studied as well. In the liquid phase, the impact of the H<sub>2</sub>S content on the CO<sub>2</sub>–H<sub>2</sub>S mixtures' density depends on the molecular weight and phase envelope. When the temperature and pressure conditions approach the phase envelope, the density of the CO<sub>2</sub>–H<sub>2</sub>S mixture increases with increasing H<sub>2</sub>S mole fraction, as the acid gas transitions from a gas region to a liquid earlier with increasing H<sub>2</sub>S mole fraction. However, when the temperature and pressure conditions are far from the phase envelope, the density of the CO<sub>2</sub>–H<sub>2</sub>S mixture decreases with increasing H<sub>2</sub>S mole fraction due to the lower molecular

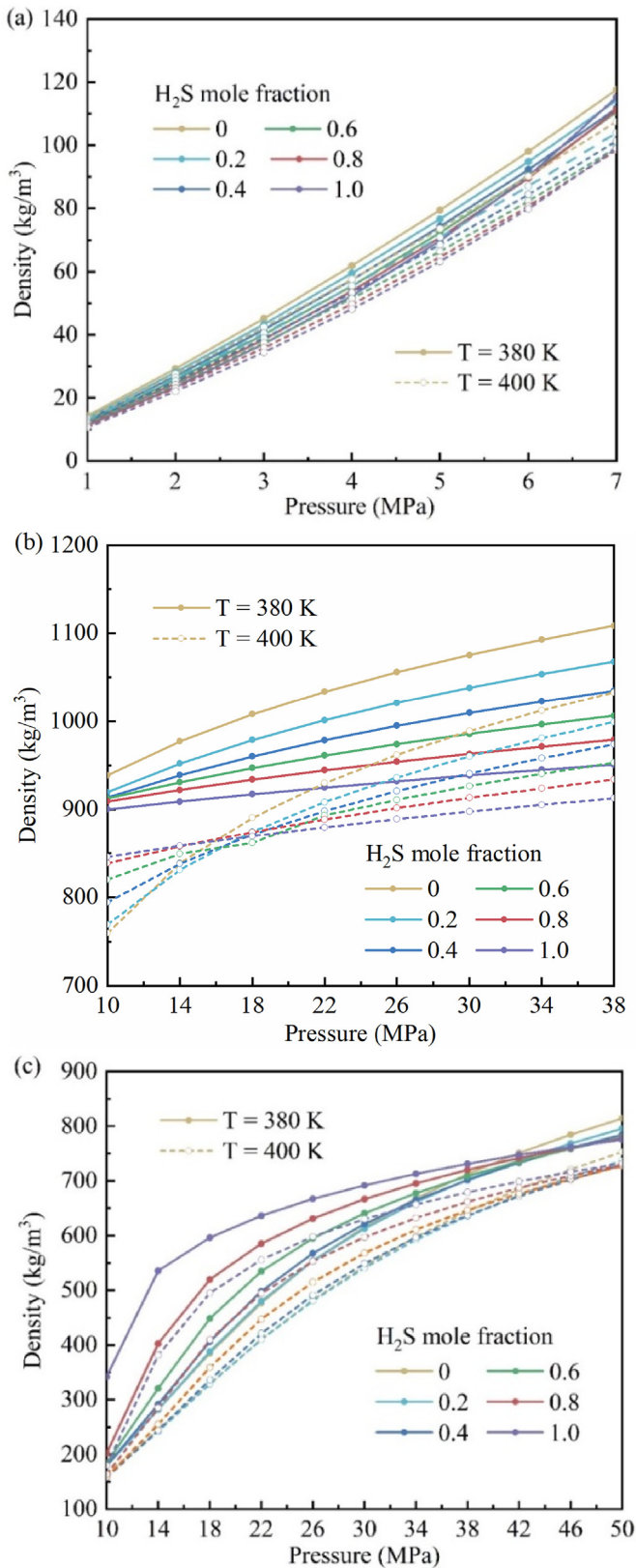


**Fig. 4.** Densities of CO<sub>2</sub>-H<sub>2</sub>S mixtures (a) in the gas phase, (b) in the liquid phase, and (c) in the supercritical phase.

weight of H<sub>2</sub>S. In addition, the mixtures' densities are only slightly impacted by the pressure, but they are considerably impacted by temperature.

Fig. 4c shows the densities of different CO<sub>2</sub>-H<sub>2</sub>S mixtures in the supercritical phase. The densities of CO<sub>2</sub>-H<sub>2</sub>S mixture at temperatures of 380 K and 400 K were studied as well. The trends of the CO<sub>2</sub>-H<sub>2</sub>S mixture densities in the supercritical phase are quite similar to those in liquid phase. The only difference is that the densities of the mixtures in the supercritical phase are significantly impacted by pressure and temperature.

### 3.3. Viscosity

A comprehensive database of the experimental data for the viscosity of the pure CO<sub>2</sub> was collected by Laesecke and Muzny (2017). Numerous measurements have been carried out since Graham's first experiments in 1864. However, the experimental data before 1957 are not accurate owing to the unavailability of accurate instruments and the lack of full working equations for the instruments employed (Fenghour et al., 1998). Furthermore, there is a wide gap at the pressure from 0.5 MPa to approximately 700 MPa and the temperature above 550 K. The data for the pure CO<sub>2</sub> are relatively sparse, and the data for the pure H<sub>2</sub>S is much more limited. As indicated by Schmidt et al. (2008) and Quiñones-Cisneros et al. (2012), the data for the viscosity of H<sub>2</sub>S are limited, and only 139 data points have been published. In addition, the majority of the data are for gaseous H<sub>2</sub>S and saturated liquid. Unfortunately, no data have been collected for the CO<sub>2</sub>-H<sub>2</sub>S mixtures either in liquid phase or vapor/supercritical phase.

Models for the viscosity of pure CO<sub>2</sub> were developed by Fenghour et al. (1998), covering the temperature from 200 K to 1500 K and the pressure up to 300 MPa. However, the Span-Wagner EOS, which is regarded as the reference equation for CO<sub>2</sub>, was not part of the correlation. Additionally, several experimental datasets have been published since the correlation of Fenghour et al. (1998), and correlation methodology has been advanced with a theory-based representation of the temperature dependence of the second viscosity virial coefficient. Consequently, Laesecke and Muzny (2017) developed a more accurate correlation, which covers the temperature from 100 K to 2000 K for gaseous CO<sub>2</sub> and from 220 K to 700 K with pressure along the melting line up to 8000 MPa in the compressed and supercritical liquid states. For the viscosity of H<sub>2</sub>S, the friction theory has been used (Schmidt et al., 2008) and then is revised (Quiñones-Cisneros et al., 2012) in an attempt to develop a reference model. The viscosity of the CO<sub>2</sub>-H<sub>2</sub>S mixtures can be described by empirical, multiparameter corresponding state correlations. An example is the procedure proposed by Chung et al. (1984, 1988), which is applicable to a wide range of polar and nonpolar fluids.

To investigate the impact of the H<sub>2</sub>S content on the viscosity, WebGasEOS (Matthew, 2006), which incorporates the correlations developed by Chung et al. (1984, 1988), was used to calculate the viscosities of the CO<sub>2</sub>-H<sub>2</sub>S mixtures in gas, liquid and supercritical phases. In addition, the PR EOS was selected to determine the thermodynamic properties.

The results of the viscosities of the CO<sub>2</sub>-H<sub>2</sub>S mixtures in gas, liquid and supercritical phases are illustrated in Fig. 5. In the gas phase, the viscosity of the CO<sub>2</sub>-H<sub>2</sub>S mixture decreases with increasing H<sub>2</sub>S mole fraction. However, in the liquid phase, the viscosity of the CO<sub>2</sub>-H<sub>2</sub>S mixture increases with increasing H<sub>2</sub>S mole fraction. Notably, a region exists where the viscosities of the CO<sub>2</sub>-H<sub>2</sub>S mixtures with different H<sub>2</sub>S mole fractions are approximately the same in the supercritical phase. This is because there is no clear transition from the gas phase to the supercritical region, and the CO<sub>2</sub>-H<sub>2</sub>S mixtures pass through the transition without discontinuities in the viscosities.

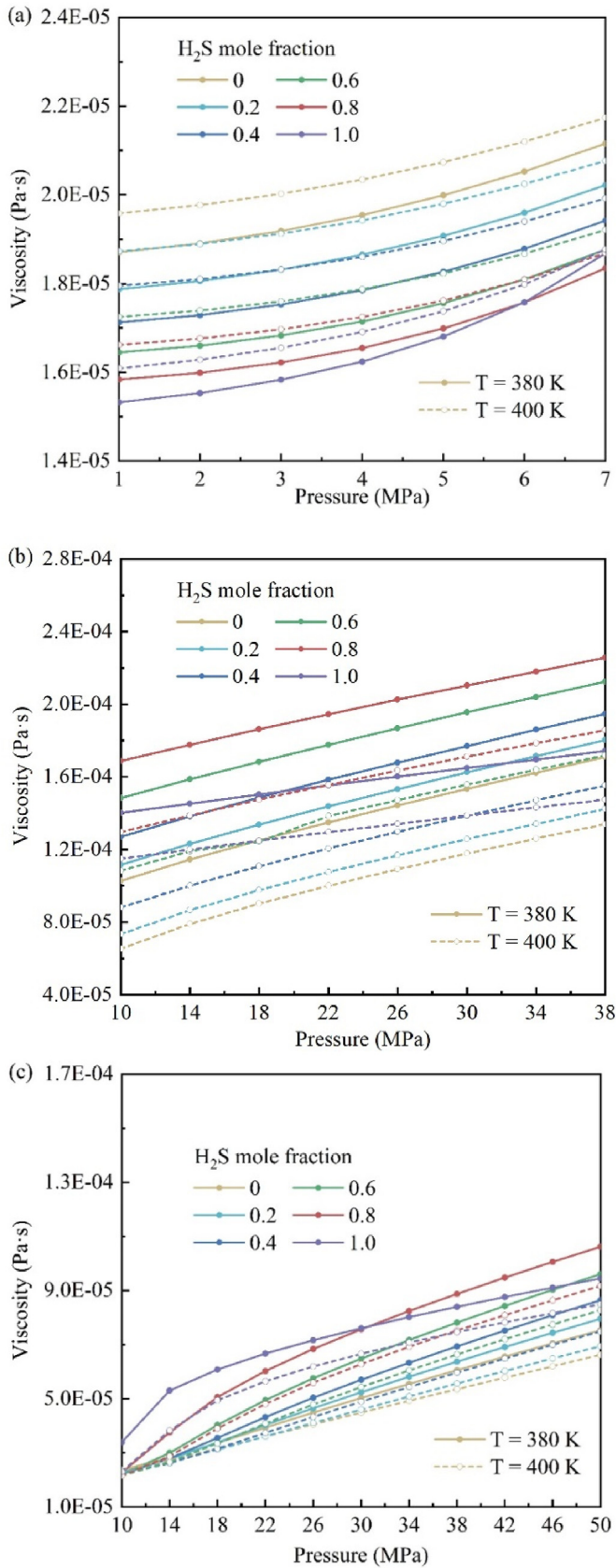


Fig. 5. Viscosities of CO<sub>2</sub>–H<sub>2</sub>S mixtures (a) in the gas phase, (b) in the liquid phase, and (c) in the supercritical phase.

#### 4. Effect of the H<sub>2</sub>S content on the interfacial properties of the acid gas/brine/rock system

Following acid gas injection into a reservoir, the acid gas and brine coexist within the pore space and a discontinuity in pressure is observed across the interface that separates the two fluid phases. This pressure jump is termed the capillary pressure. The relative permeability of a fluid is defined as the ratio of the effective permeability of that fluid to the absolute permeability, which is a direct measure of the ability to conduct one fluid when one or more fluids are presented in a porous system. The interfacial characteristics of the acid gas/brine/rock system, i.e. the IFT and wettability, play an important role in the control of the location, flow rate, and spatial distribution of fluids. Therefore, in order to investigate the relative permeability and capillary pressure characteristics of the acid gas/brine/rock system more accurately, it is necessary to better understand the interfacial characteristics of the acid gas/brine/rock system. Furthermore, as the H<sub>2</sub>S content varies, the interactions between the rock, brine and acid gas can change significantly. Thus, we examined the impact of the H<sub>2</sub>S content on the IFT and wettability of the acid gas/brine/rock system. In addition, the effects of the IFT and wettability on the relative permeability and capillary pressure characteristics were examined.

##### 4.1. Interfacial tension

###### 4.1.1. Effect of the H<sub>2</sub>S content on IFT

The IFT of CO<sub>2</sub>/water system has been studied intensively (e.g. Hebach et al., 2002; Chiquet et al., 2007a; Kvamme et al., 2007; Bennion and Bachu, 2008a; Bachu and Bennion, 2009b, c; Georgiadis et al., 2010; Bikkina, 2011). Fig. 6 shows the experimental IFT data for a pure CO<sub>2</sub>/water system. The experimental results reveal that along a given isotherm, the IFT decreases steeply with increasing pressure at low pressures. At high pressures, the IFT decreases gradually with increasing pressure, ultimately reaching a pseudo-plateau. The IFT isobars shown in Fig. 6b illustrate that at the critical temperature (304 K), the IFT first decreases and then increases with increasing temperature.

For a pure H<sub>2</sub>S/water system, the IFT data have also been reported (e.g. Herrick and Gaines, 1973; Strathdee and Given, 1976; Shah et al., 2008a), as shown in Fig. 7. The evolution of the H<sub>2</sub>S/water IFT with pressure and temperature is similar to that for CO<sub>2</sub>/water systems. At low pressures, the H<sub>2</sub>S/water IFT decreases with increasing pressure. At high pressures, the H<sub>2</sub>S/water IFT does not vary significantly with increasing pressure, and ultimately, an IFT pseudo-plateau is reached. The pseudo-plateau value of a H<sub>2</sub>S/water system is lower than that of a CO<sub>2</sub>/water system.

For practical purposes, a Taylor series polynomial regression analysis was used to describe the variation in the IFT with temperature and pressure (Herrick and Gaines, 1973; Strathdee and Given, 1976; Li et al., 2012b; Mutailipu et al., 2019). Based on the available experimental IFT data discussed above, the empirical correlations to predict the IFT for the CO<sub>2</sub>/water and H<sub>2</sub>S/water systems can be derived as follows:

$$\sigma = a_1 + b_1 P_r + b_2 T_r + c_1 P_r^2 + c_2 P_r T_r + c_3 T_r^2 + d_1 P_r^3 + d_2 P_r^2 T_r + d_3 P_r T_r^2 + d_4 T_r^3 + e_1 P_r^4 + e_2 P_r^3 T_r + e_3 P_r^2 T_r^2 + e_4 P_r T_r^3 + e_5 T_r^4 \quad (3)$$

where  $\sigma$  is the IFT (mN/m);  $T_r = T/T_C$  and  $P_r = P/P_C$  are the relative temperature and pressure, respectively. The coefficients  $a_1, b_1, b_2, c_1, c_2, c_3, d_1, d_2, d_3, d_4, e_1, e_2, e_3, e_4,$  and  $e_5$  and the determination coefficient  $R^2$  are evaluated by the Levenberg Marquardt iteration

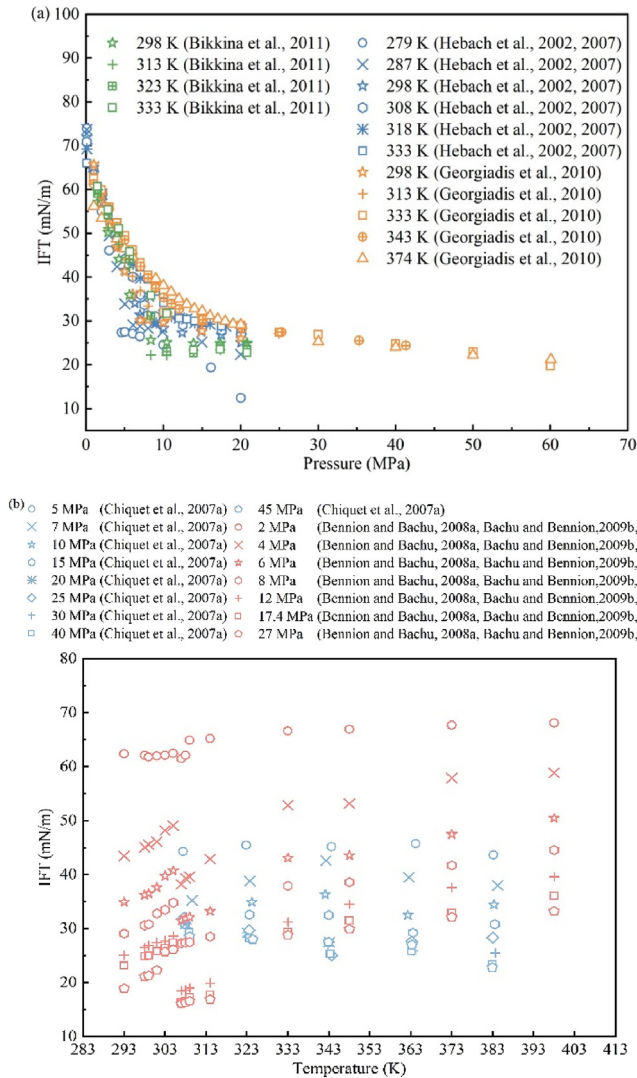


**Fig. 6.** (a) Experimental IFT data of CO<sub>2</sub>/water systems as a function of pressure (Hebach et al., 2002; Kvamme et al., 2007; Georgiadis et al., 2010; Bikkina et al., 2011), and (b) Experimental IFT data of CO<sub>2</sub>/water systems as a function of temperature (Chiquet et al., 2007a; Bennion and Bachu, 2008a; Bachu and Bennion, 2009b, c).

algorithm. The values of  $a_1, b_1, b_2, c_1, c_2, c_3, d_1, d_2, d_3, d_4, e_1, e_2, e_3, e_4, e_5,$  and  $R^2$  are listed in Table 3.

For the IFT between the water and the CO<sub>2</sub>–H<sub>2</sub>S mixture, a significant reduction in the acid gas/water IFT was observed in the presence of H<sub>2</sub>S (Chen et al., 2018). Bennion and Bachu (2006a) attributed the decrease in the capillary pressure of H<sub>2</sub>S/brine system to the lower IFT of H<sub>2</sub>S/brine system. Compared to that of a CO<sub>2</sub>/brine system, Bachu and Bennion (2009a) and Bachu et al. (2009) suggested that the gas relative permeability with a high concentration of H<sub>2</sub>S was high due to the low IFT between brine and acid gas with a high H<sub>2</sub>S content.

Furthermore, the IFTs between the water and the 70 mol% CO<sub>2</sub> + 30 mol% H<sub>2</sub>S mixture at 350 K were measured at different pressures by Shah et al. (2008a). As shown in Fig. 8, it is observed that the pseudo-plateau value of the water/(70 mol% CO<sub>2</sub> + 30 mol% H<sub>2</sub>S) mixture is proportional to the CO<sub>2</sub> (or H<sub>2</sub>S) mole fraction in the acid gas at a similar temperature and pressure:

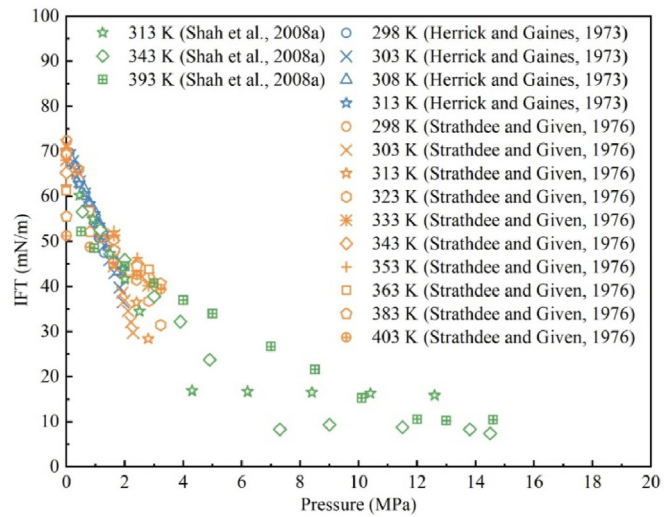


**Fig. 7.** Experimental IFT data of H<sub>2</sub>S/water systems as a function of pressure (Herrick and Gaines, 1973; Strathdee and Given, 1976; Shah et al., 2008a).

**Table 3**  
Coefficients of the regression model.

Coefficients for CO <sub>2</sub> /water systems ( $R^2 = 0.91673$ )					
Parameter	Value	Parameter	Value	Parameter	Value
$a_1$	3592.81	$c_3$	20,350.253	$e_1$	0.14
$b_1$	70.36	$d_1$	-4.553	$e_2$	1.63
$b_2$	-13,912.32	$d_2$	-41.143	$e_3$	9.6
$c_1$	51.72	$d_3$	517.33	$e_4$	-166.17
$c_2$	-475.46	$d_4$	-13078.42	$e_5$	3118.54
Coefficients for H <sub>2</sub> S/water systems ( $R^2 = 0.98525$ )					
Parameter	Value	Parameter	Value	Parameter	Value
$a_1$	-1500.97	$c_3$	-11,916.29	$e_1$	-6.5
$b_1$	-5786.93	$d_1$	-179.82	$e_2$	203.04
$b_2$	7090.88	$d_2$	-2710.14	$e_3$	1060.3
$c_1$	1638.13	$d_3$	-16134.01	$e_4$	5467.88
$c_2$	16,400.56	$d_4$	8903.25	$e_5$	-2517.67

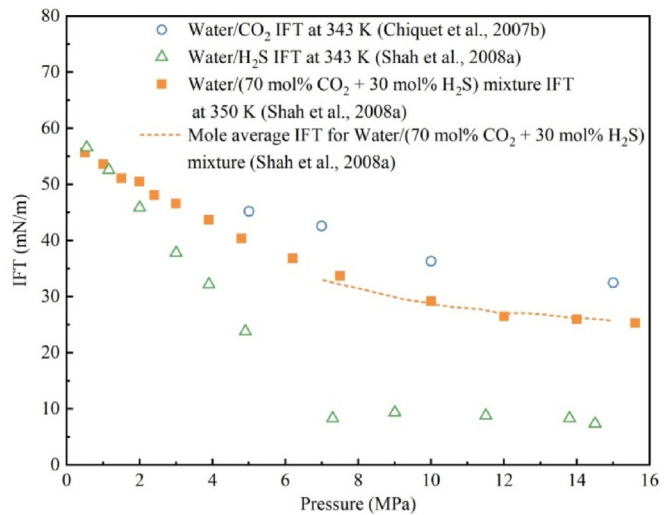


**Fig. 8.** Experimental IFT data between water and a 70 mol% CO<sub>2</sub> + 30 mol% H<sub>2</sub>S mixture at 350 K, water and H<sub>2</sub>S at 343 K, and water and CO<sub>2</sub> at 343 K, with the molar average IFT (dashed line) (i.e.  $0.7\sigma_{w,CO_2} + 0.3\sigma_{w,H_2S}$ ) (Shah et al., 2008a).

$$\sigma_{w,0.7CO_2+0.3H_2S} \approx 0.7\sigma_{w,CO_2} + 0.3\sigma_{w,H_2S} \quad (4)$$

#### 4.1.2. Effect of interfacial tension on relative permeability and capillary pressure characteristics

Interest in the effect of the IFT on the relative permeability characteristics has previously been driven by chemical flooding methods, whereby enhanced oil recovery is pursued by reducing the IFT between the aqueous phase and the reservoir oil. A number of studies have investigated the relative permeability of systems containing low-tension additives (e.g. Talash, 1976; Batychy and McCaffery, 1978; Amaefule and Handy, 1982; Harbert, 1983; Fulcher et al., 1985; Shen et al., 2010). Likewise, the relative permeability curves for high- and low-tension systems at the temperature ranging from 295 K to 448 K were obtained to understand the temperature effects in the thermal oil recovery process (Torabzadey and Handy, 1984). Furthermore, different IFTs were obtained by use of a solvent system to investigate the effect of IFT on the displacement of the wetting and nonwetting phases (Chukwudeme et al., 2014). In addition, different IFT magnitudes can be obtained by changing the composition of the gases or pressures of the experiments (Asar and Handy, 1988).

Bennion and Bachu (2005, 2006b, c) focused on the effect of the IFT on the CO<sub>2</sub>/brine systems of CO<sub>2</sub> injection into deep saline aquifers. They performed a series of controlled tests to investigate the effect of IFT on the relative permeabilities as CO<sub>2</sub> displaced brine.

The following concerns how the IFT affects the four important characteristics of the relative permeability and capillary pressure: (1) relative permeability nonlinearity, (2) residual saturation, (3) endpoint relative permeability, and (4) capillary pressure characteristics.

##### (1) Relative permeability nonlinearity

The effect of the IFT on the relative permeability nonlinearity has been intensively investigated (e.g. Talash, 1976; Batychy and McCaffery, 1978; Bardon and Longeron, 1980; Amaefule and Handy, 1982; Torabzadey and Handy, 1984; Asar and Handy, 1988; Bennion and Bachu, 2005, 2006b, c; Shen et al., 2010). However, consensus trends on between the IFT and the wetting or non-wetting relative permeability are rarely reported. Several studies report that both the wetting and nonwetting phase relative permeabilities increase with decreasing IFT (Talash, 1976; Asar and Handy, 1988; Bennion and Bachu, 2005, 2006b, c). However, other studies have found that such trends are unclear (Batychy and McCaffery, 1978; Amaefule and Handy, 1982). In some cases, a critical IFT value is proposed, below and above which the influences of the IFT on the relative permeability are very different (Bardon and Longeron, 1980; Torabzadey and Handy, 1984; Shen et al., 2010).

In some studies, it is reported that the relative permeability of both phases increase with decreasing IFT at a given water saturation (Talash, 1976; Asar and Handy, 1988; Bennion and Bachu, 2005, 2006b c). In the study of Talash (1976), four surfactants were used in crude oil/water systems to obtain various IFTs. Unfortunately, the IFT values, flow rates employed, and possible changes in the wettability of the cores were not reported. In contrast, the IFT values reported by Asar and Handy (1988) were ranging from 0.03 mN/m and 0.82 mN/m by changing the composition of the gas or pressure of the methane/propane system. As shown in Fig. 9, the curvatures of the relative permeability curves decreased as the IFT was reduced, and the irreducible gas and liquid saturations approached zero as the IFT approached zero.

Bennion and Bachu (2005, 2006b, c) focused on the CO<sub>2</sub>/brine system in CO<sub>2</sub> geological storage. In their studies, a series of IFT and relative permeability tests were conducted on core plugs sampled from the Wabamun Lake area, Alberta Basin, Canada, with the pressure, temperature and water salinity characteristics specific to each rock sample. A less pronounced trend of increasing the relative permeability with decreasing the IFT was reported. The weak dependency of the relative permeability was likely due to the high degree of variability in different rock samples. To verify the emerging pattern, Bennion and Bachu (2006b) further performed a series of controlled tests to investigate the IFT effect on the relative permeability of CO<sub>2</sub> as it displaces brine. The temperature and brine salinity of the CO<sub>2</sub>/brine system are 316 K and 27,096 ppm (parts per million), respectively. As shown in Fig. 10, the CO<sub>2</sub> and brine relative permeabilities increase with decreasing IFT at any given saturation. The correlation between the IFT and relative permeability was confirmed according to these results.

Batychy and McCaffery (1978) suggested that the effect of IFT on oil/brine (1 wt% NaCl) relative permeability was unclear. The effects of IFT on the drainage and imbibition relative permeability curves were obtained by steady-state methods in unconsolidated sand-packs at three IFT magnitudes. As shown in Fig. 11, the relative permeability to brine increases with decreasing IFT at any given saturation. However, the changes in oil relative permeability are complicated. Thus, IFT may not be a good predictor of the non-wetting phase permeability.

Amaefule and Handy (1982) also suggested that the effect of IFT on relative permeability was unclear. In their study, the effects of IFT on oil/brine (1 wt% NaCl) relative permeability in consolidated Berea sandstone cores were evaluated by unsteady- and steady-state displacement methods. Their results showed that the relative permeability to brine increases with decreasing IFT at any given saturation in both the unsteady- and steady-state displacement methods; however, the unsteady-state relative permeability data shows that the oil relative permeabilities decrease with decreasing IFT to a lesser extent. Conversely, the steady-state oil relative permeabilities increase with decreasing IFT.

In contrast to the abovementioned studies, Bardon and Longeron (1980) investigated a wide range of IFTs, including high IFTs (3.7 mN/m, 8.7 mN/m and 12.6 mN/m) and low IFTs, as of 0.001 mN/m. The IFT was controlled by varying the equilibrium

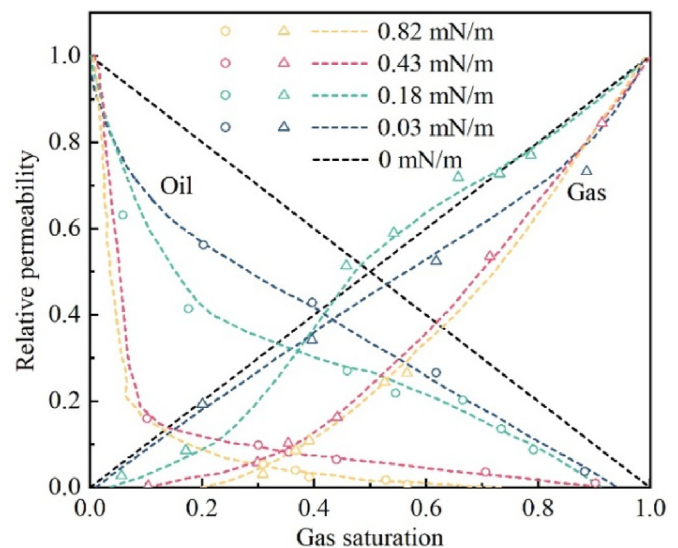


Fig. 9. Effects of IFT on imbibition gas/oil relative permeability curves (Asar and Handy, 1988).

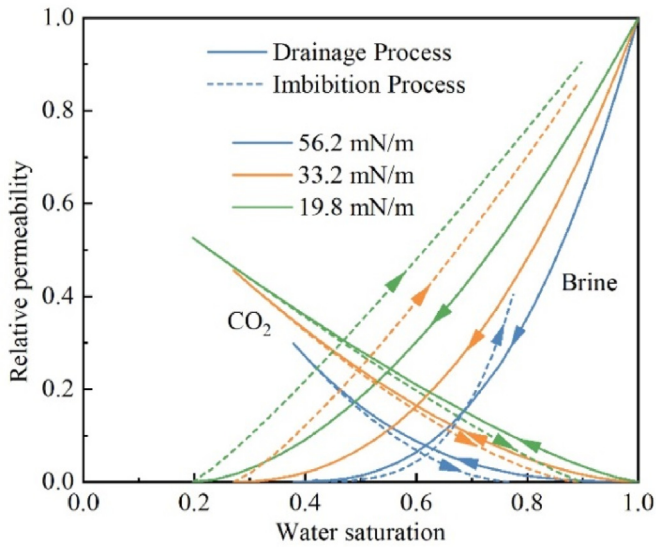


Fig. 10. Effects of IFT on CO<sub>2</sub>/brine relative permeability (Bennion and Bachu, 2006b).

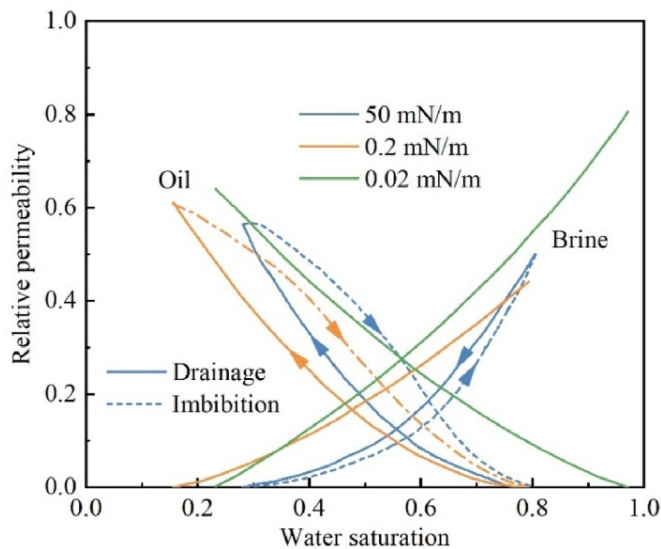


Fig. 11. Effects of IFT on drainage and imbibition relative permeability curves (Batychy and McCaffery, 1978).

pressure and thus the composition of the gas and oil mixtures under high-pressure and high-temperature conditions. It showed that when  $IFT \geq 0.04\text{--}0.07$  mN/m, the decrease in the IFT was not sufficient to change the vapor relative permeability, but the liquid relative permeability increased with decreasing IFT at any given saturation (Fig. 12a). In addition, they found a linear relation between the liquid relative permeability and IFT at a constant vapor saturation (Fig. 13). When  $IFT \leq 0.04\text{--}0.07$  mN/m, the relative permeability curves for both liquid and vapor considerably increased as the IFT decreased at any given saturation.

Torabzadey and Handy (1984) and Shen et al. (2010) also found that a crucial IFT value may exist below and above which the influences of the IFT on the relative permeability are very different. Note that the crucial IFT values were different in the two studies. Torabzadey and Handy (1984) reported that for the high-IFT system ( $IFT > 20$  mN/m), the oil's relative permeability increased, but the water's relative permeability decreased with decreasing IFT at any

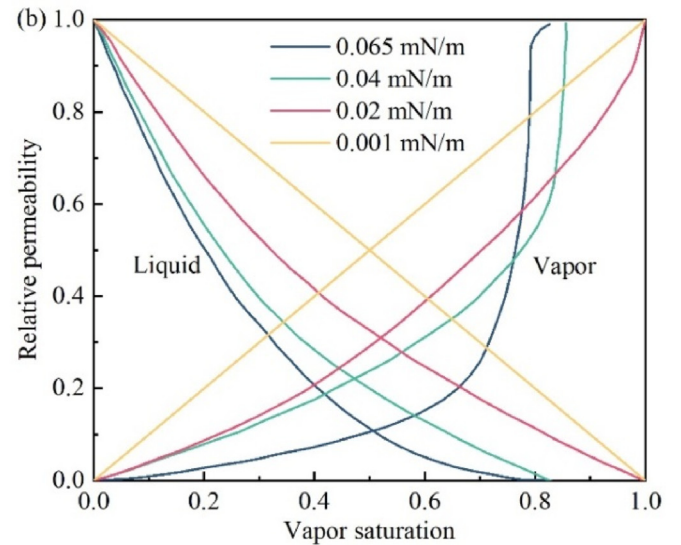
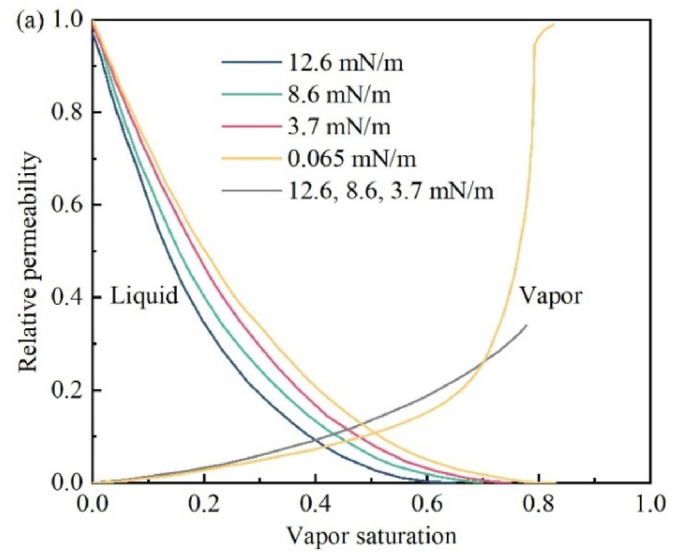


Fig. 12. Effects of IFT on drainage vapor/liquid relative permeability curves for (a) High IFTs and (b) Very low IFTs (Bardon and Longeron, 1980).

given saturation. For the low-IFT system (i.e.  $0.01$  mN/m  $< IFT < 0.19$  mN/m), the oil's relative permeability increased with decreasing IFT at any given saturation. The changes in water's relative permeability were complicated by the conflicting effects of increasing temperature on the wettability and IFT because the IFTs were obtained experimentally at the temperatures ranging from 295 K to 448 K. However, Shen et al. (2010) found that the resulting relative permeability curve trend was different when  $IFT < 3$  mN/m. IFT has little impact on the relative permeability of oil and water when  $IFT > 3$  mN/m. However, the relative permeability curve trend changed significantly with decreasing IFT when  $IFT < 3$  mN/m.

As discussed above, the relative permeability measurements have been conducted to investigate the effect of IFT on relative permeability characteristics (Talash, 1976; Batychy and McCaffery, 1978; Bardon and Longeron, 1980; Amaefule and Handy, 1982; Torabzadey and Handy, 1984; Asar and Handy, 1988; Shen et al., 2010). However, as shown in Table 4, only Shen et al. (2010) isolated the impact of IFT on relative permeability. The viscosity, flow velocity and viscosity ratio also change when the test conditions are changed to obtain different IFT magnitudes. Under these

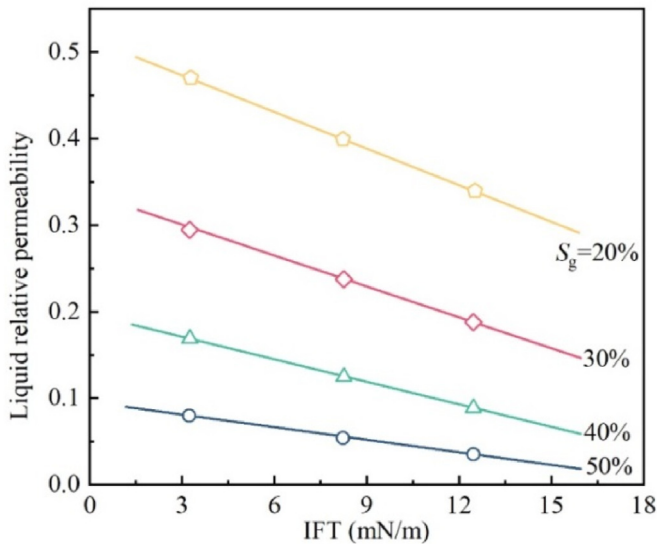


Fig. 13. Effects of IFT on liquid relative permeability for different vapor saturations (Bardon and Longeron, 1980).

circumstances, the capillary number ( $N_c$ ) is defined to characterize the flow behavior by combining the viscosity, flow velocity and IFT:

$$N_c = \frac{u\mu}{\sigma} \quad (5)$$

Table 4  
Summary of relative permeability test conditions.

System	$u$ (cm/h)	$\mu_1^a$ (mPa s)	$\mu_2^b$ (mPa s)	$\mu_1/\mu_2$	$\sigma$ (mN/m)	$N_c$	Source
N-decane/1 wt% NaCl brine	105	0.8336	0.8879	0.94	50	$4.87 \times 10^{-6}$ (drainage)	Batychy and McCaffery (1978)
						$5.18 \times 10^{-6}$ (imbibition)	
N-decane/1 wt% NaCl brine with 0.2 wt% TRS 10–80	40	0.8336	0.9079	0.92	0.2	$4.63 \times 10^{-4}$ (drainage)	
						$5.05 \times 10^{-4}$ (imbibition)	
N-octane/1 wt% NaCl brine with 0.2 wt% TRS 10–80	40	0.5008	0.9079	0.52	0.02	$2.78 \times 10^{-3}$ (drainage)	
						$5.05 \times 10^{-3}$ (imbibition)	
Dodecane/1 wt% NaCl brine	23.67	1.35	1.0544	1.28	34	$2.04 \times 10^{-6}$ (imbibition)	Amaefule and Handy (1982)
Dodecane/1 wt% NaCl brine with 1 wt% sec-butanol	23.67	1.35	0.9804	1.38	0.03	$2.15 \times 10^{-3}$ (imbibition)	
Dodecane/1 wt% NaCl brine with 1 wt% sec-butanol	23.67	1.4852	0.9910	1.5	0.01	$6.52 \times 10^{-3}$ (imbibition)	Asar and Handy (1988)
Methane/propane	N/A	N/A	N/A	0.29	0.82	N/A	
	N/A	N/A	N/A	0.39	0.43	N/A	
	N/A	N/A	N/A	0.55	0.18	N/A	
	N/A	N/A	N/A	0.85	0.03	N/A	Bardon and Longeron (1980)
C <sub>1</sub> -nC <sub>7</sub>	17.25	0.0128	0.208	0.062	12.6	$0.5 \times 10^{-7}$ (drainage)	
	19.52	0.0137	0.175	0.078	8.6	$0.86 \times 10^{-7}$ (drainage)	
	17.36	0.0159	0.122	0.13	3.7	$0.21 \times 10^{-6}$ (drainage)	
	20.20	0.0240	0.048	0.50	0.065	$0.19 \times 10^{-4}$ (drainage)	
	20.00	0.0260	0.046	0.56	0.04	$0.38 \times 10^{-4}$ (drainage)	
	18.10	0.0265	0.040	0.66	0.02	$0.65 \times 10^{-3}$ (drainage)	Torabzadey and Handy (1984)
	20.54	0.0270	0.037	0.73	0.001	$0.11 \times 10^{-2}$ (drainage)	
N-dodecane/salt solution	23.67	1.4250	0.9782	1.46	33.6	$1.92 \times 10^{-6}$ (imbibition)	Torabzadey and Handy (1984)
N-dodecane/salt solution	23.67	0.5270	0.2895	1.82	30.3	$6.29 \times 10^{-7}$ (imbibition)	
N-dodecane/salt solution	23.67	0.3352	0.1875	1.79	24.7	$5.00 \times 10^{-7}$ (imbibition)	
N-dodecane/salt solution	23.67	0.2752	0.1588	1.73	20.4	$5.12 \times 10^{-7}$ (imbibition)	
N-dodecane/surfactant solution	23.67	1.3300	0.8951	1.49	0.187	$3.15 \times 10^{-4}$ (imbibition)	
N-dodecane/surfactant solution	23.67	0.9520	0.5658	1.68	0.165	$2.26 \times 10^{-4}$ (imbibition)	
N-dodecane/surfactant solution	23.67	0.5270	0.2967	1.78	0.117	$1.67 \times 10^{-4}$ (imbibition)	
N-dodecane/surfactant solution	23.67	0.3352	0.1922	1.74	0.05	$2.53 \times 10^{-4}$ (imbibition)	
N-dodecane/surfactant solution	23.67	0.2752	0.1628	1.69	0.015	$7.14 \times 10^{-4}$ (imbibition)	
Oil/water	1.18	1	N/A	N/A	34.2	$4.15 \times 10^{-5}$ (drainage)	
Oil/water with surfactant					3.52	$4.12 \times 10^{-4}$ (drainage)	Shen et al. (2010)
Oil/water with surfactant					0.21	$6.91 \times 10^{-3}$ (drainage)	
Oil/water with surfactant					0.0114	$1.27 \times 10^{-1}$ (drainage)	

<sup>a</sup> Viscosity of the nonwetting phase.  
<sup>b</sup> Viscosity of the wetting phase.  
<sup>c</sup> Relative permeability test conditions in the steady-state tests.

where  $u$  is the flow velocity (m/s), and  $\mu$  is the viscosity of the displacing phase (Pa s).

According to Eq. (5), it shows that the  $N_c$  increases with decreasing IFT. Based on the results of Shen et al. (2010), it can be concluded that when the IFT effects are investigated individually, the effects of decreasing IFT on relative permeability are similar to those of increasing  $N_c$ . This conclusion has been proven by experimental results (Batychy and McCaffery, 1978; Bardon and Longeron, 1980), although viscosity and flow velocity are changed during experiments. However, according to the relative permeability measurements conducted by Amaefule and Handy (1982), Torabzadey and Handy (1984) and Asar and Handy (1988),  $N_c$  changes irregularly with decreasing IFT, due to the complicated changes in relative permeability with decreasing IFT. Thus, the IFT magnitude is inadequate to characterize the effects of IFT on relative permeability when viscosity and flow velocity also change.

In addition, Harbert (1983) presented the results of relative permeability tests using an alcohol, brine (130 kppm NaI and 13 kppm CaCl<sub>2</sub>), and oil fluid system in outcrop and reservoir rock samples. It was found that the relative permeability curves change with  $N_c$ , although the IFTs remain constant.

To determine the impact of the capillary number and its constituents, such as the flow velocity, fluid viscosity, and IFT, on the relative permeabilities, Fulcher et al. (1985) carried out a series of steady-state relative permeability measurements. They found that the nonwetting-phase (oil) and wetting-phase (water) relative permeabilities increased dramatically as the IFT decreased below 5.5 mN/m. As the water viscosity increased, the oil relative permeability decreased, approaching a linear relationship. However, the water relative permeability increased with increasing

water viscosity. The oil relative permeability showed little correlation with the capillary number. The increase in the capillary number, which is caused by a decrease in the IFT and an increase in the viscosity, leads to an increase in water relative permeability.

Based on the experimental results, Fulcher et al. (1985) developed a relative permeability model for both drainage and imbibition. For the relative permeabilities of oil (nonwetting-phase), it yields:

$$k_{ro(dr)} = 0.72899S^{*(1.2861+0.08043 \ln \sigma)} \left(\frac{\mu_w}{\mu_o}\right)^{-0.37932} \quad (6)$$

$$k_{ro(im)} = 1.56878S^{*[1.33874+0.09187 \ln \sigma+0.08528 \ln(\mu_w/\mu_o)]} \quad (7)$$

where  $k_r$  stands for relative permeability; the subscripts w and o stand for water and oil, respectively;  $S^*$  is a normalized variable based on the fluid saturation and the residual saturations. During the drainage process, it yields  $S^* = S_o$ . During the imbibition process, we have  $S^* = \frac{S_o - S_{or}}{1 - S_{or}}$ , where  $S_o$  is oil saturation, and  $S_{or}$  is residual oil saturation.

For the brine (wetting-phase) relative permeability, correlations are developed based on both individual variables and the capillary number:

$$k_{rw1(dr)} = 0.70216S^{*[1.25579-0.074482 \ln(\mu_w/\mu_o/\sigma)]} \quad (8)$$

$$k_{rw1(im)} = 0.61135S^{*[1.25875-0.070812 \ln(\mu_w/\mu_o/\sigma)]} \quad (9)$$

$$k_{rw2(dr)} = 0.7034S^{*(0.66596-0.071513 \ln N_c)} \quad (10)$$

$$k_{rw2(im)} = 0.61135S^{*(0.6958-0.068221 \ln N_c)} \quad (11)$$

where  $S^* = \frac{S_w - S_{wr}}{1 - S_{wr}}$ ,  $S_w$  is water saturation, and  $S_{wr}$  is residual water saturation.

The previous review of reported results reveals that there may exist a crucial IFT value below and above which the influences of the IFT on the relative permeability are very different. When the IFT is lower than the crucial IFT value, both the wetting- and nonwetting-phase relative permeabilities increase significantly with decreasing IFT. However, when the IFT is higher than the crucial IFT value, it has little impact on the relative permeability to the wetting and nonwetting phases. Notably, the viscosity, flow velocity and viscosity ratio may change when the test conditions are changed to obtain different IFT magnitudes. Furthermore, the gas and oil relative permeability curves approached a linear function of saturation as the IFT was reduced to zero. Notably, the effect of IFT on the relative permeability obtained by the steady-state method is far less than that on the curves measured by the unsteady-state method. The hysteresis effects in the relative permeability curves decrease and eventually disappear with decreasing IFT.

## (2) Residual saturation

According to Eq. (5), a reduction in IFT leads to an increase in the capillary number,  $N_c$ . To investigate the effect of IFT on residual saturation, the capillary desaturation curve which is a measure of residual saturation as a function of  $N_c$  was established. The typical capillary desaturation curves were reported by Lake (1989), as shown in Fig. 14. For both of the wetting and nonwetting phases, a critical capillary number,  $N_{cc}$ , exists in the capillary desaturation curves. The capillary desaturation curves plateau at the residual

saturation when  $N_c$  is below  $N_{cc}$ . When  $N_c$  is above  $N_{cc}$ , the residual saturation decreases with increasing  $N_c$ . The  $N_{cc}$  of the wetting phase is approximately 10 times that of the nonwetting phase (Gupta and Trushenski, 1979; Delshad et al., 1986). Several scholars have also reported no  $N_{cc}$  or a very low value of  $N_{cc}$  (Abrams, 1975; Garnes et al., 1990; Kamath et al., 2001). Nevertheless, the assumption of typical capillary desaturation curves is generally correct for a water-wet medium.

Fig. 15 compares a selection of the reported data from several different studies (Batycky and McCaffery, 1978; Harbert, 1983; Torabzadey and Handy, 1984) on the effect of the capillary number in residual saturation. Batycky et al. (1978) measured residual saturation levels as a function of capillary number,  $N_c$ , under the IFT values between 50 mN/m and 0.02 mN/m. Comparing with typical capillary desaturation curves reported by Lake (1989), a typical capillary desaturation curve was observed for the nonwetting phase (oil). However, the residual wetting-phase (water) saturation decreased with increasing  $N_c$  with no constant plateau.

Nevertheless, the experimental data reported by Harbert (1983) and Torabzadey and Handy (1984) are not consistent with the typical capillary desaturation curves reported by Lake (1989). Harbert (1983) reported a significant decrease in residual oil saturation with increasing  $N_c$  at the same IFT. However, no change in residual water saturation was observed with increasing  $N_c$ . Their results showed that both the residual water and oil saturations are determined by capillary number. Notably, a less permeable rock has a higher residual saturation if the capillary number does not change. Torabzadey and Handy (1984) found that residual water saturation for high  $N_c$  was lower than that for low  $N_c$ . A reduction in the residual oil saturation was also observed at  $N_c$  above  $10^{-4}$ .

By plotting the residual saturation against the capillary number,  $N_c$ , as shown in Fig. 16, the results obtained by Bardon and Longeron (1980) and Chukwudeme et al. (2014) confirmed that the capillary desaturation curves for the liquid phase and oil phase are consistent with the findings of Lake (1989). However, the water phase capillary desaturation curves for the three systems exhibited different trends. The residual water saturation decreased with increasing  $N_c$  and no critical capillary number was observed.

In particular, different IFT values (38.5 mN/m, 1.12 mN/m, and 0.09 mN/m for systems 1, 2, and 3, respectively) were obtained by three solvent systems in the context of Chukwudeme et al. (2014).

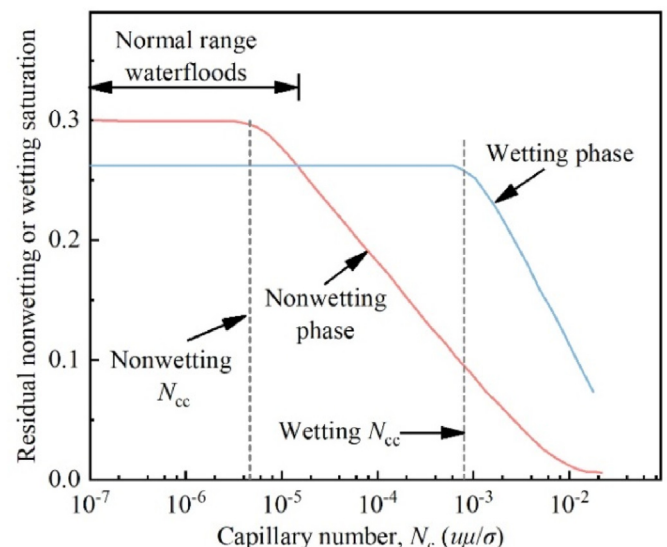


Fig. 14. Typical capillary desaturation curves (Lake, 1989).

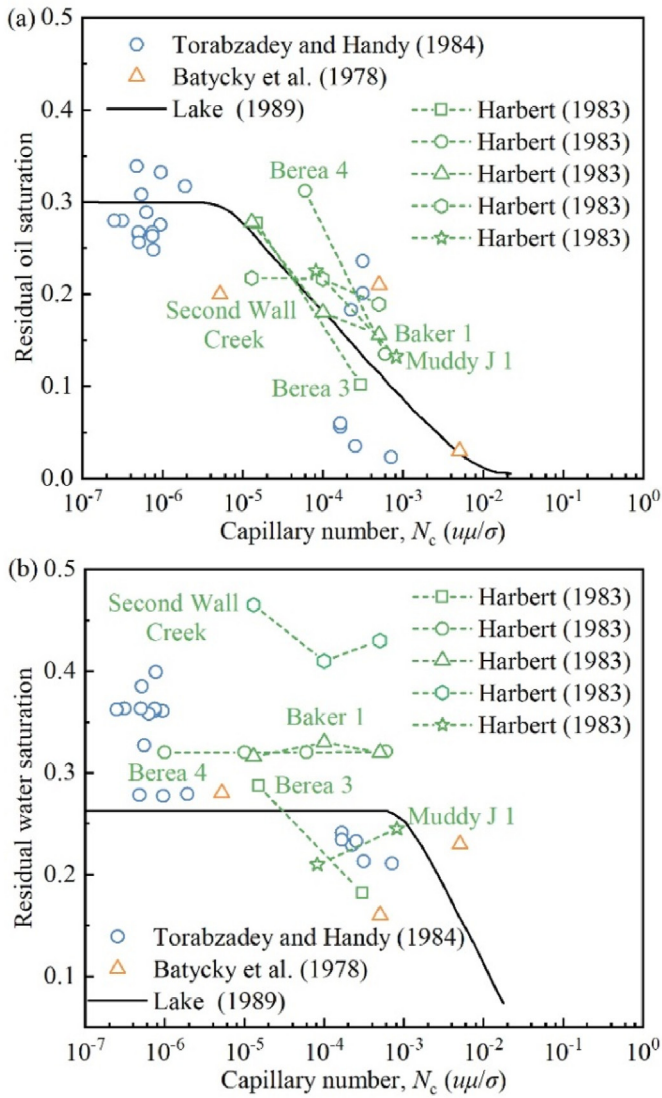


Fig. 15. Comparison of the variation in residual saturation with capillary number,  $N_c$ , in water/oil systems (Batycky and McCaffery, 1978; Harbert, 1983; Torabzadey and Handy, 1984).

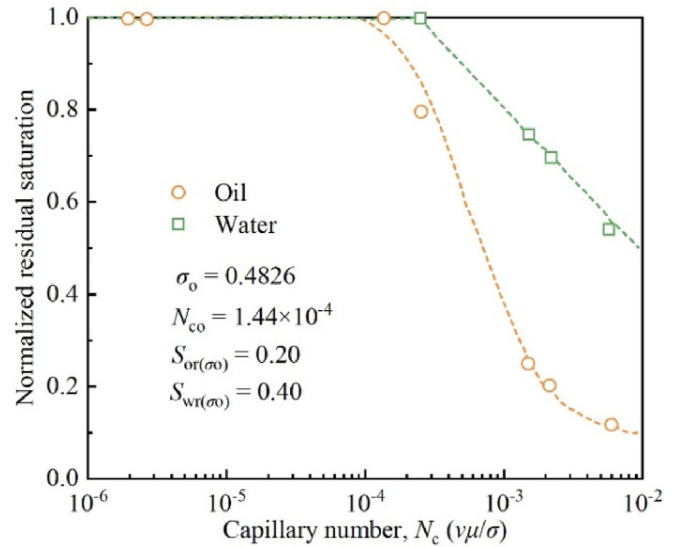


Fig. 17. Normalized residual saturations as functions of the capillary number (Amaefule and Handy, 1982).

Flooding steps 1a and 2a were drainage processes, and flooding steps 1b and 2b were imbibition processes. In each flooding step, a broader range of  $N_c$  was obtained by an increase in flow rate.

Analyzing the wetting-phase results, Chukwudeme et al. (2014) found that the capillary desaturation curve for the water phase is not a true capillary desaturation curve. First, the residual saturation in Fig. 16 is the average remaining water saturation, which is higher than the residual saturation obtained from  $P_c$  measurements. Additionally, the residual saturation is only partly a function of  $N_c$ . The capillary end effect, the number of pore volumes injected and the core length also affect the residual saturation.

Moreover, Bardon and Longeron (1980) examined the influence of the IFT on the residual liquid saturation in the  $C_1$ - $nC_7$  system at 344.1 K. The residual liquid saturation decreased with decreasing IFT. By performing several experiments with the  $C_1$ - $nC_{10}$  system at 310.7 K at different flow rates, they suggested that residual liquid saturation was independent of the fluid velocity. Moreover, Bardon

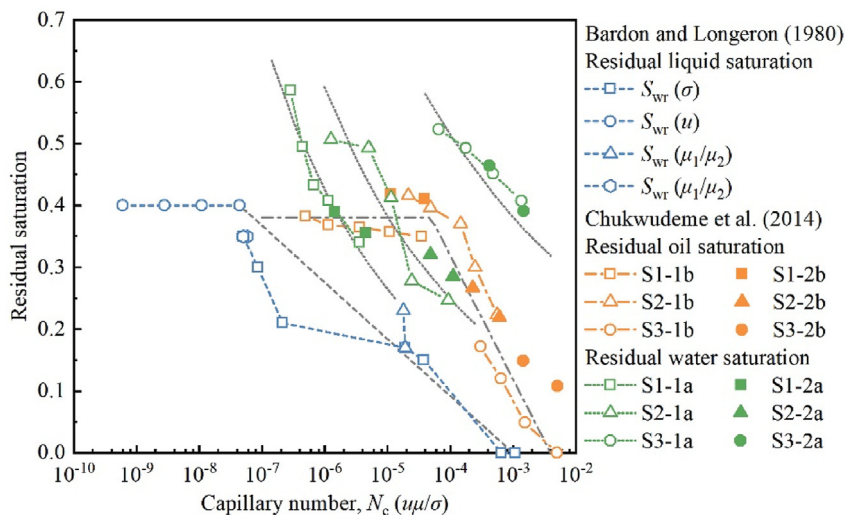


Fig. 16. The effect of capillary number,  $N_c$ , on residual saturation (Bardon and Longeron, 1980; Chukwudeme et al., 2014).

and Longeron (1980) investigated the effect of the viscosity ratio on the residual liquid saturation. The IFT and capillary number of the C<sub>1</sub>-nC<sub>10</sub> mixture at 310.7 K and 8.76 MPa were approximately the same as those at 344.1 K and 2.76 MPa. Identical residual liquid saturation results were obtained with two systems with different viscosity ratios. However, for the C<sub>1</sub>-nC<sub>5</sub> fluid system at 310.7 K and 1.62 MPa and the C<sub>1</sub>-nC<sub>7</sub> mixture at 344.1 K and 2.31 MPa, a difference of 6% in the residual liquid saturation was observed. The capillary number and IFT were comparable for both systems. The difference was attributed to the “critical zone” around an IFT value of 0.04 mN/m.

As shown in Fig. 17, Amaefule and Handy (1982) analyzed the relation between normalized residual saturations and capillary number. They normalized the residual saturations by the high-tension residual saturations. Empirical correlations, which relate the IFT and residual saturation through the capillary number, are developed as follows:

$$S_{or(\sigma)} / S_{or(\sigma_0)} \equiv f\left(\frac{\sigma}{\sigma_0}\right) = f\left(\frac{N_{co}}{N_c}\right) \quad (12)$$

$$S_{or(\sigma)} = \begin{cases} S_{or(\sigma_0)} & N_c < N_{co} \\ S_{or(\sigma_0)} \left(\frac{N_{co}}{N_c}\right)^{m_o} & N_c \geq N_{co} \end{cases} \quad (13)$$

$$S_{or(\sigma)} = \begin{cases} S_{or(\sigma_0)} & N_c < N_{co} \\ S_{or(\sigma_0)} \left(\frac{N_{co}}{N_c}\right)^{m_o} & N_c \geq N_{co} \end{cases} \quad (14)$$

where  $N_{co}$  and  $N_{cwo}$  are the critical capillary numbers for oil and water, respectively;  $S_{or(\sigma_0)}$  and  $S_{wr(\sigma_0)}$  are the residual oil and water saturations at  $N_{co}$  and  $N_{cwo}$ , respectively;  $S_{or(\sigma)}$  and  $S_{wr(\sigma)}$  are the residual oil and water saturations corresponding to any capillary number,  $N_c$ ;  $m_o$  and  $m_w$  are the capillary number exponents for oil and water, respectively;  $\sigma$  and  $\sigma_0$  are the IFT values corresponding to  $N_c$  and  $N_{co}$ , respectively.  $N_{co}$  and  $N_{cwo}$  are assumed to be equal in the correlations. The values of  $\sigma_0$ ,  $N_{co}$ ,  $S_{or(\sigma_0)}$  and  $S_{wr(\sigma_0)}$  are shown in Fig. 17.

To obtain the capillary number exponents, the log-log plots of residual saturations as a function of the capillary number are shown in Fig. 18. With no more than 10% deviation, all the points

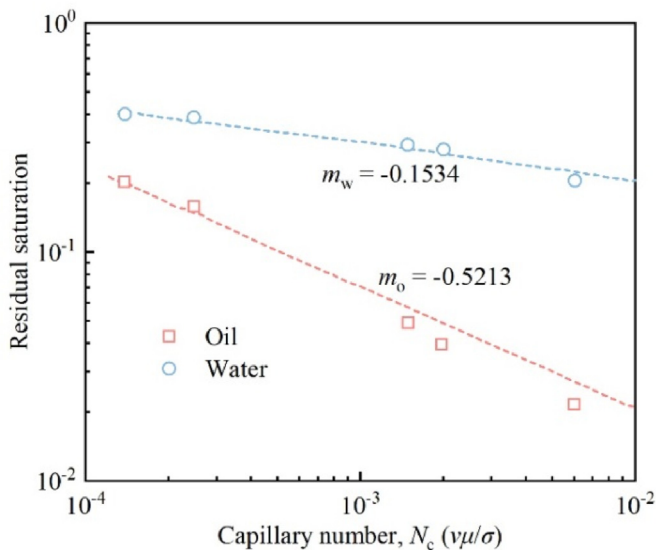


Fig. 18. Residual saturations as functions of the capillary number (Amaefule and Handy, 1982).

obtained in the experiments are in good agreement with the linear relationship. From the slopes of these plots, the capillary number exponents of 0.5213 and 0.1534 are obtained.

Another two correlations were developed by Fulcher et al. (1985) by performing regression analysis on the experimental residual saturation data. Fulcher et al. (1985) hypothesized that residual oil saturation was a function of capillary number. However, their results found that the residual water saturation varied with only IFT. The empirical correlations were expressed as follows:

$$S_{or} = 0.5846 + 0.296 \ln N_c + 0.0462(\ln N_c)^2 + 1.8855 \times 10^{-3}(\ln N_c)^3 \quad (15)$$

$$S_{wr} = 0.40214 + 3.976 \times 10^{-3} \ln \sigma - 7.065 \times 10^{-3}(\ln \sigma)^2 \quad (16)$$

Due to the difficulty in conducting low-IFT experiments and measurements under laboratory conditions, the ranges of  $N_c$  covered in the abovementioned studies were limited to less than

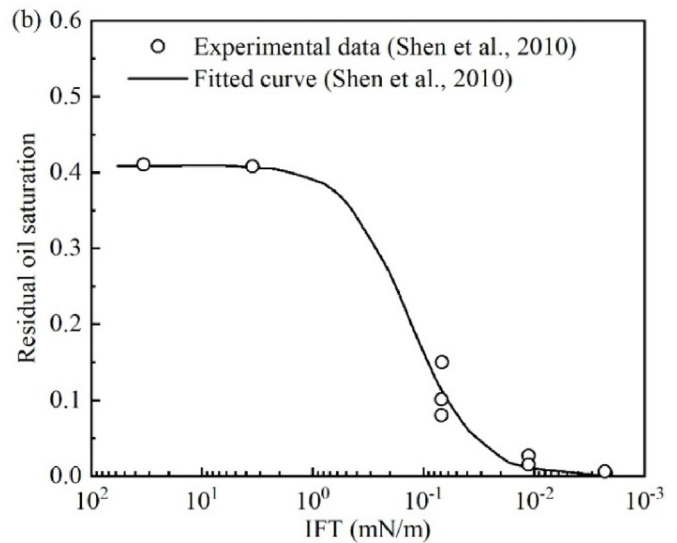
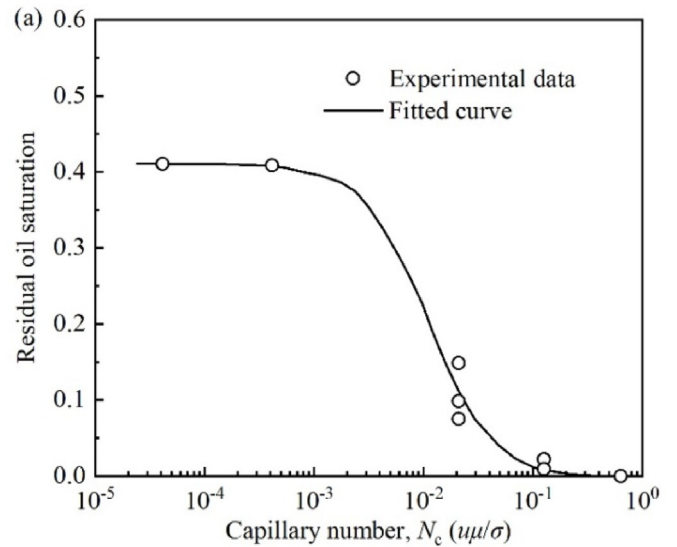


Fig. 19. (a) Experimentally determined residual saturations as functions of the capillary number. (b) Residual saturations as functions of the IFT in water/oil systems (Shen et al., 2010).

$10^{-2}$ . Shen et al. (2010) presented an improved steady-state method to fill the large gap between research and application regarding the water/oil relative permeability under low and more realistic ranges of the IFT. Correspondingly, the  $N_c$  was approximately increased to a value of 1. They found two crucial values ( $\sigma_{c1}$  and  $\sigma_{c2}$ ) in the correlation between the residual oil saturation and IFT within core-fluid flow systems (Fig. 19). At  $IFT > \sigma_{c1}$  ( $= 3$  mN/m), the residual oil saturation remained at a plateau value of 0.4. When  $IFT < \sigma_{c2}$  ( $= 0.01$  mN/m), the residual oil saturation also remained at a low constant value. However, for the intermediate values of IFT ( $\sigma_{c2} < IFT < \sigma_{c1}$ ), the residual saturation decreased rapidly with decreasing IFT.

Furthermore, Shen et al. (2010) developed an empirical correlation between residual oil saturation ( $S_{or}$ ) and IFT by fitting and statistical analysis of the experimental data:

$$S_{or} = \frac{\sigma^{1.5}}{2.432\sigma^{1.5} + 0.1154} \quad (r_{cc}^2 = 0.9995, \quad F_{stat} = 5517) \quad (17)$$

where  $r_{cc}$  and  $F$  are the correlation coefficient and statistic from an  $F$ -test, respectively.

(3) Endpoint relative permeability

The endpoint relative permeability to the wetting phase (water),  $k_{rw}(S_{or})$ , is defined as the relative permeability to the wetting phase at the residual nonwetting-phase (oil) saturation. The results of previous studies reveal that the endpoint relative permeabilities to water for low IFTs (high  $N_c$ ) are higher than those for high IFTs (low  $N_c$ ). As shown in Fig. 20, Torabzadey and Handy (1984) reported that the endpoint relative permeability to water was higher at lower IFTs (higher  $N_c$ ). Harbert (1983) also reported an increase in the endpoint relative permeability to water by increasing the capillary number,  $N_c$ , within a range of  $10^{-5}$  to  $10^{-3}$ . Notably, the endpoint relative permeability to water for the Muddy J 1 formation remained constant because it is equal to 1.

Batychy and McCaffery (1978) investigated the IFT effect on the relative permeability of unconsolidated sand. The results revealed an increase in the relative permeability with decreasing the IFT. Amaefule and Handy (1982) observed the same trend in Berea

sandstone cores. However, the endpoint relative permeability to water determined by unsteady-state tests was higher than that determined by steady-state tests. Fulcher et al. (1985) also reported that  $k_{rw}(S_{or})$  tended to increase at lower IFTs, as shown in Fig. 21.

The endpoint relative permeability to the nonwetting phase (oil),  $k_{ro}(S_{wr})$ , is defined as the relative permeability to the nonwetting phase at the residual wetting-phase (water) saturation. The results of previous studies revealed that the endpoint relative permeabilities to the nonwetting phase for low IFTs (high  $N_c$ ) were higher than those for high IFTs (low  $N_c$ ). However, the endpoint relative permeability to the nonwetting phase would remain constant if its value approximates 1.

As shown in Fig. 22, Torabzadey and Handy (1984) reported that the endpoint relative permeability to oil was higher at lower IFT (higher  $N_c$ ). However, the endpoint relative permeability to oil remained constant because it was equal to 1.

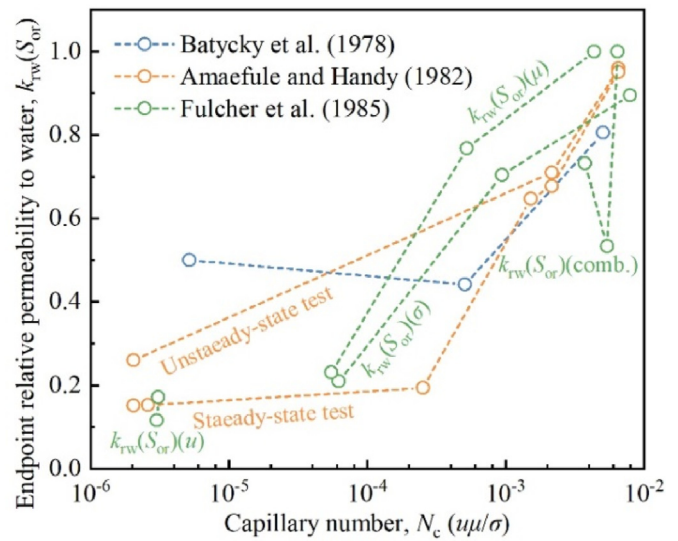


Fig. 21. The variation in the endpoint relative permeability to water with  $N_c$  in water/oil systems (Batychy and McCaffery, 1978; Amaefule and Handy, 1982; Fulcher et al., 1985).

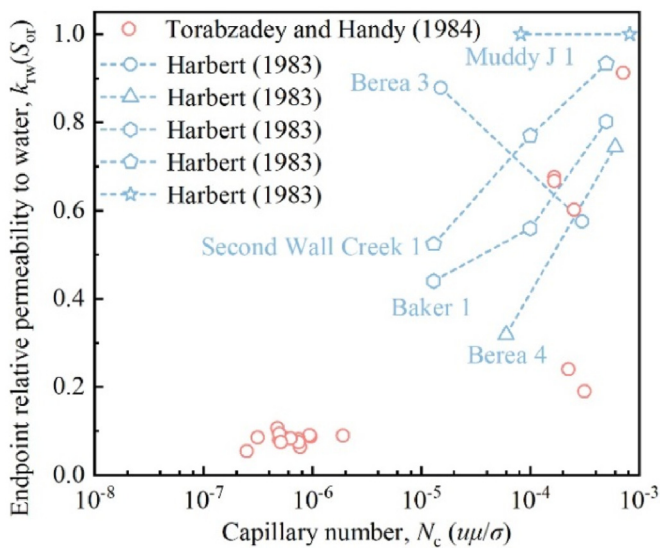


Fig. 20. The increasing trend of the endpoint relative permeability to water in water/oil systems (Harbert, 1983; Torabzadey and Handy, 1984).

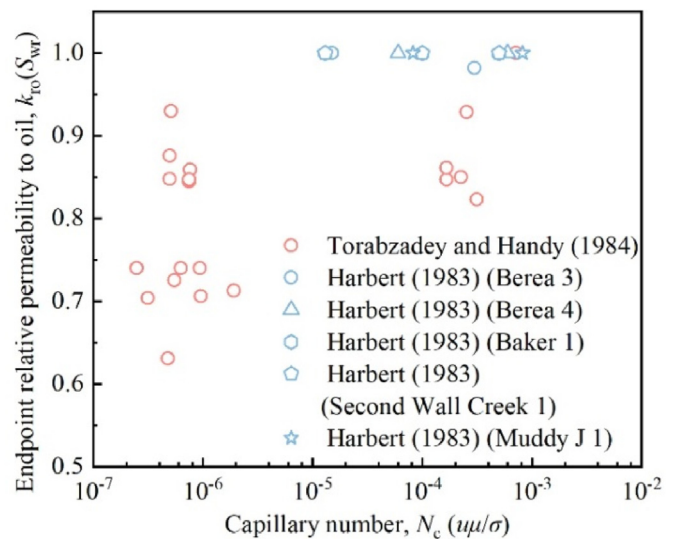


Fig. 22. The variation in oil endpoint relative permeability in water/oil systems (Harbert, 1983; Torabzadey and Handy, 1984).

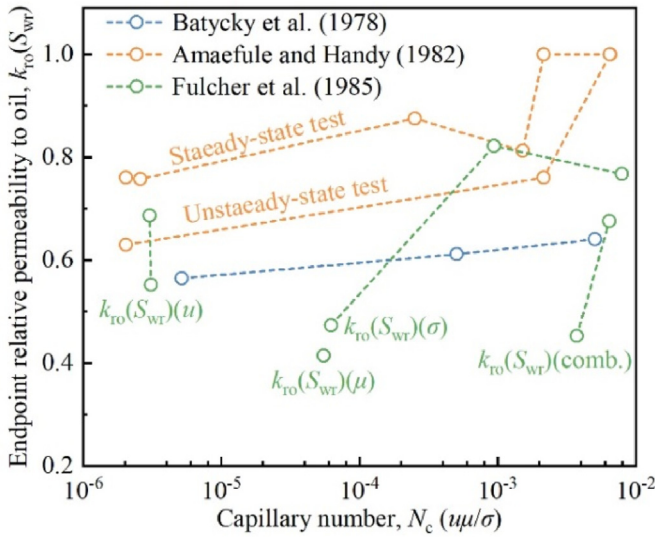


Fig. 23. The increasing trend of oil endpoint relative permeability with  $N_c$  in water/oil systems (Batycky and McCaffery, 1978; Amaefule and Handy, 1982; Fulcher et al., 1985).

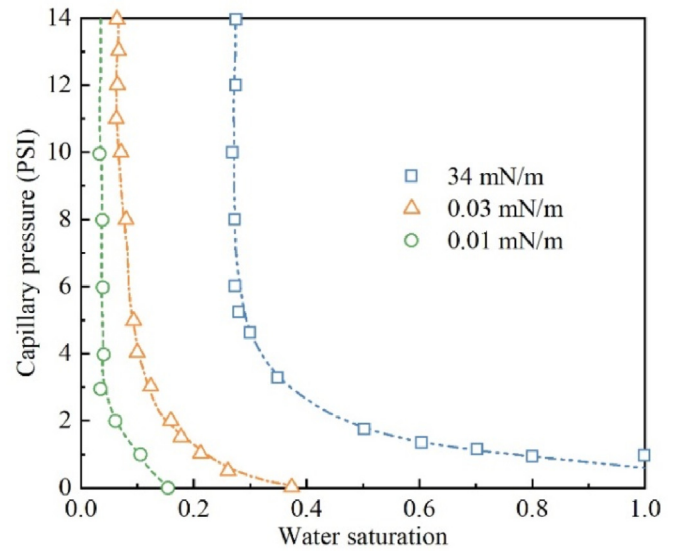


Fig. 25. Effect of IFT on capillary curves (Amaefule and Handy, 1982).

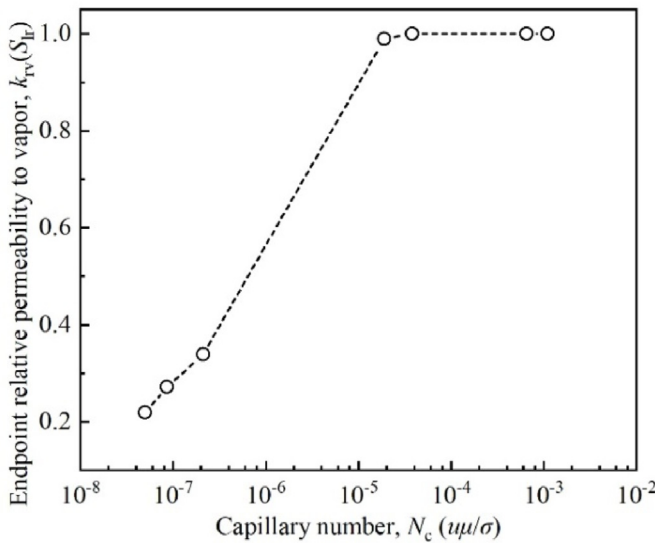


Fig. 24. The variation in nonwetting-phase (vapor) endpoint relative permeability with  $N_c$  in vapor/liquid systems (Bardon and Longeron, 1980).

The results presented in Fig. 23 show that the endpoint relative permeability to oil increased with decreasing IFT (corresponding to increasing  $N_c$ ). Bardon and Longeron (1980) also reported that the endpoint relative permeability to the nonwetting phase (vapor) tended to increase at a lower IFT until it was equal to 1, as shown in Fig. 24.

(4) Capillary pressure characteristics

Amaefule and Handy (1982) investigated the effect of IFT on the drainage capillary curves by centrifuge test. They reported that the capillary pressure curves shifted toward lower water saturations and that the capillary pressure decreased with decreasing IFT (Fig. 25). In addition, they also demonstrated that the residual water saturations obtained by the capillary pressure procedures were lower than those obtained in the conventional flow

experiments. These differences were attributed to the differences in the flow behavior. In their capillary pressure experiments, the fluid distributions were significantly influenced by the bond number,  $\Delta \rho g k / \sigma$ . However, the capillary number controlled the fluid distributions in conventional flow experiments.

4.2. Wettability

4.2.1. Effect of H<sub>2</sub>S content on wettability

Wettability can be defined as the preferential tendency of one fluid over another to spread on or adhere to a solid surface (Craig, 1993; Iglauder et al., 2015). The fluids that exist in the rock pore spaces during acid gas injection are water and gas. In a water-wet gas/water/rock system, water will occupy the smaller pores and form a thin film around the edges of the larger pores. The gas will occupy the centers of the larger pores. In a gas-wet gas/water/rock system, the locations of the two fluids are reversed from those in the water-wet case.

There are various methods available to measure the gas/water/rock wettability, including coreflood methods, contact angle measurements and theoretical approaches (Iglauder, 2017). In addition to the traditional coreflood tests, two-dimensional (2D) micromodels and three-dimensional (3D) X-ray microcomputed tomography (microCT) and nuclear magnetic resonance (NMR) measurement techniques have been developed for coreflood testing (i.e. Xu et al., 2019; Umeobi et al., 2021; Yu et al., 2022). These newly developed methods can observe the fluid configurations directly in the pore space. The sessile drop method is the common method employed in contact angle measurements to provide a direct quantification of the wettability. The theoretical approach refers to atomistic molecular dynamics simulations.

The contact angle, which is experimentally measured through the denser fluid phase, has become an important measure of the wettability. This angle is entirely determined by the intermolecular force balance, and can be expressed macroscopically by the Young's equation (Young, 1805):

$$\cos \theta = \frac{\sigma_{sg} - \sigma_{sw}}{\sigma_{wg}} \tag{18}$$

where  $\theta$  is the contact angle of the rock/water/gas system,  $\sigma_{sg}$  is IFT value of the rock/gas (mN/m),  $\sigma_{sw}$  is the IFT value of the rock/water (mN/m), and  $\sigma_{wg}$  is the IFT value of the water/gas (mN/m).

$\sigma_{wg}$  is determined by the pressure, temperature and H<sub>2</sub>S content of the acid gas, as discussed in Section 4.1.1. However, the other interfacial forces,  $\sigma_{sg}$  and  $\sigma_{sw}$ , cannot be measured directly. The relationship between the contact angle and IFT is shown in Fig. 26. The contact angle varies from 0° to 180°.

It is well known that the advancing ( $\theta_a$ ) and receding ( $\theta_r$ ) contact angles must be measured during contact angle measurement due to surface roughness and/or chemical heterogeneity. Young's contact angle values are between the advancing and receding angles. The measured advancing–receding contact angles can be converted to Young's contact angle (Tadmor, 2004):

$$\theta = \arccos\left(\frac{r_a \cos \theta_a + r_r \cos \theta_r}{r_a + r_r}\right) \quad (19)$$

$$r_a = \left(\frac{\sin^3 \theta_a}{2 - 3 \cos \theta_a + \cos^3 \theta_a}\right)^{1/3} \quad (20)$$

$$r_r = \left(\frac{\sin^3 \theta_r}{2 - 3 \cos \theta_r + \cos^3 \theta_r}\right)^{1/3} \quad (21)$$

where  $r_a$  and  $r_r$  stand for the advancing and receding Young's contact angle, respectively.

The rock/water/gas wettability was classified into seven grades to more precisely evaluate the wettability of rock minerals (Iglauer et al., 2015). Complete wetting and nonwetting occur when  $\theta = 0^\circ$  and  $180^\circ$ , respectively. Partial wetting of water occurs in the water-wet, intermediate-wet, and gas-wet cases (See Table 5).

The gas/water/rock wettability is claimed to depend on the H<sub>2</sub>S content, thermophysical conditions (pressure and temperature) and the rock mineral composition. The caprocks and storage rocks in acid gas geological sequestration generally consist of a large variety of minerals, such as quartz, calcite, mica, muscovite mica, biotite mica, feldspar, montmorillonite, kaolinite, illite and smectite

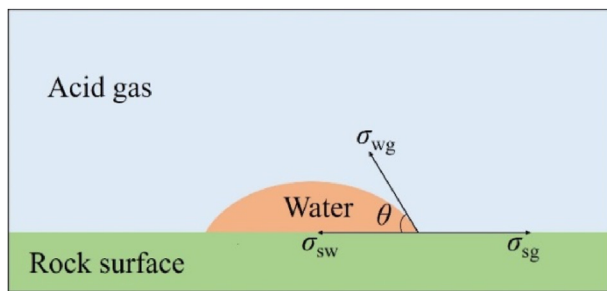


Fig. 26. Relationship between the contact angle and IFT according to Young's equation.

**Table 5**  
Wettability classification based on contact angle for rock/water/gas system (Iglauer et al., 2015).

Wettability State	Water contact angle $\theta$ (°)
Complete wetting or spreading of water	0
Strongly water-wet	0–50
Weakly water-wet	50–70
Intermediate-wet	70–110
Weakly gas-wet	110–130
Strongly gas-wet	130–180
Complete nonwetting of water	180

(Iglauer et al., 2015). However, only several researchers have investigated the water contact angles of the acid gases (CO<sub>2</sub>, H<sub>2</sub>S and their mixtures) on quartz, calcite and mica substrates (Shah et al., 2008b; Broseta et al., 2012; McCaughan et al., 2013; Chen et al., 2018). Hence, the following review provides the data available in the literature on the contact angle of quartz, calcite and mica substrates to investigate the effect of the acid gases (CO<sub>2</sub>, H<sub>2</sub>S and their mixtures) on the wettability.

A large number of experimental quartz/water/CO<sub>2</sub> contact angles have been obtained under various pressure, temperature and salinity conditions (Wesch et al., 1997; Chiquet et al., 2007b; Sutjiadi-Sia et al., 2008; Espinoza and Santamarina, 2010; Bikkina, 2011; Broseta et al., 2012; Jung and Wan, 2012; Farokhpoor et al., 2013; Saraji et al., 2013; Iglauer et al., 2014; Chen et al., 2015a). Fig. 27 displays a compilation of these water contact angles. Clearly, there is large uncertainty associated with the experimental quartz/water/CO<sub>2</sub> contact angle. Specifically, Young's contact angles from 0° to 97° have been reported. Advancing contact angles from 0° to 92° and receding contact angles from 7° to 42° were measured. The main reason for the large variation in contact angle is probably surface contamination of the substrates (Bikkina, 2012; Mahadevan, 2012; Iglauer et al., 2014).

The water contact angles of the acid gases (CO<sub>2</sub>, H<sub>2</sub>S and their mixtures) on quartz substrates are limited. Shah et al. (2008b) measured the receding and advancing contact angles for a quartz/0.08 M NaCl/H<sub>2</sub>S system. The origin and preparation of the quartz used in the contact angle measurements are the same as those used by Chiquet et al. (2007b). Quartz substrates of optical quality were purchased from OptiqueFichou, Fresnes, France. Prior to each experiment, the quartz was cleaned with a tensioactive solution under ultrasonic agitation for 30 min, rinsed with a 10% nitric-acid solution and finally washed with deionized water. Broseta et al. (2012) used the same quartz substrates to measure the receding and advancing contact angles of the quartz/brine/CO<sub>2</sub> systems. However, the method used to clean the quartz substrates prior to measuring the contact angles was not specified.

As shown in Fig. 28, the maximum contact angle of quartz/brine/CO<sub>2</sub> systems reported by Broseta et al. (2012) is 92°. In contrast, the contact angles for the quartz/brine/CO<sub>2</sub> systems obtained by Chiquet et al. (2007b) are rather low (20°–35°). Hence, we can infer that the cleaning method used by Broseta et al. (2012) is different and leads to a highly biased contact angle. To avoid the influence of surface contamination, the effect of acid gases (CO<sub>2</sub>, H<sub>2</sub>S and their mixtures) on the water wettability of quartz was investigated by comparing the results obtained by Chiquet et al. (2007b) and Shah et al. (2008b). It was concluded that the contact angle of a quartz/water/H<sub>2</sub>S system is similar to that of a quartz/water/CO<sub>2</sub> system.

Molecular dynamics simulation methods have been used to investigate the water contact angle of the acid gases (CO<sub>2</sub>, H<sub>2</sub>S and their mixtures) on quartz substrates (Liu et al., 2010; Iglauer et al., 2012; McCaughan et al., 2013; Chen et al., 2018). As discussed above, surface contamination plays a major role in the significant scattering and high uncertainties of contact angle measurements. Furthermore, the surfaces can be chemically modified during cleaning and during the experiment itself. Nonetheless, a clean mineral surface, which is difficult to achieve in the physical experiments, can be constructed in the molecular dynamics simulations (Iglauer et al., 2012; McCaughan et al., 2013; Chen et al., 2015a, b). The desired chemistry can be obtained by adding hydroxyl functional groups on quartz surfaces. Notably, quartz in a subsurface environment may not be completely clean because it has been exposed to formation fluids.

The effect of the H<sub>2</sub>S content on the water contact angles of the acid gases (CO<sub>2</sub>, H<sub>2</sub>S and their mixtures) on quartz substrates is shown in Fig. 29. Three typical molecular surface models for quartz,

i.e.  $Q^3$ ,  $Q^4$  and  $Q^3/Q^4$ , were used in the simulations. Their results indicated that an increase in  $H_2S$  increased the water contact angle. For the  $Q^3$  quartz surface, the water contact angle of the 80%  $CO_2$  + 20%  $H_2S$  mixture increased by 10.99° from that of pure  $CO_2$  at 20 MPa and 318 K. When the surface structure of quartz is  $Q^3/Q^4$ , similar results are obtained. The results of the  $Q^4$  quartz surface obtained by McCaughan et al. (2013) indicated that this increase was most apparent at low/intermediate pressures (<20 MPa) and much less apparent at higher pressures (>20 MPa).

The water-wet characteristics of muscovite mica substrates in the presence of the acid gases ( $CO_2$  and  $H_2S$ ) were evaluated by several studies (Chiquet et al., 2007b; Shah et al., 2008b; Broseta et al., 2012; Farokhpour et al., 2013). In the studies conducted by Chiquet et al. (2007b) and Shah et al. (2008b), the grade V3 muscovite mica substrate was obtained by cleaving mica sheets (S&J Trading Inc., Glen Oaks, NY, USA). The grade V2 muscovite mica substrate (Ted Pella, Redding, CA, USA), whose surface is more uniform than that of the grade V3, was used by Broseta et al. (2012). The origin of the muscovite mica substrate used by Farokhpour

et al. (2013) was not specified, but the mica surfaces were washed with Deconex solution under an ultrasonic bath and then cleaned with distilled water to minimize any roughness effect on the contact angle measurements. Hence, as shown in Fig. 30b, advancing contact angles measured by Farokhpour et al. (2013) are significantly lower than those measured by Shah et al. (2008b) and Broseta et al. (2012).

As shown in Fig. 30, the water wettability of a mica/ $CO_2$ /water system decreases slightly with increasing pressure. In contrast, a considerable change in the wettability from moderately water-wet to  $H_2S$ -wet occurs as pressure increases. When  $H_2S$  is gaseous, that is, for pressures below 3.5 MPa, the receding contact angles are in the range of 63° and 77°. The corresponding advancing contact angles are near 90°. However, a wettability reversal of mica to  $H_2S$ -wet behavior occurred when  $H_2S$  is liquid. The receding and advancing contact angles rise to approximately 118° and 150°, respectively. In conclusion, the wettability alteration is pronounced in the presence of dense  $H_2S$  compared to that in the presence of  $CO_2$ .

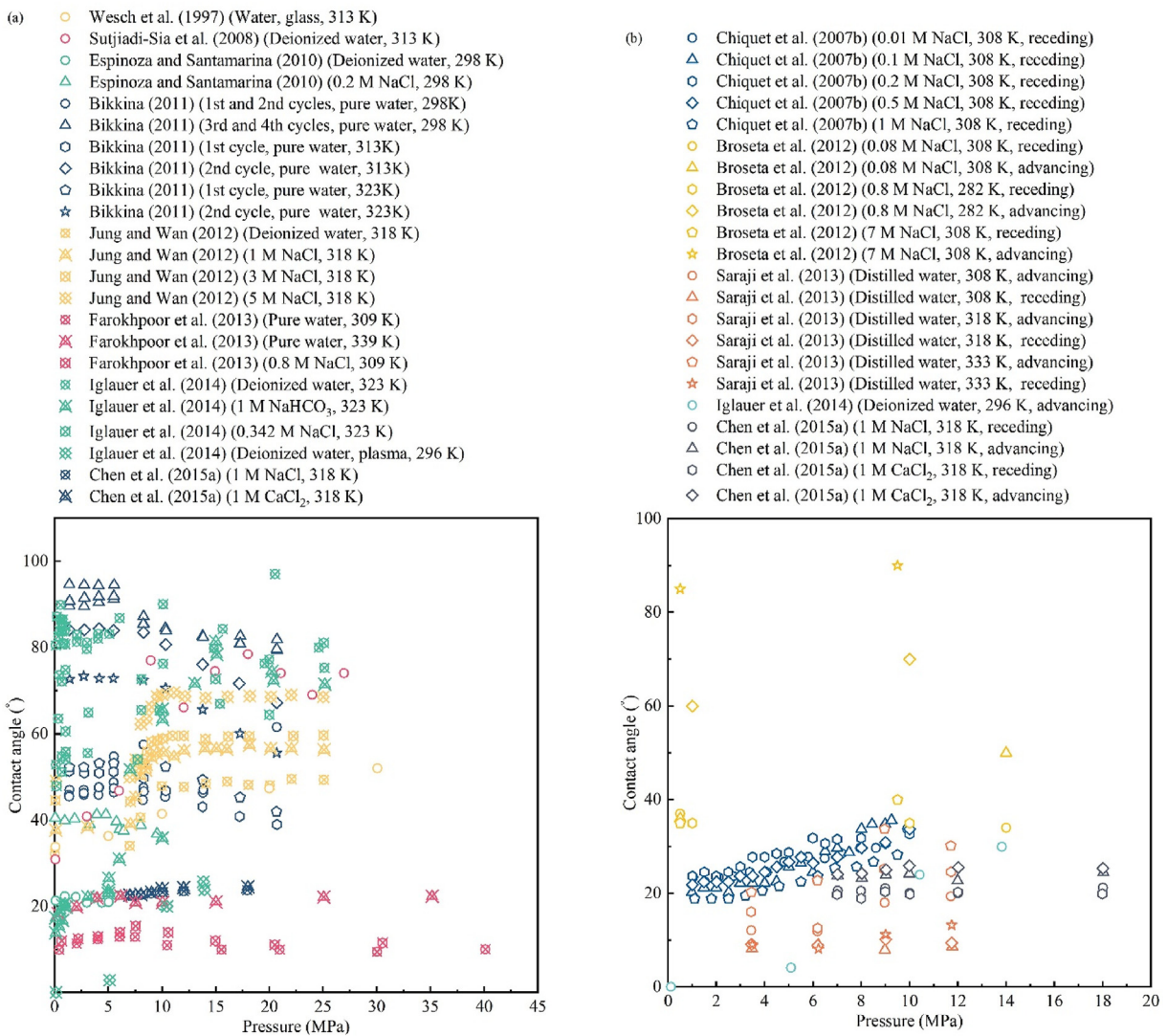


**Fig. 27.** (a) Experimental Young's contact angles of quartz/ $CO_2$ /water (or brine) systems, and (b) Receding and advancing water contact angles measured in quartz/ $CO_2$ /water (or brine) systems. (Wesch et al., 1997; Chiquet et al., 2007b; Sutjiadi-Sia et al., 2008; Espinoza and Santamarina, 2010; Bikkina, 2011; Broseta et al., 2012; Jung and Wan, 2012; Farokhpour et al., 2013; Saraji et al., 2013; Iglauer et al., 2014; Chen et al., 2015a).

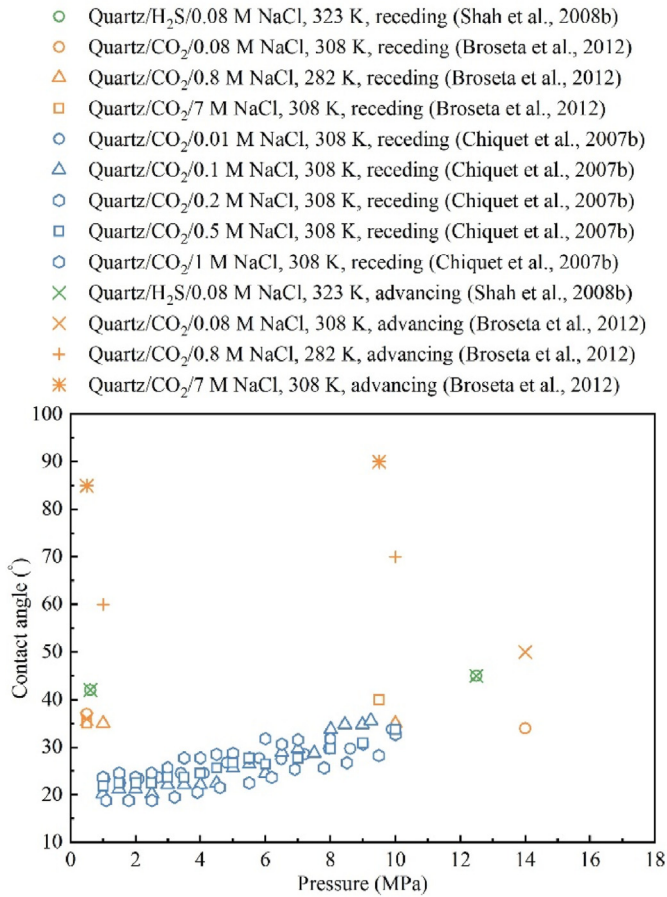


Fig. 28. Receding and advancing water contact angles measured in quartz/CO<sub>2</sub>/brine and quartz/H<sub>2</sub>S/brine systems (Chiquet et al., 2007b; Shah et al., 2008b; Broseta et al., 2012).

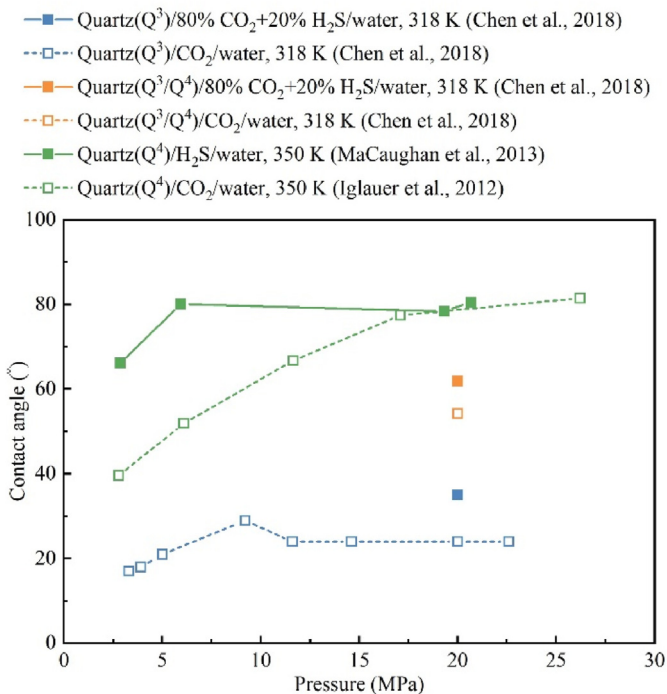


Fig. 29. The effect of the H<sub>2</sub>S content on the contact angles of the quartz/(CO<sub>2</sub>+H<sub>2</sub>S) mixture/water systems (Iglauer et al., 2012; McCaughan et al., 2013; Chen et al., 2018).

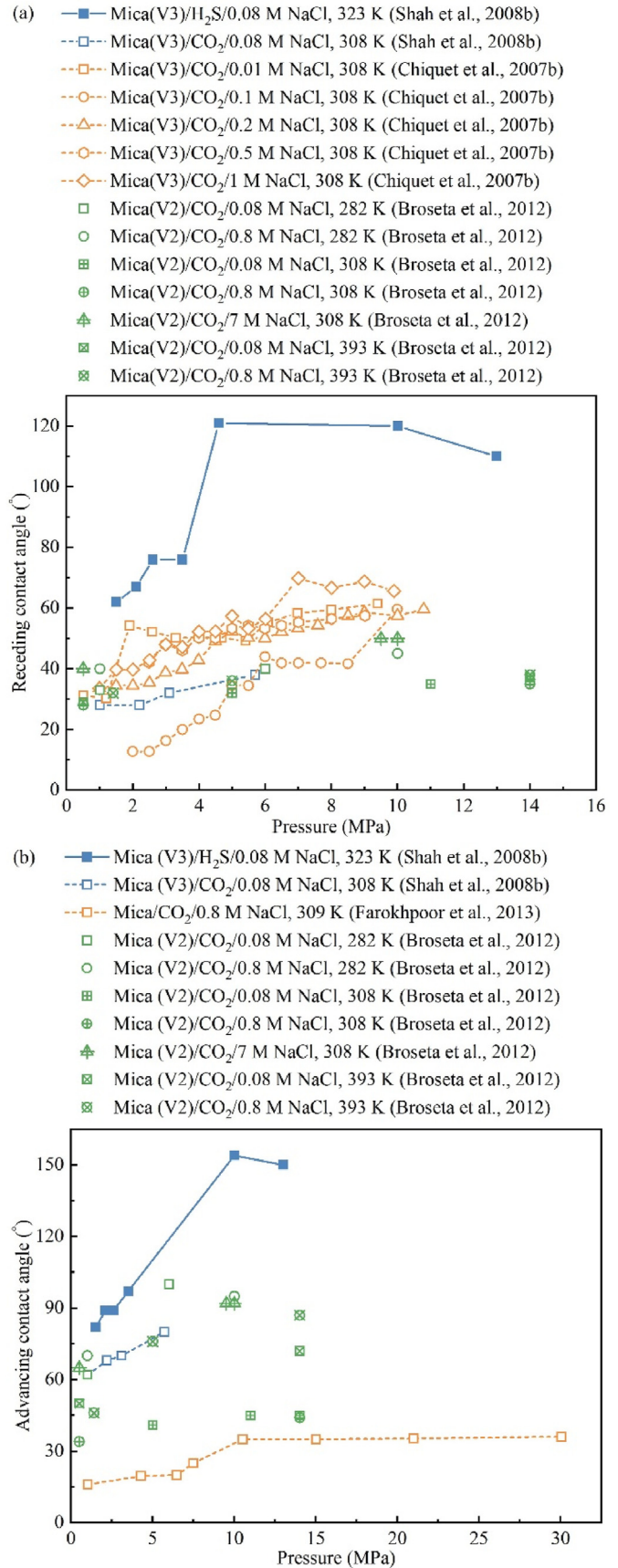
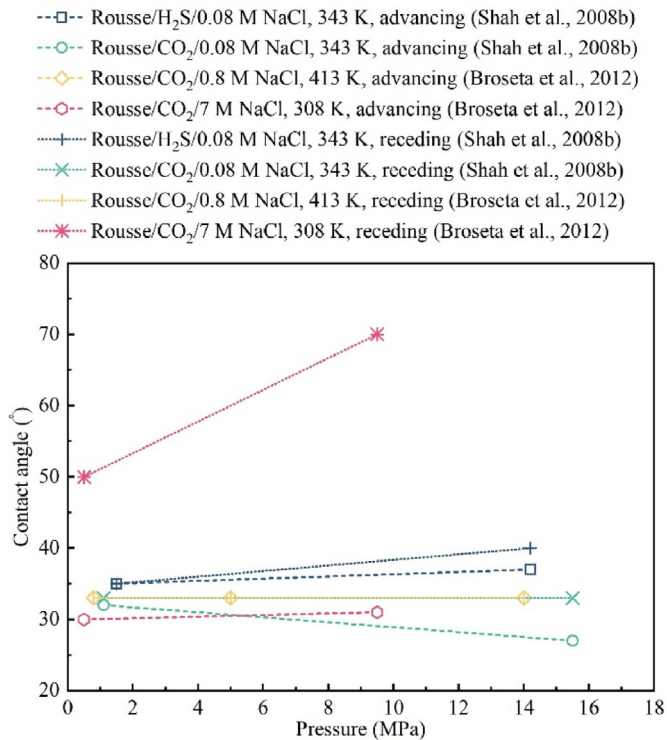


Fig. 30. (a) Receding and (b) advancing water contact angles measured in mica/CO<sub>2</sub>/brine and mica/H<sub>2</sub>S/brine systems (Chiquet et al., 2007b; Shah et al., 2008b; Broseta et al., 2012; Farokhpour et al., 2013).



**Fig. 31.** Receding and advancing water contact angles measured in Rousse/CO<sub>2</sub>/brine and Rousse/H<sub>2</sub>S/brine systems (Shah et al., 2008b; Broseta et al., 2012).

The water-wet characteristics of a ‘real’ carbonate-rich substrate drilled from the caprock of the Rousse depleted gas field in France in the presence of the acid gases (CO<sub>2</sub> and H<sub>2</sub>S) was evaluated by Shah et al. (2008b) and Broseta et al. (2012). The main constituents of this caprock sample are calcite (approximately 70%), quartz (13%), chlorite (10%) and illite/mica (4.5%). As shown in Fig. 31, the wetting behavior of this caprock with H<sub>2</sub>S in a low-salinity brine does not exhibit significant changes compared to that in the presence of CO<sub>2</sub> and remained water-wet.

#### 4.2.2. Effect of wettability on relative permeability and capillary pressure characteristics

##### (1) Relative permeability nonlinearity

Several investigators (Donaldson and Thomas, 1971; Owens and Archer, 1971; Morrow et al., 1973) have endeavored to detect whether the relative permeability characteristics change with wettability. Owens and Archer (1971) experimentally evaluated the effect of rock wettability on oil/water relative permeability relationships. The oil/water relative permeability data of the Torpedo core were obtained by the steady-state testing procedure. The water contact angle on quartz crystals was monitored by photographic techniques. Notably, the oil/water contact angles in oil/water/Torpedo core systems may not be the same as those measured in oil/water/quartz systems, even though pure quartz was believed to be the main mineral component in the Torpedo core. Nevertheless, the contact angles measured in oil/water/quartz systems were supposed to indicate the changes in the degree of oil wetting or water wetting in oil/water/Torpedo core systems during the flow tests. In Fig. 32, the results show that at any tested water saturation, as the system becomes more oil-wet, the water relative permeability increases, and the oil relative permeability decreases.

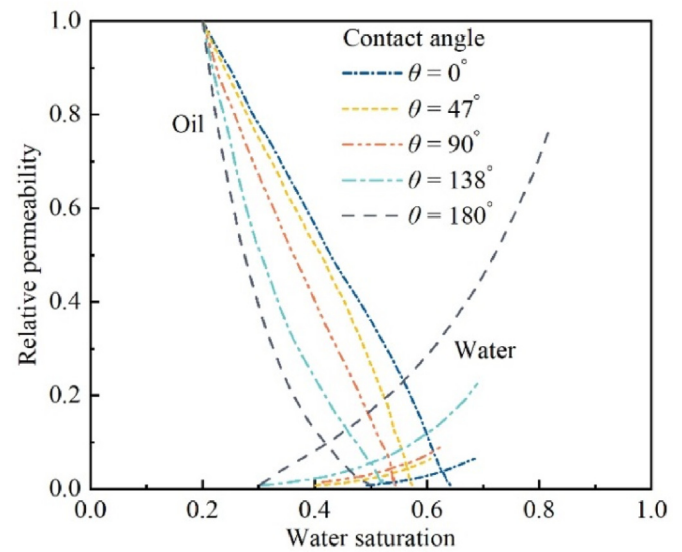


**Fig. 32.** Effect of wettability on relative permeability curves of the Torpedo core (Owens and Archer, 1971).

Donaldson and Thomas (1971) and Morrow et al. (1973) also compared the relative permeabilities under different wettability conditions. They also found that at any tested water saturation, as the system became more oil-wet, the water relative permeability increased, and the oil relative permeability decreased. The results of Donaldson and Thomas (1971) suggested that the oil permeability at the initial water saturation decreased as the system became more oil-wet. In the study of Morrow et al. (1973), the contact angles of 15°, 100° and 155° were obtained at octanoic acid concentrations of 0 mol/L, 5 × 10<sup>-3</sup> mol/L and 0.1 mol/L in oil, respectively. A crossover point between the oil relative permeability curve for the intermediate-wet system (100°) and that for the water-wet system (15°) occurred at a water saturation of approximately 62%. This apparently anomalous behavior was attributed to the fact that even a small change in the octanoic acid concentration at approximately 5 × 10<sup>-3</sup> M had a significant effect on the wettability of the intermediate-wet system.

Previous investigators (Donaldson and Thomas, 1971; Owens and Archer, 1971; Morrow et al., 1973) used the representative core samples for which wettability conditions were controlled by surfactants to study the effects of wettability on the relative permeability. The apparent drawback was that those tests essentially measured the combined effects of pore geometry and wettability during the displacement processes. To characterize and isolate the effects of wettability on relative permeability, several researchers (Mungan, 1966; McCaffery and Bennion, 1974) have used consolidated polytetrafluoroethylene (PTFE) as porous media and various fluid pairs, which display essentially different wetting behaviors with solids. The results were generally in good agreement with the findings of the abovementioned investigators (Donaldson and Thomas, 1971; Owens and Archer, 1971; Morrow et al., 1973).

However, a notable difference was found in the study of McCaffery and Bennion (1974). As shown in Fig. 33, there was no effect of contact angle on relative permeability when the system was strongly wetted, with large changes occurring only when the system was near neutral wettability. These conclusions can be derived from the curves marked “up to 49°” and “138° and greater” in the relative permeability curves.

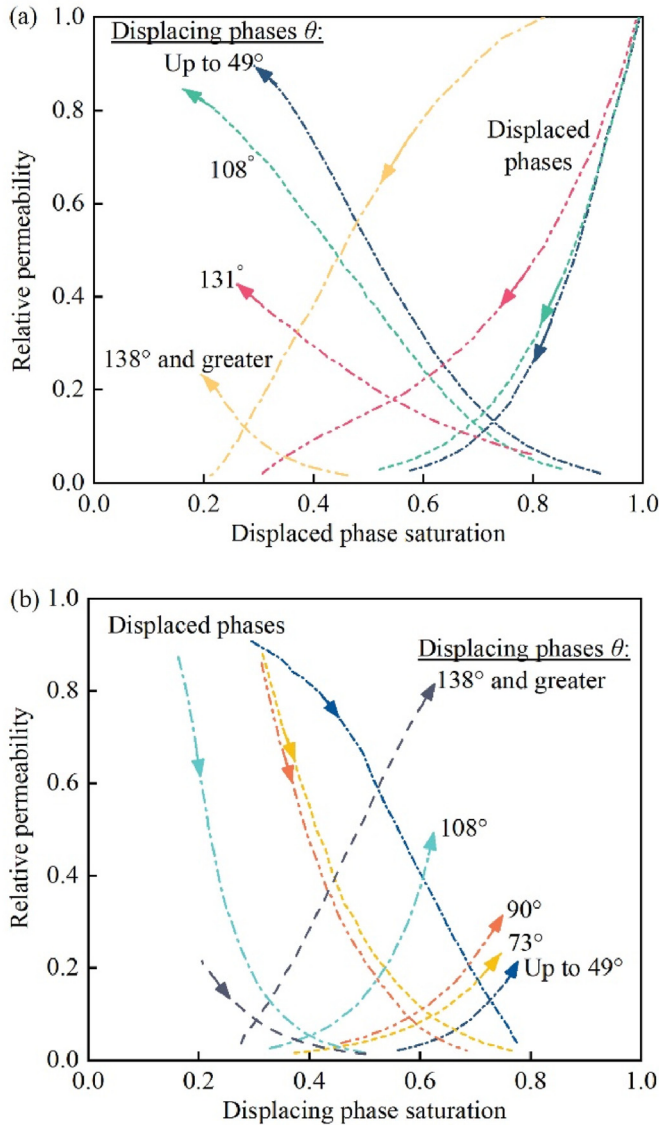


Fig. 33. Effects of wettability on the relative permeability of PTFE cores (a) During the drainage process and (b) During the imbibition process (McCaffery and Bennion, 1974).

Fig. 34, taken from Craig (1993), shows the typical water/oil relative permeability curves of strongly water-wet and strongly oil-wet systems. The differences in the relative permeability characteristics of strongly wetted cores can be illustrated by Craig's rules of thumb, given in Table 6.

The preceding review of reported results confirms that at a given saturation, the relative permeability of a fluid is higher when it is the nonwetting phase in a system than when it is the wetting phase in another system. For example, at any given water saturation, the water relative permeability is higher in an oil-wet system than in a water-wet system. This is because, at the pore scale, the wetting fluid fills the narrowest regions of the pore space and is poorly connected, while the nonwetting fluid is stranded in the larger pores and travels more easily (Fig. 35). In addition, at a low nonwetting-phase saturation, the nonwetting phase is present as discrete droplets in the centers of the pore spaces (Fig. 35). These discrete droplets block pore throats, leading to a lower wetting-phase relative permeability.

(2) Residual saturation

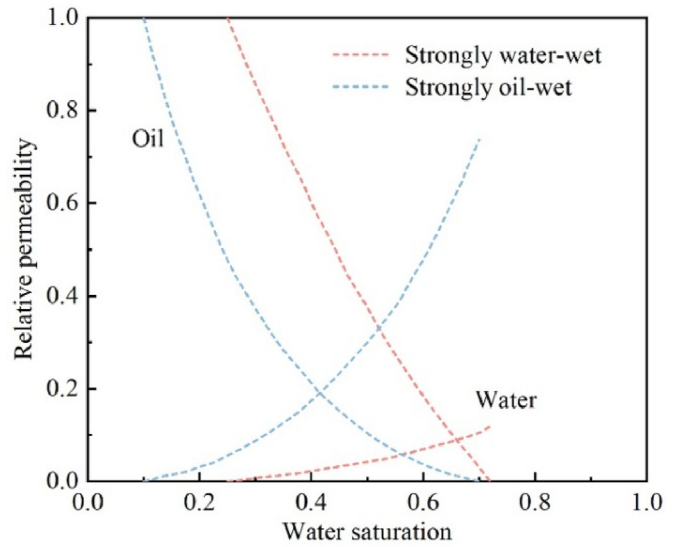


Fig. 34. Typical water/oil relative permeability curves for strongly water-wet and oil-wet systems (Craig, 1993).

Table 6  
Craig's rules of thumb (Craig, 1993).

Parameters	Strongly water-wet	Strongly oil-wet
Residual water saturation	Generally greater than 20%–50%	Generally less than 15%, frequently less than 10%
Saturation at which the oil and water relative permeabilities are equal	Greater than 50% water saturation	Less than 50% water saturation
Relative permeability to water at the maximum water saturation (i.e. floodout), based on the effective oil permeability at residual saturation of the reservoir	Generally less than 30%	Greater than 50% and approaching 100%

Both residual wetting and nonwetting phases are affected by wettability. Some studies reported that the residual water saturation increased when the uniformly wetted system became more water-wet. According to Craig's rule of thumb (Table 6), the residual water saturation should be generally less than 15% in the oil-wet rocks and usually greater than 20%–25% in the water-wet rocks. Furthermore, Donaldson and Thomas (1971) also examined the effect of the wettability on the residual water saturation. In that work, the residual water saturation was obtained by injection of oil until the flow of water ceased. Their results, in Fig. 36, show an increase in the residual water saturation with increasing wettability number. The wettability number is calculated by the means of the areas under a capillary pressure curve which is obtained by the centrifuge method (Donaldson et al., 1969):

$$W = \log_{10}(A_1/A_2) \tag{22}$$

where  $A_1$  and  $A_2$  are the areas under the oil- and brine-drive curves, respectively.

In recent years, several studies have been carried out to investigate the effect of wettability on the residual trapping of CO<sub>2</sub>. Pentland et al. (2011) used the porous plate coreflood method to measure the capillary trapping of supercritical CO<sub>2</sub>. It was found that the CO<sub>2</sub> saturation dropped to 35% after injection of brine (5 wt

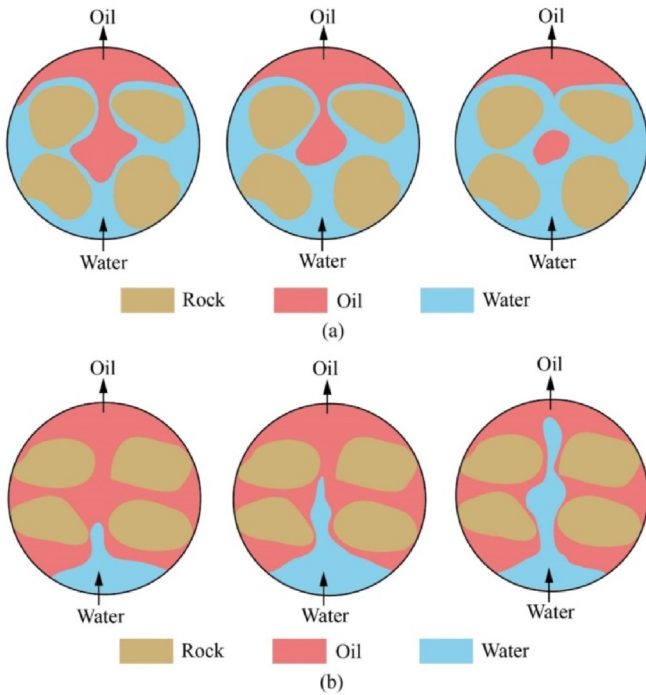


Fig. 35. Water displacing oil from a pore during waterflooding: (a) Strongly water-wet rock and (b) Strongly oil-wet rock.

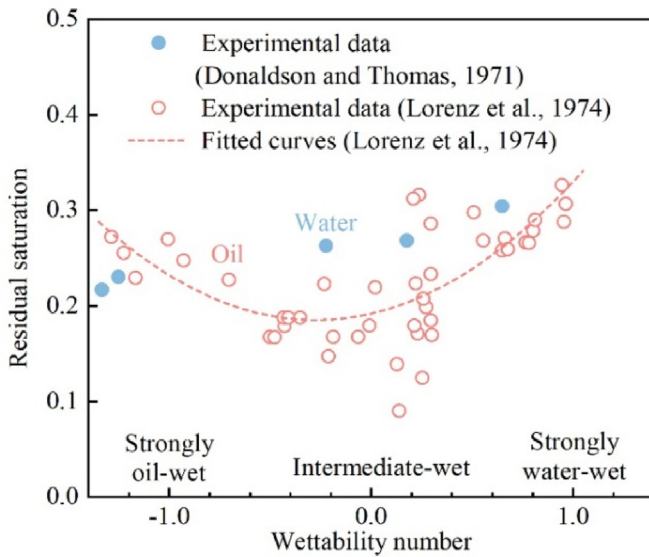


Fig. 36. The variation in residual saturation with wettability number (Donaldson and Thomas, 1971; Lorenz et al., 1974).

% NaCl and 1 wt% KCl), which was less than the maximum trapped saturation of 48% measured in an equivalent *n*-decane (oil)-brine experiment. This was due to an increase in the contact angle of the CO<sub>2</sub>/brine system. Chaudhary et al. (2013) conducted two-phase flow experiments using columns subjected to reservoir conditions to address how the grain wettability would control the capillary trapping of supercritical CO<sub>2</sub>. High-resolution X-ray computed tomography was used to image the columns, which were packed with water-wet glass beads and CO<sub>2</sub>-wet Teflon beads. Under the condition of 12.4 MPa and 333 K, the contact angle was 65° for the CO<sub>2</sub>/

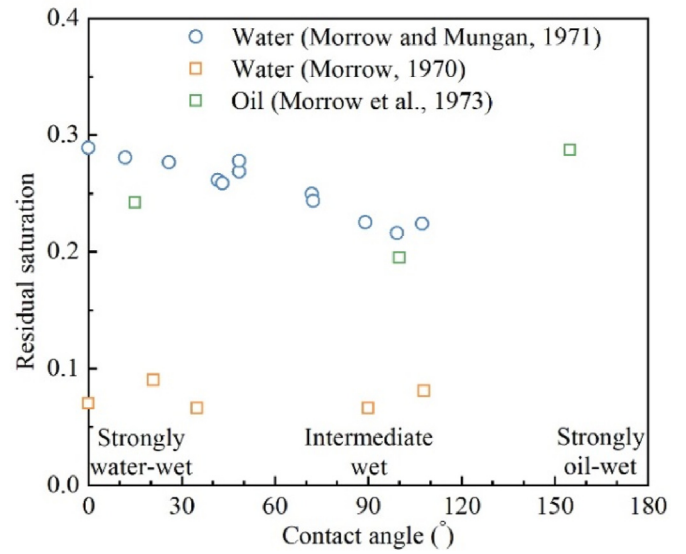


Fig. 37. The variation in residual saturation with contact angle (Morrow, 1970; Morrow and Mungan, 1971; Morrow et al., 1973).

1 wt% NaBr brine/glass system and 138° for the CO<sub>2</sub>/1 wt% NaBr brine/Teflon system. The results showed that the residual CO<sub>2</sub> saturation was 15% and 2% in the glass bead and Teflon bead media, respectively. Rahman et al. (2016) also demonstrated that the residual CO<sub>2</sub> saturation of oil-wet rock was significantly lower than that of water-wet rock because the oil-wet rock was intermediate-wet or CO<sub>2</sub>-wet under reservoir conditions.

The involvement of the wettability in determination of the residual CO<sub>2</sub> saturation can be explained at the pore scale, and the amount of trapping is controlled by the competition between snap-off and piston-like advance (Iglauer et al., 2010, 2011; Alyafei and Blunt, 2016). In a strongly water-wet system, water fills the narrowest regions of the pore space in order of size by snap-off, stranding the nonwetting phase (CO<sub>2</sub>) in the larger pores. This leads to the trapping of more CO<sub>2</sub> in the larger pores. As the contact angle increases, the piston-like advance becomes more common than the snap-off. In that case, a lower residual saturation is expected because the piston-like advance of water will simply push out the nonwetting phase, without trapping it.

In contrast to the abovementioned studies, Morrow and Mungan (1971) reported that the measured residual water saturation first decreased under the strongly water-wet conditions and then increased under the strongly oil-wet conditions. As shown in Fig. 37, the minimum residual saturation occurs at near-neutral wettability conditions, when  $\theta = 90^\circ$ . A similar trend of residual oil saturation was obtained by Morrow et al. (1973), as illustrated in Fig. 37. A minimum residual saturation value of 0.195 was obtained under the intermediate-wet conditions, when  $\theta = 100^\circ$ .

Lorenz et al. (1974) examined the effect of the wettability on the residual oil saturation. Note that the residual saturation was obtained by immersing cores in oil and centrifuging at high speeds. According to the obtained residual saturation (see Fig. 36), Lorenz et al. (1974) developed a least-squares equation with a 99% confidence level:

$$S_{or} = 0.192 + 0.049W + 0.089W^2 \quad (23)$$

where *W* is the wettability number. The results suggest that the minimum residual oil saturation occurs at a slightly oil-wet condition when  $W = -0.3$ .

The abovementioned findings do not apply to very homogeneous porous media such as beads and sandpicks. Under these circumstances, the residual saturation is typically very low and rarely affected by the wettability. A study by Morrow (1970) showed that in very homogeneous packings of equal-size Teflon spheres, the residual water saturation was always in the range of  $7.5\% \pm 1.5\%$ , while the contact angle was varied from  $0^\circ$  to  $108^\circ$  (Fig. 37). Very little effect of the wettability on the residual saturation was also found for packed beads (Von Engelhardt, 1955; Harris et al., 1963).

### (3) Endpoint relative permeability

The effect of wettability on the endpoint relative permeability is caused by the differences in the fluid distributions. For a strongly water-wet system at the residual water saturation, the water (wetting phase) occupies the narrowest regions of the pore space, where it has very little effect on the flow of oil (nonwetting phase). Thus, the endpoint relative permeability to oil is relatively high, often approaching 100%. In contrast, for a strongly oil-wet system at residual water saturation, water (nonwetting phase) appears as discrete droplets in the centers of the pore spaces. These discrete droplets block pore throats, leading to a lower endpoint relative permeability to oil (wetting phase). Likewise, for a strongly water-wet system at the residual oil saturation, the endpoint relative permeability to water (wetting phase) is low because the residual oil (nonwetting phase) blocks the water flow. For a strongly oil-wet system at the residual oil saturation, the endpoint relative permeability to water is high because the oil (wetting phase) occupies the narrowest regions of the pore space, where it has very little effect on the water (nonwetting phase) flow. Consequently, the endpoint relative permeability to water is higher when the system is more water-wet. The endpoint relative permeability to water is lower when the system is more water-wet.

Fig. 38 shows the examples of the effect of wettability on the endpoint relative permeability. When a system is more water-wet, the endpoint relative permeability to water is lower, while the endpoint relative permeability to oil is higher. Morrow et al. (1973) also reported that the endpoint relative permeability to water increased with increasing contact angle (Fig. 39). In another study

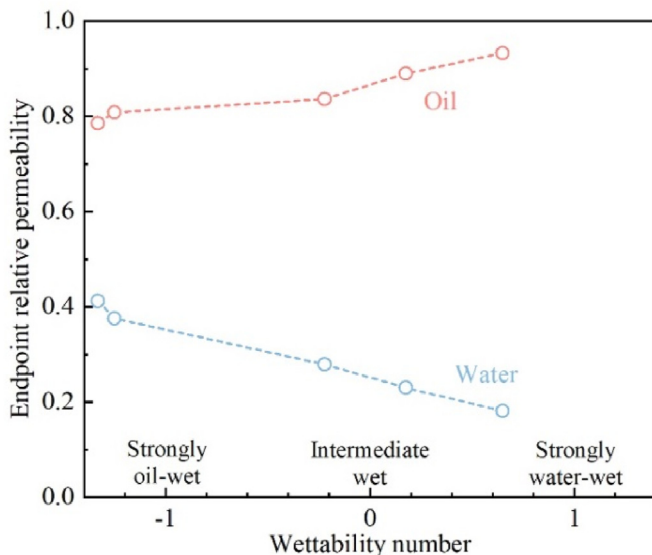


Fig. 38. The variation in endpoint relative permeability with wettability number (Donaldson and Thomas, 1971).

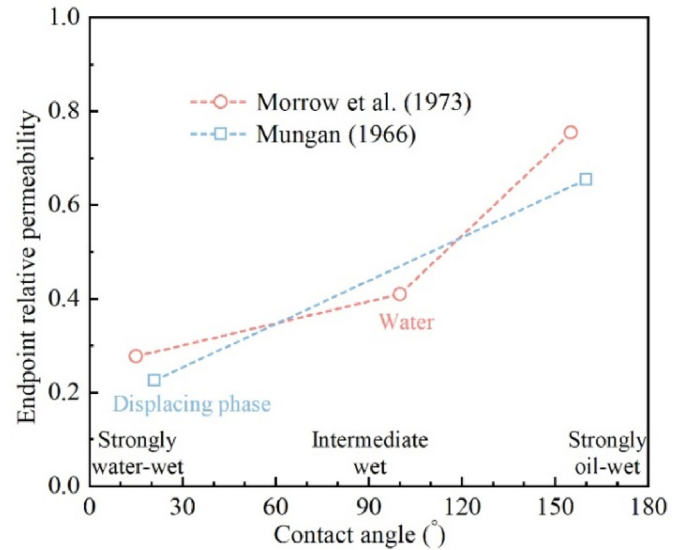


Fig. 39. The variation in endpoint relative permeability with contact angle (Mungan, 1966; Morrow et al., 1973).

performed by Mungan (1966), the results clearly showed that the endpoint relative permeability to the displacing phase increased as the displacing phase transitioned from nonwetting to wetting phase.

### (4) Capillary pressure characteristics

Likewise, the wettability plays an important role in controlling the capillary pressure. Typical primary drainage and secondary imbibition capillary pressure curves  $P_c(S_w)$  for systems of different wettabilities were presented by Iglaue et al. (2015), as shown in Fig. 40.  $\text{CO}_2$  will not enter a water-saturated rock ( $S_w = 1$ ) until the capillary entry pressure ( $P_e$ ) is overcome (points A and B, Fig. 40a) in a strongly water-wet system. As  $P_c$  is increased, more water is continuously displaced by  $\text{CO}_2$  until the irreducible water saturation is attained (point C, Fig. 40a). In an intermediate-wet system,  $\text{CO}_2$  enters the rock at  $P_e$ , which is lower than the capillary entry pressure in a strongly water-wet system (point F, Fig. 40b). As  $P_c$  is increased, more water is displaced by  $\text{CO}_2$  until the irreducible water saturation is reached (point G, Fig. 40b). Note that the area under the primary drainage curve is reduced compared to that in a strongly water-wet system because less work is necessary for  $\text{CO}_2$  to displace water in an intermediate-wet system. In a  $\text{CO}_2$ -wet system,  $\text{CO}_2$  displaces water at  $P_c = 0$  until the irreducible water saturation is attained (points J to K, Fig. 40c). During the secondary imbibition process,  $P_c$  decreased, causing water to spontaneously imbibe into the system, but no water is imbibed at negative  $P_c$  values (points D to E, Fig. 40a) in a strongly water-wet system. In contrast to the strongly water-wet case, in an intermediate-wet system, water imbibes into rock at both positive (points G to H, Fig. 40b) and negative (points H to I, Fig. 40b)  $P_c$  values. In a  $\text{CO}_2$ -wet system, as  $P_c$  is decreased, water will only enter the system at negative  $P_c$  values (points K to L, Fig. 40c). In summary, the effect of wettability on capillary pressure during primary drainage and secondary imbibition is essentially dependent on the affinity of rock to water and  $\text{CO}_2$ .

Many researchers have quantitatively evaluated the effect of wettability on capillary pressure characteristics determined by experiments and have qualitatively assessed the system's wettability from  $P_c$  curves. For example, Morrow (1976) investigated the

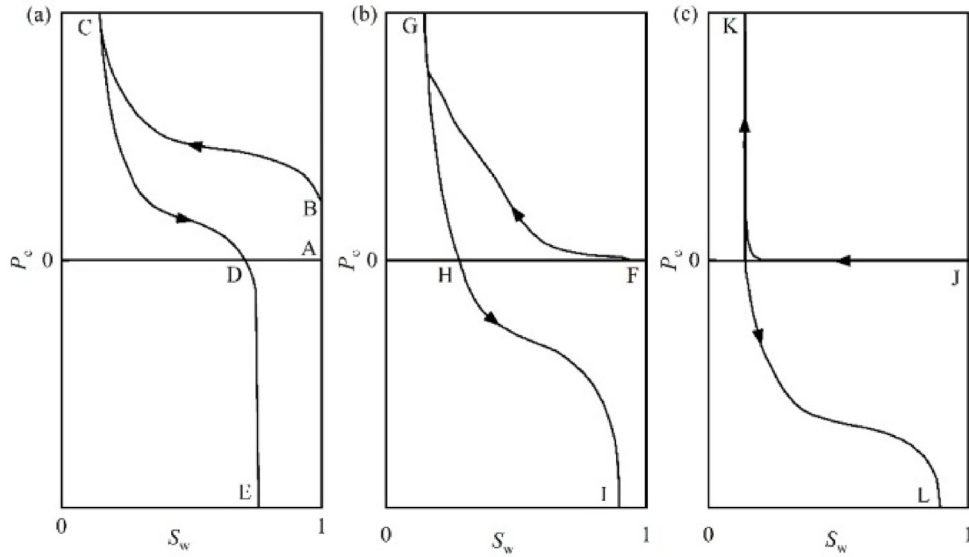


Fig. 40. Capillary pressure curves for (a) a strongly water-wet system, (b) an intermediate-wet system and (c) a CO<sub>2</sub>-wet system (Abdallah et al., 2007; Iglauer et al., 2015).

dependence of capillary pressure on wettability using PTFE porous media. The capillary pressure data were obtained by the porous plate method, and the contact angle was measured on a flat, smooth PTFE surface. According to the drainage capillary pressure results (Fig. 41a), the capillary pressure was almost insensitive to wettability when the contact angle was less than 50°. Furthermore, no measurable effect of the contact angle on the capillary pressure was found for the contact angles less than 22°. Several other researchers (Purcell, 1950; Brown, 1951; Dumore and Schols, 1974) also observed that the wettability had almost no effect on the capillary pressure curves when the contact angle was less than 50°. Morrow (1976) presented spontaneous imbibition capillary pressure curves after drainage capillary pressure measurements (Fig. 41b). The spontaneous imbibition capillary pressure curves were not sensitive to the wettability as the contact angle varied between 0° and 22°. However, the imbibition capillary pressure was sensitive to the wettability for the contact angles larger than 22° due to the different behaviors of the advancing and receding contact angles measured on a rough surface.

**5. Effect of H<sub>2</sub>S content on relative permeability and capillary pressure curves**

Due to the highly toxic and corrosive nature of H<sub>2</sub>S, the only experimental study on the relative permeability and capillary pressure curves of the acid gas/brine/rock systems published in the academic literature was presented by Bennion and Bachu (2006a, 2008b). Notably, because pure CO<sub>2</sub> and H<sub>2</sub>S represent the compositional end members of the acid gas, Bennion and Bachu (2006a, 2008b) measured the displacement characteristics of these two gases under in situ conditions with samples from the Wabamun and Zama areas, Alberta, Canada. In addition, the IFT between brine and CO<sub>2</sub> or H<sub>2</sub>S was also measured under these conditions.

First, all the experimental measurements, including the IFT, capillary pressure and relative permeability measurements, were conducted under in situ reservoir conditions using supercritical pure CO<sub>2</sub> and H<sub>2</sub>S in the core plugs. The IFTs between CO<sub>2</sub> or H<sub>2</sub>S and the equilibrium brine under reservoir conditions were measured by a pendant-drop interfacial tensiometer. The in situ

conditions of rock samples and the IFTs between CO<sub>2</sub> or H<sub>2</sub>S and equilibrium brine under reservoir conditions are shown in Table 7. The IFT between H<sub>2</sub>S and its equilibrium H<sub>2</sub>S-saturated brine was lower than that between the supercritical CO<sub>2</sub> and its equilibrium CO<sub>2</sub>-saturated brine. The lower IFT could be because the solubility of the H<sub>2</sub>S in the brine is greater than that of CO<sub>2</sub> in the brine.

The relative permeability for CO<sub>2</sub> and H<sub>2</sub>S was measured by laboratory coreflood experiments. Due to the highly toxic and corrosive nature of H<sub>2</sub>S, special core holder cells, pumps, and displacement equipment, which were composed of Hastelloy C or titanium, were used in the coreflood experiments. The CO<sub>2</sub>/brine and H<sub>2</sub>S/brine relative permeability curves were generated by computer history matching of the laboratory experimental data. Furthermore, Bennion and Bachu (2008b) presented the parameters for Corey-type relative permeability functions, which were used to generate the CO<sub>2</sub>/brine and H<sub>2</sub>S/brine relative permeability curves.

Corey-type relative permeability functions, which are functions of phase saturations raised to a power, are often represented in numerical and mathematical reservoir simulators (Orr, 2007; Mathias et al., 2013). In the relative permeability relations, we have

$$k_{rw} = k_{rw0} \left( \frac{S_w - S_{wr}}{1 - S_{gr} - S_{wr}} \right)^m \tag{24}$$

$$k_{rg} = k_{rg0} \left( \frac{S_g - S_{gr}}{1 - S_{gr} - S_{wr}} \right)^n \tag{25}$$

where  $k_r$  and  $S$  are the relative permeability and saturation, respectively; the subscripts  $w$  and  $g$  stand for water and gas; the subscript  $r$  stands for residual;  $m$  and  $n$  are power-law exponents for the water and gas phases; and  $k_{rw0}$  and  $k_{rg0}$  are the end-point values of the water and gas relative permeabilities, respectively.

Fig. 42 presents the relative permeability curves of CO<sub>2</sub>-brine and H<sub>2</sub>S-brine for the drainage and imbibition processes, and Table 8 presents the parameters of the Corey-type relative permeability functions.

There is no consensus on the effect of H<sub>2</sub>S content on the relative permeability curves for the four rock samples. As shown in Fig. 43,

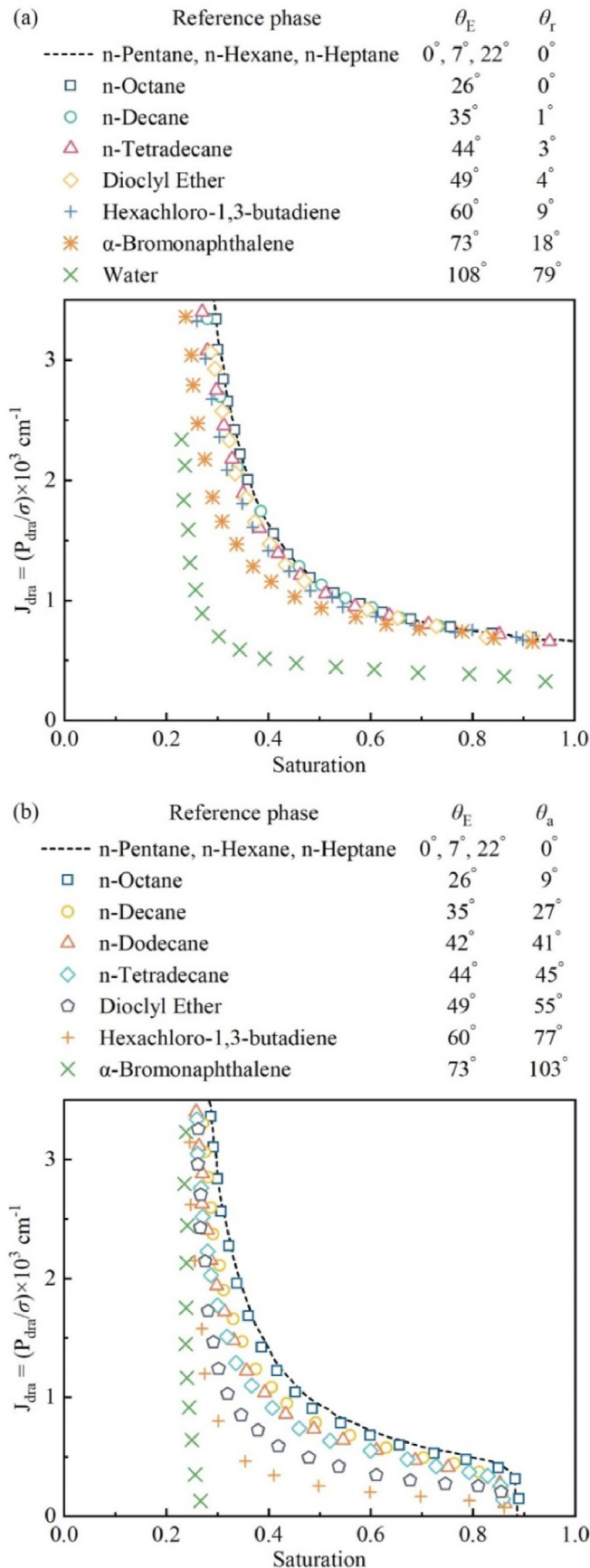


Fig. 41. Effects of wettability on the capillary pressure of PTFE cores with air and liquid (a) during the drainage process and (b) during the imbibition process (Morrow, 1976).

the residual gas saturation decreased with increasing H<sub>2</sub>S mole fraction for the Viking and Calmar formations, possibly due to the reduction in the capillary pressure with decreasing IFT. However, for the Nisku formation, the residual gas saturation increased slightly with increase in the H<sub>2</sub>S mole fraction.

The residual water saturation increased with increasing H<sub>2</sub>S mole fraction for the Viking, Nisku and Muskeg formations. However, for the Calmar formation, the residual water saturation decreased with increasing H<sub>2</sub>S mole fraction (Fig. 43). The results were attributed to the wettability changes; that is, the residual water saturation increased when the uniformly wetted system became more water-wet. As shown in Fig. 42, the saturation at which the water and gas relative permeabilities are equally increased as the H<sub>2</sub>S mole fraction increased for the Viking and Nisku formations. Thus, the rock/water/gas system is more water-wet based on Craig's rules of thumb (Table 6). For the Calmar formation, the saturation at which the water and gas relative permeabilities are equally decreased, and thus, the rock/water/gas system is less water-wet as the H<sub>2</sub>S mole fraction increases.

Note that the relative permeability to the brine phase is higher at a lower residual gas saturation. As shown in Fig. 44, the endpoint relative permeability to the brine phase decreased for the Nisku formation and increased for the Calmar formation as the H<sub>2</sub>S mole fraction increased, which was consistent with the higher residual gas saturation for the Nisku formation and lower residual gas saturation for the Calmar formation in the H<sub>2</sub>S test. However, for the Viking formation, the lower endpoint relative permeability to the brine phase is not consistent with decrease in the residual gas saturation with increasing H<sub>2</sub>S mole fraction.

Similarly, relative permeability to the gas phase is higher at a lower residual water saturation. Thus, the endpoint relative permeability to gas phase decreased for the Viking and Muskeg formations and increased for the Calmar formation. However, for the Nisku formation, the higher endpoint relative permeability to the brine phase is not consistent with increase in the residual gas saturation and H<sub>2</sub>S mole fraction.

The gas relative permeability at a water saturation of 0.7 increased with increasing H<sub>2</sub>S mole fraction for all formations during both drainage and imbibition processes (Fig. 45), due to higher gas mobility caused by lower IFT at higher H<sub>2</sub>S mole fractions. The brine relative permeability correspondingly decreased with increase in the H<sub>2</sub>S mole fraction for the Viking and Muskeg formations during both drainage and imbibition processes. However, the brine relative permeability increased with the in the H<sub>2</sub>S mole fraction for the Calmar formation during both drainage and imbibition processes. For the Nisku formation, the brine relative permeability increased during the drainage process and decreased during the imbibition process with increasing H<sub>2</sub>S mole fraction. It is difficult to directly compare the CO<sub>2</sub>- and H<sub>2</sub>S-test results of the four samples.

A high-pressure air-mercury capillary pressure apparatus was used to measure the capillary pressure. The corresponding 2.5 cm diameter sample rock chips were taken from the endcap sections of the plugs that were tested for the relative permeability. Fig. 46 shows the comparison of the capillary pressures with CO<sub>2</sub>/brine and with H<sub>2</sub>S/brine in the Viking sandstone and in the Nisku carbonate.

As shown in Fig. 47, the capillary pressure at a water saturation of 0.7 decreased with increasing H<sub>2</sub>S mole fraction. This lower capillary pressure can be attributed to the significant reduction in the IFT at higher H<sub>2</sub>S mole fractions under in situ conditions. Furthermore, the capillary entry pressure with H<sub>2</sub>S/brine was lower than that with CO<sub>2</sub>/brine (Fig. 46). Since no contact angles were measured during the experiments, it is impossible to conclude whether the wettability of H<sub>2</sub>S/brine and CO<sub>2</sub>/brine systems affects the capillary entry pressure.

**Table 7**

In situ conditions for rock samples from the Wabamun and Zama areas, Alberta, Canada, used in the analysis of relative permeability and displacement characteristics of CO<sub>2</sub>/brine and H<sub>2</sub>S/brine systems (Bennion and Bachu, 2008b).

Unit	Lithology	Depth (m)	Pressure (MPa)	Temperature (K)	Brine salinity (mg/L)	Porosity (%)	Absolute permeability (mD)	IFT to CO <sub>2</sub> (mN/m)	IFT to H <sub>2</sub> S (mN/m)
Viking #2	Sandstone	1342	8.6	308	28300	19.5	21.72	32.1 <sup>a</sup>	12.2 <sup>a</sup>
Nisku #2	Carbonate	1953	17.4	329	136800	11.4	21.02	34.6 <sup>a</sup>	12.3 <sup>a</sup>
Calmar	Shale	1566	12.25	316	129700	3.9	$2.94 \times 10^{-6}$	27.6 <sup>b</sup>	16 <sup>d</sup>
Muskeg*	Anhydrite	1491	15	344	189800	1.2	$0.0003.54 \times 10^{-4}$	30 <sup>c</sup>	7.0 <sup>d</sup>

\* Sample from the Zama oil field in northwestern Alberta. All other samples were from the Wabamun/Pembina oil field in central Alberta.

<sup>a</sup> IFT values for the Viking #2 sandstone and Nisku #2 carbonate were obtained from Bennion and Bachu (2006a).

<sup>b</sup> IFT to CO<sub>2</sub> for Calmar shale was obtained from Bachu and Bennion (2008).

<sup>c</sup> IFT to CO<sub>2</sub> for Muskeg anhydrite was obtained from Chalbaud et al. (2009).

<sup>d</sup> IFT to H<sub>2</sub>S for Calmar shale and Muskeg anhydrite were interpolated from values obtained by Shah et al. (2008a).

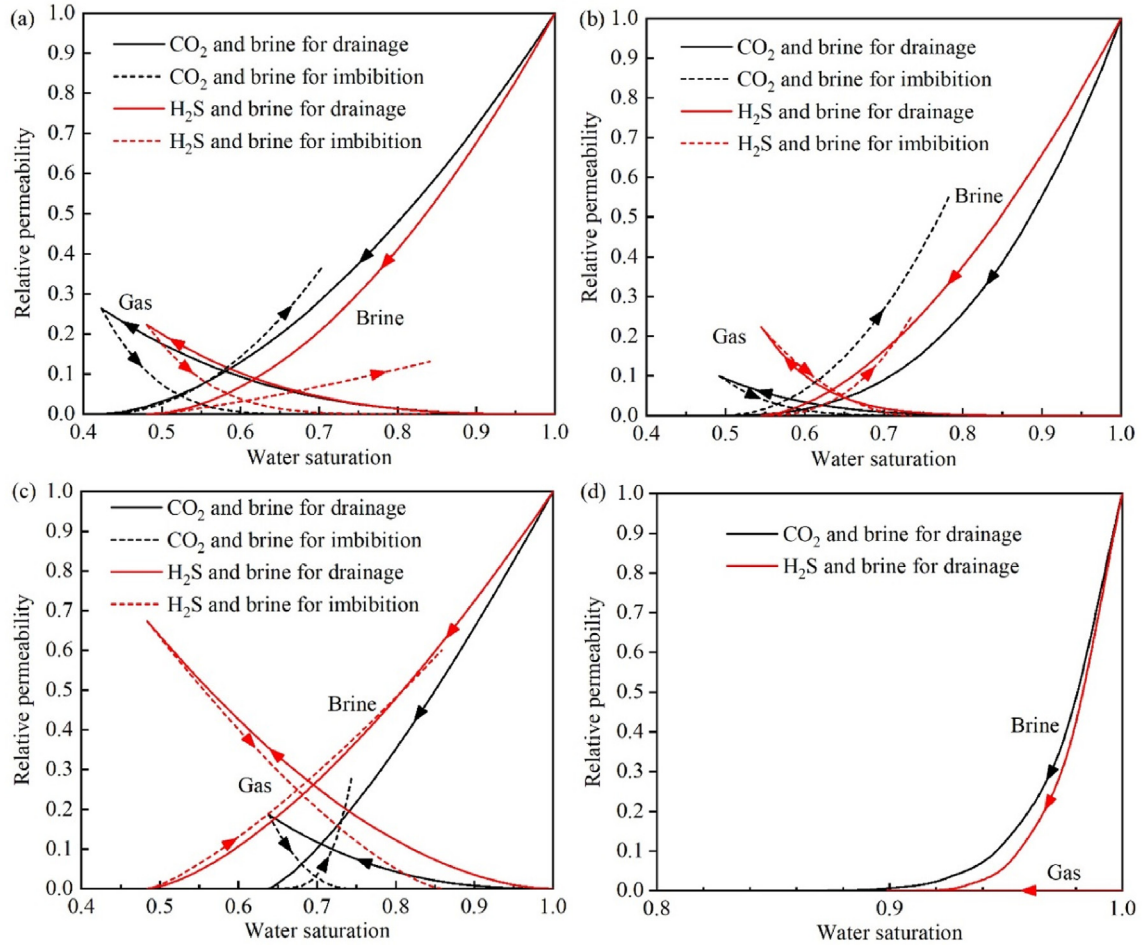


**Fig. 42.** Comparison between the relative permeabilities of CO<sub>2</sub>-brine and H<sub>2</sub>S-brine during the drainage and imbibition processes in the (a) Viking formation, (b) Nisku formation, (c) Calmar formation and (d) Muskeg formation (Bennion and Bachu, 2008b).

**Table 8**

Relative permeability parameters for CO<sub>2</sub>/brine and H<sub>2</sub>S/brine systems during the drainage and imbibition processes for rock samples from the Wabamun and Zama areas, Alberta, Canada (Bennion and Bachu, 2008b).

Unit	Drainage process								Imbibition process							
	CO <sub>2</sub> /Brine system				H <sub>2</sub> S/Brine system				CO <sub>2</sub> /Brine system				H <sub>2</sub> S/Brine system			
	$k_{rg0}$	$S_{wr}$	m	n	$k_{rg0}$	$S_{wr}$	m	n	$k_{rw0}$	$S_{gr}$	m	n	$k_{rw0}$	$S_{gr}$	m	n
Viking #2	0.2638	0.423	1.7	2.8	0.2223	0.481	1.8	3.0	0.365	0.297	2.1	4.0	0.1312	0.159	1.3	4.5
Nisku #2	0.0999	0.492	2.7	4.6	0.2231	0.545	1.7	6.2	0.55	0.218	2.1	4.4	0.2485	0.265	2.2	4.4
Calmar	0.1875	0.638	1.3	2.5	0.673	0.484	1.5	1.8	0.282	0.256	4	2.2	0.6008	0.141	1.3	1.4
Muskeg	0.0000828	0.815	6.6	2.7	0.0000298	0.899	4.0	7.5	—	0.18	—	—	—	—	—	—

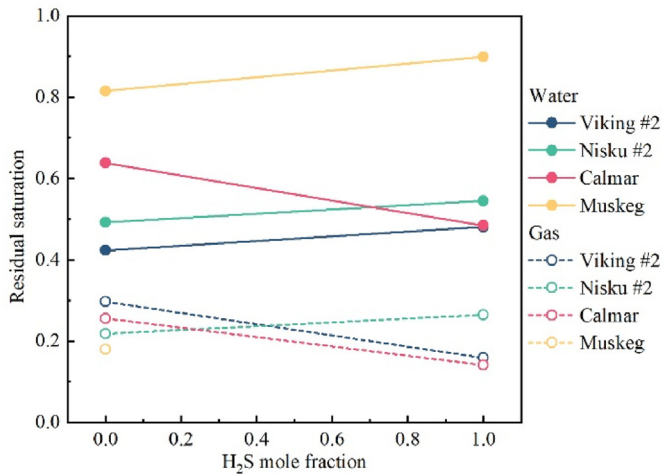


Fig. 43. Effects of the H<sub>2</sub>S content on residual saturation.

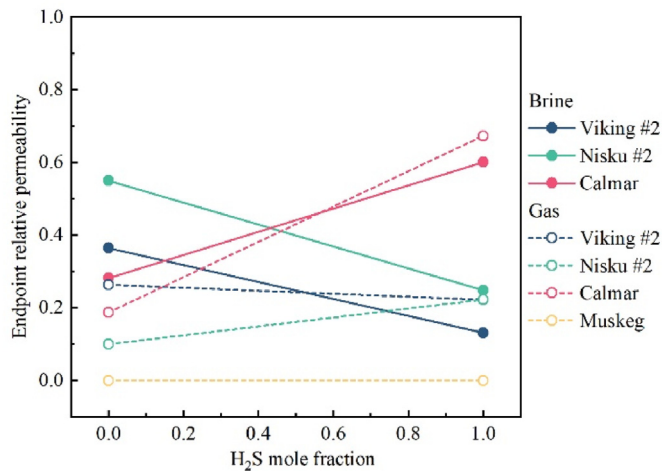


Fig. 44. Effects of the H<sub>2</sub>S content on endpoint relative permeability.

## 6. Discussion

The existing experimental data and theoretical models were reviewed to explore how H<sub>2</sub>S content affects the thermophysical properties of the acid gas. The development of better theoretical models requires abundant experimental data, and semitheoretical models cannot be more accurate than the experimental data to which they are fitted. Regarding the density of acid gas, the available data for the pure CO<sub>2</sub> and H<sub>2</sub>S are sufficient in this context. However, only limited experimental data are available for the densities of CO<sub>2</sub>–H<sub>2</sub>S mixtures, covering only a small range of the temperatures, pressures and H<sub>2</sub>S contents of interest. For the viscosity of the acid gas, high-quality data exist for the pure CO<sub>2</sub>, but only limited data are available for the pure H<sub>2</sub>S. There are currently no available viscosity data for the CO<sub>2</sub>–H<sub>2</sub>S mixtures. Experimental measurement of the thermophysical properties of acid gas, especially the CO<sub>2</sub>–H<sub>2</sub>S mixtures, remains an important topic in future study.

It is necessary to consider the variation in the H<sub>2</sub>S content in acid gas geological sequestration. The preceding review shows that as the H<sub>2</sub>S content varies in the geological co-storage of CO<sub>2</sub> and H<sub>2</sub>S, the acid gas viscosity, IFT and wettability can be altered.

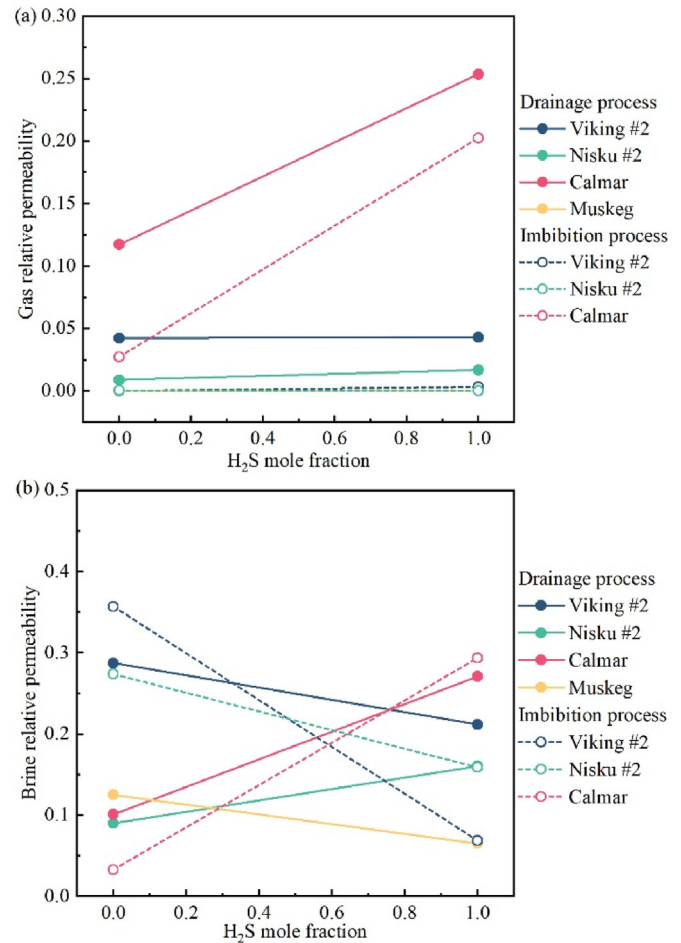


Fig. 45. Effects of the H<sub>2</sub>S content on (a) gas relative permeability and (b) brine relative permeability at a water saturation of 0.7.

However, there is only a single dataset available on the IFT of a CO<sub>2</sub>–H<sub>2</sub>S mixture provided by Shah et al. (2008a). Hence, considerable attention should be paid to IFT measurements of the CO<sub>2</sub>–H<sub>2</sub>S mixtures in future studies. Furthermore, it is unreasonable to expect the effect of the H<sub>2</sub>S content on the wettability of rock minerals to be the same in all rock-fluid systems. Only a few experimental data points on the water contact angle of acid gases (CO<sub>2</sub>, H<sub>2</sub>S and their mixtures) on quartz, calcite and mica substrates are available, and data on the water contact angle of acid gases (CO<sub>2</sub>, H<sub>2</sub>S and their mixtures) on biotite mica, feldspar, montmorillonite, kaolinite, illite and smectite mudrocks are rare. Experimental measurements are desired to investigate the effect of the H<sub>2</sub>S content on the wettability of caprocks and storage rocks for acid gas geological sequestration.

In rock/oil/water system, the effect of wettability on the relative permeability and capillary pressure characteristics has been well investigated. Wettability is a major control of the location, flow and spatial distribution of fluids in rock. Thus, the wettability has been shown to affect the relative permeability, residual saturation, endpoint relative permeability and capillary pressure curves. In contrast, there are few experimental data points of the relative permeability and capillary pressure of the acid gas/water/rock system. However, the results demonstrate that the influence of wettability on relative permeability and capillary pressure characteristics in acid gas/water/rock system is similar to that in oil/water/rock system. For instance, the typical capillary pressure curves of

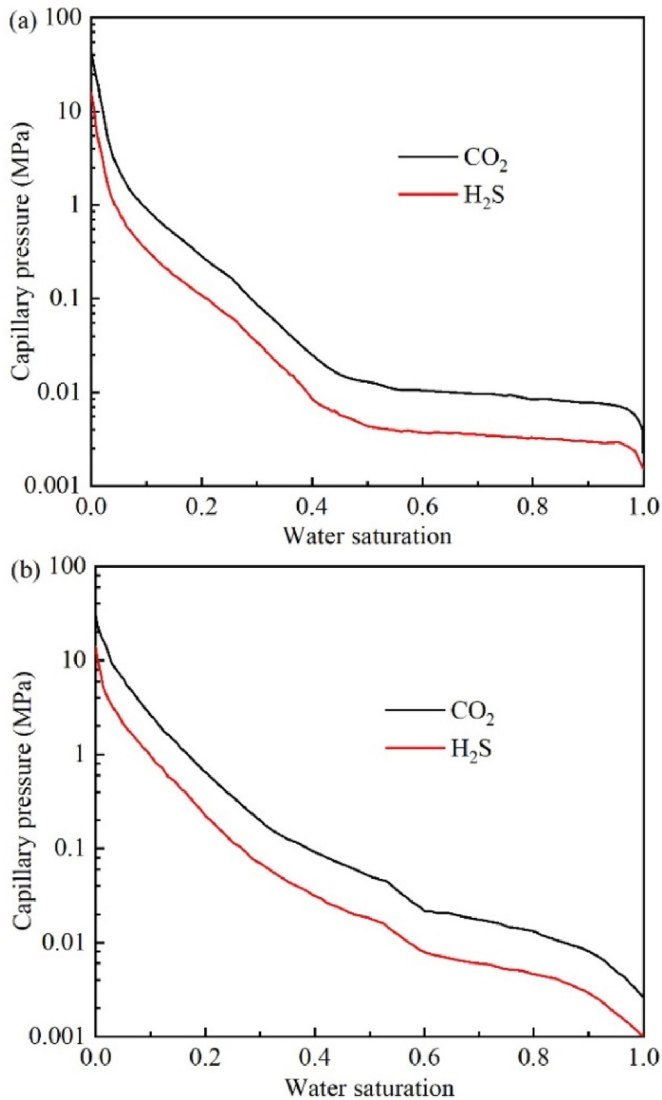


Fig. 46. Comparison of the capillary pressure with CO<sub>2</sub>-brine and H<sub>2</sub>S-brine in the (a) Viking formation and (b) Nisku formation (Bennion and Bachu, 2006a).

the acid gas/water/rock systems with different wettabilities presented by Iglaer et al. (2015) are consistent with capillary pressure characteristics of oil/water/rock systems with different contact angles determined experimentally by Morrow (1976).

Furthermore, whether in the acid gas/water/rock system or in the oil/water/rock system, the wetting fluid fills the narrowest regions of the pore space and is poorly connected, stranding the nonwetting phase in the larger pores. It would be sensible to conduct experimental measurements in the reservoir systems that have a high potential for the acid gas geological sequestration. The experimental work should include not only relative permeability and capillary pressure tests but also wettability measurements. Without such experimental measurements, it is preferable to construct the relative permeability and capillary pressure curves of acid gases under different wettability conditions based on the data of the oil/water/rock system (Al-Khdheawi et al., 2017a; b, 2018).

For the effect of the IFT on the relative permeability characteristic, only Bennion and Bachu (2005, 2006b, c) focused on the CO<sub>2</sub>/brine system in the CO<sub>2</sub> geological storage. Other studies (Talash, 1976; Batycky and McCaffery, 1978; Bardon and Longeron, 1980;

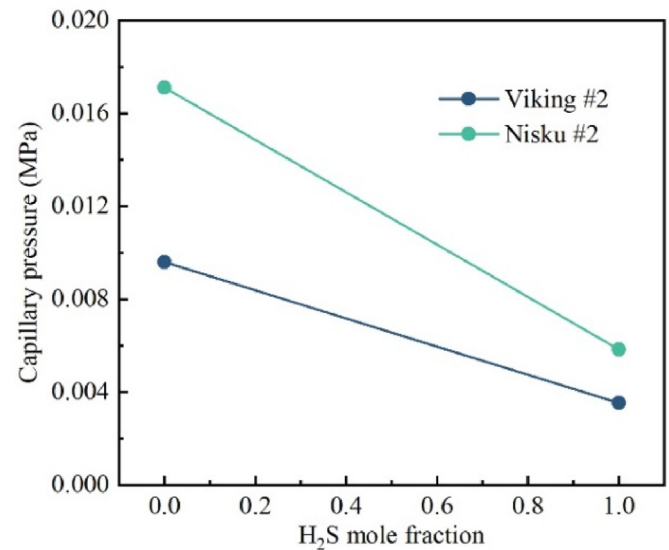


Fig. 47. Effects of the H<sub>2</sub>S content on capillary pressure at a water saturation of 0.7.

Amaefule and Handy, 1982; Torabzadey and Handy, 1984; Asar and Handy, 1988; Shen et al., 2010) investigated the effect of the IFT on the relative permeability nonlinearity for the oil/brine or gas systems. Notably, Talash (1976), Asar and Handy (1988) and Bennion and Bachu (2005, 2006b, c) conducted experimental tests in oil/brine, gas/oil and CO<sub>2</sub>/brine systems, respectively. However, in their studies, a consistent finding was reported that the relative permeability of both the wetting and nonwetting phases increased with decreasing the IFT at a given water saturation.

In addition, for the IFT effect on the relative permeability characteristic, only Shen et al. (2010) isolated the impact of the IFT on the relative permeability. They found there may exist a crucial IFT value below and above which the influences of IFT on relative permeability are very different. Regarding the effect of IFT on the relative permeability characteristics investigated by other researchers, the viscosity, flow velocity and viscosity ratio also changed when the test conditions were changed to obtain different IFT levels (Talash, 1976; Batycky and McCaffery, 1978; Bardon and Longeron, 1980; Amaefule and Handy, 1982; Torabzadey and Handy, 1984; Asar and Handy, 1988; Bennion and Bachu, 2005, 2006b, c). Under these circumstances, the relative permeability, residual saturation, and endpoint relative permeability are functions of both the individual variables and the capillary number. However, there is no consistency in the effect of the capillary number on the relative permeability characteristics.

Furthermore, both the viscosity of the acid gas and IFT of acid gas/water system change with the variation of the H<sub>2</sub>S content in acid gas geological sequestration. Thus, we proposed that further investigation of the effect of IFT and viscosity on acid gas/brine relative permeability and capillary pressure characteristics in acid gas geological sequestration is necessary.

In the present study, the focus is on the alterations of the interfacial characteristics of the acid gas/brine/rock system and thermophysical properties induced by changes in the H<sub>2</sub>S content and how these alterations affect the relative permeability and capillary pressure characteristics. The geochemical effects of the H<sub>2</sub>S content in the acid gas injection are not considered. However, compared with the pure CO<sub>2</sub> injection, the co-injection of CO<sub>2</sub>-H<sub>2</sub>S resulted in decrease of pH, and then the lower pH drove more severe corrosion of the primary minerals (e.g. feldspar, basalts, oligoclase, calcite and chlorite), favoring more secondary mineral to

be formed, such as amorphous quartz, kaolinites, anhydrite and pyrite (Schaefer et al., 2010, 2013; Li et al., 2016). Particularly, the precipitation of pyrite may partially inhibit the precipitation of Fe-bearing carbonate minerals such as ankerite in the H<sub>2</sub>S–CO<sub>2</sub>–brine–sandstone interaction (Li et al., 2016). Pore dimension and morphology may change due to mineral precipitation and dissolution, affecting the wettability heterogeneity, capillary pressure and relative permeability. Thus, the alterations of geochemical interaction of acid gas/brine/rock systems induced by changes in the H<sub>2</sub>S content and how these alterations affect the relative permeability and capillary pressure characteristics need further research.

In conclusion, it would be advisable to conduct experimental measurements in reservoir systems that have a high potential for acid gas geological sequestration. The experimental work should include not only relative permeability and capillary pressure tests but also measurements of the viscosity, IFT, wettability and geochemical reactions.

## 7. Conclusions

The effects of the H<sub>2</sub>S content on the relative permeability and capillary pressure characteristics in the acid gas geological sequestration are considered in this paper. The alteration in the viscosity, IFT and wettability induced by the variation in the H<sub>2</sub>S content has a significant impact on the relative permeability and capillary pressure characteristics. This has important implications for ascertaining acid gas injectivity and migration and assessing the suitability and safety of prospective acid gas sequestration sites. Key findings are given below.

- (1) The H<sub>2</sub>S mole fraction has a larger control on the CO<sub>2</sub>–H<sub>2</sub>S mixture fluid density in a liquid or supercritical phase than in a gas phase. When the temperature and pressure conditions approach the phase boundaries, the densities of CO<sub>2</sub>–H<sub>2</sub>S mixtures increase with increasing H<sub>2</sub>S mole fraction. However, when the temperature and pressure conditions are far from the phase boundaries, the densities of the CO<sub>2</sub>–H<sub>2</sub>S mixtures decrease with increasing H<sub>2</sub>S mole fraction.
- (2) In the gas phase, the viscosities of CO<sub>2</sub>–H<sub>2</sub>S mixtures decrease with increasing H<sub>2</sub>S mole fraction. However, in the liquid phase, the viscosities of the CO<sub>2</sub>–H<sub>2</sub>S mixtures increase with increasing H<sub>2</sub>S mole fraction. Furthermore, there exists a range where the viscosities of CO<sub>2</sub>–H<sub>2</sub>S mixtures with different H<sub>2</sub>S mole fractions are almost the same in the supercritical phase.
- (3) The water/acid gas IFT decreases strongly with increasing H<sub>2</sub>S content. In particular, the IFT between a CO<sub>2</sub>–H<sub>2</sub>S mixture and water is proportional to the CO<sub>2</sub> (or H<sub>2</sub>S) mole fraction in the acid gas if the acid gas is under the supercritical conditions.
- (4) The effect of the H<sub>2</sub>S content on the wettability of gas/water/rock systems is suggested to depend on the type of mineral substrate. The wetting behavior of carbonate-rich Rousse rock with H<sub>2</sub>S in a low-salinity brine does not exhibit significant changes and remains water-wet compared to that in the presence of CO<sub>2</sub>. In contrast, mica is less water-wet when the H<sub>2</sub>S is gaseous. Furthermore, a wettability reversal of mica to H<sub>2</sub>S-wet behavior occurs when H<sub>2</sub>S is liquid. For a clean quartz surface, the contact angle of the quartz/water/H<sub>2</sub>S system is larger than that of the analogous quartz/water/CO<sub>2</sub> system. However, for quartz substrates contaminated with hydroxyl groups, the contact angle of the quartz/water/H<sub>2</sub>S system is similar to that observed with the quartz/water/CO<sub>2</sub> system.

- (5) At a given saturation, the capillary pressure decreases with decreasing IFT. As IFT decreases, the capillary pressure curve shifts toward lower water saturations. Regarding the effect of the IFT on the relative permeability characteristics, there is no consistency in the effect of the capillary number on the relative permeability characteristics.
- (6) At a given saturation, the relative permeability of a fluid is higher when it is the nonwetting phase in a system than when it is the wetting phase in another system. Both residual wetting and nonwetting phases are affected by wettability. Although there are conflicting results among different systems, it appears that residual water saturation increases when a uniformly wetted system becomes more water-wet. Meanwhile, the residual gas saturation increases when the uniformly wetted system becomes more water-wet. When the system is more water-wet, the endpoint relative permeability to water is lower, while the endpoint relative permeability to gas is higher. At a given saturation, the capillary pressure increases when the system becomes more water-wet.
- (7) The capillary pressure at a constant water saturation decreased with increasing the H<sub>2</sub>S mole fraction due to the lower capillary pressure at higher H<sub>2</sub>S mole fractions in acid gas. However, it is difficult to obtain the relative permeability characteristics at different H<sub>2</sub>S mole fractions in acid gas due to the influence of multiple factors, such as IFT and wettability.

Nevertheless, the issue of the effect of the H<sub>2</sub>S content on the relative permeability and capillary pressure characteristics is not yet fully resolved. The recommendations are as follows:

- (1) To obtain a better understanding of the effect of the H<sub>2</sub>S content on the thermophysical properties, further experimental work is required, with a focus on the densities and viscosities of CO<sub>2</sub>–H<sub>2</sub>S mixtures for a wide range of temperatures, pressures and H<sub>2</sub>S contents of the acid gas.
- (2) The IFT and wettability influenced by the H<sub>2</sub>S content in different acid gas/water/rock systems have not been fully investigated. Furthermore, the effect of viscosity, IFT and wettability of acid gas/water/rock systems on relative permeability and capillary pressure characteristics is an important topic for future studies.
- (3) The H<sub>2</sub>S content may affect the mineral precipitation and dissolution in the H<sub>2</sub>S–CO<sub>2</sub>–brine–rock interaction, and then change the pore dimension and morphology. Hence, the alterations of geochemical interaction of the acid gas/brine/rock systems induced by changes in the H<sub>2</sub>S content and how these alterations affect the relative permeability and capillary pressure characteristics need further research.
- (4) Due to the lack of consensus on the universal effect of H<sub>2</sub>S content on the relative permeability and capillary pressure characteristics in all rock-fluid systems, it is advisable to perform experimental measurements relevant to acid gas geological sequestration.

## Declaration of competing interest

The authors declare that they have no known competing financial interests or personal relationships that could have appeared to influence the work reported in this paper.

## Acknowledgments

The research was partially supported by the National Natural Science Foundation of China (Grant Nos. 41872210 and 41274111) and the Open Research Fund of State Key Laboratory of Geomechanics and Geotechnical Engineering (Grant No. Z018002).

## References

- Abdallah, W., Buckley, J.S., Carnegie, A., et al., 2007. Fundamentals of wettability. *Oilfield Rev.* 19, 44–61.
- Abrams, A., 1975. The influence of fluid viscosity, interfacial tension, and flow velocity on residual oil saturation left by waterflood. *Soc. Petrol. Eng. J.* 15 (5), 437–447.
- Al-Khdheawi, E.A., Vialle, S., Barifcani, A., Sarmadivaleh, M., Iglauer, S., 2017a. Impact of reservoir wettability and heterogeneity on CO<sub>2</sub>-plume migration and trapping capacity. *Int. J. Greenh. Gas Control* 58, 142–158.
- Al-Khdheawi, E.A., Vialle, S., Barifcani, A., Sarmadivaleh, M., Iglauer, S., 2017b. Influence of CO<sub>2</sub>-wettability on CO<sub>2</sub> migration and trapping capacity in deep saline aquifers. *Greenh. Gases* 7 (2), 328–338.
- Al-Khdheawi, E.A., Vialle, S., Barifcani, A., Sarmadivaleh, M., Iglauer, S., 2018. Effect of wettability heterogeneity and reservoir temperature on CO<sub>2</sub> storage efficiency in deep saline aquifers. *Int. J. Greenh. Gas Control* 68, 216–229.
- Alfredsson, H.A., Oelkers, E.H., Hardarsson, B.S., Franzson, H., Gunnlaugsson, E., Gislason, S.R., 2013. The geology and water chemistry of the Hellisheidi, SW-Iceland carbon storage site. *Int. J. Greenh. Gas Control* 12, 399–418.
- Alyafei, N., Blunt, M.J., 2016. The effect of wettability on capillary trapping in carbonates. *Adv. Water Resour.* 90, 36–50.
- Amaefule, J.O., Handy, L.L., 1982. The effect of interfacial tensions on relative oil/water permeabilities of consolidated porous media. *Soc. Petrol. Eng. J.* 22 (3), 371–381.
- Aradóttir, E.S.P., Gunnarsson, I., Sigfússon, B., et al., 2015. Towards Cleaner Geothermal Energy: Subsurface Sequestration of Sour Gas Emissions from Geothermal Power Plants. *World Geothermal Congress 2015*, Melbourne, Australia, pp. 1–13.
- Asar, H., Handy, L.L., 1988. Influence of interfacial tension on gas/oil relative permeability in a gas-condensate system. *SPE Reservoir Eng.* 3 (1), 257–264.
- Bachu, S., 2000. Sequestration of CO<sub>2</sub> in geological media: criteria and approach for site selection in response to climate change. *Energy Convers. Manag.* 41 (9), 953–970.
- Bachu, S., 2015. Review of CO<sub>2</sub> storage efficiency in deep saline aquifers. *Int. J. Greenh. Gas Control* 40, 188–202.
- Bachu, S., Adams, J.J., Michael, K., Buschkuehle, B.E., 2003. Acid gas injection in the Alberta basin: a commercial-scale analogue for CO<sub>2</sub> geological sequestration in sedimentary basins. In: *Second Annual Conference on Carbon Sequestration: Developing & Validating the Technology Base to Reduce Carbon Intensity*. NETL, Alexandria, VA, USA, pp. 1–11.
- Bachu, S., Bennion, D.B., 2008. Effects of in-situ conditions on relative permeability characteristics of CO<sub>2</sub>-brine systems. *Environ. Geol.* 54 (8), 1707–1722.
- Bachu, S., Bennion, D.B., 2009a. Chromatographic partitioning of impurities contained in a CO<sub>2</sub> stream injected into a deep saline aquifer: Part 1. Effects of gas composition and in situ conditions. *Int. J. Greenh. Gas Control* 3 (4), 458–467.
- Bachu, S., Bennion, D.B., 2009b. Dependence of CO<sub>2</sub>-brine interfacial tension on aquifer pressure, temperature and water salinity. *Energy Proc.* 1 (1), 3157–3164.
- Bachu, S., Bennion, D.B., 2009c. Interfacial tension between CO<sub>2</sub>, freshwater, and brine in the range of pressure from (2 to 27) MPa, temperature from (20 to 125) °C, and water salinity from (0 to 334000) mg·L<sup>-1</sup>. *J. Chem. Eng. Data* 54 (3), 765–775.
- Bachu, S., Carroll, J.J., 2005. In-situ phase and thermodynamic properties of resident brine and acid gases (CO<sub>2</sub> and H<sub>2</sub>S) injected into geological formations in western Canada. In: Rubin, E.S., Keith, D.W., Gilboy, C.F., Wilson, M., Morris, T., Gale, J., Thambimuthu, K. (Eds.), *Greenhouse Gas Control Technologies 7*. Elsevier Science Ltd, Oxford, pp. 449–457.
- Bachu, S., Mehran, P.D., Hong, H., 2009. Chromatographic partitioning of impurities (H<sub>2</sub>S) contained in a CO<sub>2</sub> stream injected into a deep saline aquifer: Part 2. Effects of flow conditions. *Int. J. Greenh. Gas Control* 3 (4), 468–473.
- Bardon, C., Longener, D.G., 1980. Influence of very low interfacial tensions on relative permeability. *Soc. Petrol. Eng. J.* 20 (5), 391–401.
- Batycky, J.P., McCaffery, F.G., 1978. Low interfacial tension displacement studies. In: *Annual Technical Meeting*. Petroleum Society of Canada, Calgary, Alberta, Canada, pp. 1–13.
- Bennion, D.B., Bachu, S., 2005. Relative permeability characteristics for supercritical CO<sub>2</sub> displacing water in a variety of potential sequestration zones. In: *SPE Annual Technical Conference and Exhibition*. Society of Petroleum Engineers, Dallas, Texas, USA.
- Bennion, D.B., Bachu, S., 2006a. Supercritical CO<sub>2</sub> and H<sub>2</sub>S-brine drainage and imbibition relative permeability relationships for intergranular sandstone and carbonate formations. In: *SPE Europec/EAGE Annual Conference and Exhibition*. Society of Petroleum Engineers, Vienna, Austria.
- Bennion, D.B., Bachu, S., 2006b. Dependence on temperature, pressure, and salinity of the IFT and relative permeability displacement characteristics of CO<sub>2</sub> injected in deep saline aquifers. In: *SPE Annual Technical Conference and Exhibition*. Society of Petroleum Engineers, San Antonio, Texas, USA.
- Bennion, D.B., Bachu, S., 2006c. The impact of interfacial tension and pore size distribution/capillary pressure character on CO<sub>2</sub> relative permeability at reservoir conditions in CO<sub>2</sub>-brine systems. In: *SPE/DOE Symposium on Improved Oil Recovery*. Society of Petroleum Engineers, Tulsa, Oklahoma, USA.
- Bennion, D.B., Bachu, S., 2007. Permeability and Relative Permeability Measurements at Reservoir Conditions for CO<sub>2</sub>-water Systems in Ultralow Ultralow-Permeability Confining Caprocks. *EUROPEC/EAGE Conference and Exhibition*. Society of Petroleum Engineers, London, UK.
- Bennion, D.B., Bachu, S., 2008a. A correlation of the interfacial tension between supercritical phase CO<sub>2</sub> and equilibrium brines as a function of salinity, temperature and pressure. In: *SPE Annual Technical Conference and Exhibition*. SPE, Denver, Colorado, USA, pp. 1–13.
- Bennion, D.B., Bachu, S., 2008b. Drainage and imbibition relative permeability relationships for supercritical CO<sub>2</sub>/brine and H<sub>2</sub>S/brine systems in intergranular sandstone, carbonate, shale, and anhydrite rocks. *SPE Reservoir Eval. Eng.* 11 (3), 487–496.
- Bierlein, J.A., Kay, W.B., 1953. Phase-equilibrium properties of system carbon dioxide-hydrogen sulfide. *Ind. Eng. Chem.* 45 (3), 618–624.
- Bikkina, P.K., 2011. Contact angle measurements of CO<sub>2</sub>-water-quartz/calcite systems in the perspective of carbon sequestration. *Int. J. Greenh. Gas Control* 5 (5), 1259–1271.
- Bikkina, P.K., 2012. Reply to the comments on “Contact angle measurements of CO<sub>2</sub>-water-quartz/calcite systems in the perspective of carbon sequestration”. *Int. J. Greenh. Gas Control* 7, 263–264.
- Bikkina, P.K., Shoham, O., Uppaluri, R., 2011. Equilibrated interfacial tension data of the CO<sub>2</sub>-water system at high pressures and moderate temperatures. *J. Chem. Eng. Data* 56 (10), 3725–3733.
- Boyle, T.B., Carroll, J.J., 2002. Study determines best methods for calculating acid-gas density. *Oil Gas J.* 100 (2), 45–53.
- British Columbia Geological Survey, 2003. Acid gas injection: a study of existing operations phase I: final report. In: *Ministry of Energy, Mines and Petroleum Resources*. British Columbia Geological Survey, Canada.
- Broseta, D., Tonnet, N., Shah, V., 2012. Are rocks still water-wet in the presence of dense CO<sub>2</sub> or H<sub>2</sub>S? *Geofluids* 12 (4), 280–294.
- Brown, H.W., 1951. Capillary pressure investigations. *J. Petrol. Technol.* 3 (3), 67–74.
- Carroll, J.J., Griffin, P.J., Alkafef, S.F., 2009. Review and Outlook of Subsurface Acid Gas Disposal. *SPE Middle East Oil and Gas Show and Conference*. Society of Petroleum Engineers, Manama, Bahrain.
- Chalabaud, C., Robin, M., Lombard, J.-M., Martin, F., Egermann, P., Bertin, H., 2009. Interfacial tension measurements and wettability evaluation for geological CO<sub>2</sub> storage. *Adv. Water Resour.* 32 (1), 98–109.
- Chaudhary, K., Bayani Cardenas, M., Wolfe, W.W., Maisano, J.A., Ketcham, R.A., Bennett, P.C., 2013. Pore-scale trapping of supercritical CO<sub>2</sub> and the role of grain wettability and shape. *Geophys. Res. Lett.* 40 (15), 3878–3882.
- Chen, C., Wan, J.M., Li, W.Z., Song, Y.C., 2015a. Water contact angles on quartz surfaces under supercritical CO<sub>2</sub> sequestration conditions: experimental and molecular dynamics simulation studies. *Int. J. Greenh. Gas Control* 42, 655–665.
- Chen, C., Zhang, N., Li, W.Z., Song, Y.C., 2015b. Water contact angle dependence with hydroxyl functional groups on silica surfaces under CO<sub>2</sub> sequestration conditions. *Environ. Sci. Technol.* 49 (24), 14680–14687.
- Chen, C., Zhuang, C., Shen, W.J., Li, W.Z., 2018. Effects of impurities on CO<sub>2</sub> sequestration in saline aquifers: perspective of interfacial tension and wettability. *Ind. Eng. Chem. Res.* 57 (1), 371–379.
- Chiquet, P., Broseta, D., Thibeau, S., 2007a. Wettability alteration of caprock minerals by carbon dioxide. *Geofluids* 7 (2), 112–122.
- Chiquet, P., Daridon, J.-L., Broseta, D., Thibeau, S., 2007b. CO<sub>2</sub>/water interfacial tensions under pressure and temperature conditions of CO<sub>2</sub> geological storage. *Energy Convers. Manag.* 48 (3), 736–744.
- Chukwudeme, E.A., Fjelde, I., Abeyinghe, K., Lohne, A., 2014. Effect of interfacial tension on water/oil relative permeability on the basis of history matching to coreflood data. *SPE Reservoir Eval. Eng.* 17 (1), 37–48.
- Chung, T.H., Ajlan, M., Lee, L.L., Starling, K.E., 1988. Generalized multiparameter correlation for nonpolar and polar fluid transport properties. *Ind. Eng. Chem. Res.* 27 (4), 671–679.
- Chung, T.H., Lee, L.L., Starling, K.E., 1984. Applications of kinetic gas theories and multiparameter correlation for prediction of dilute gas viscosity and thermal conductivity. *Ind. Eng. Chem. Fund.* 23 (1), 8–13.
- Clark, D.E., Gunnarsson, I., Aradóttir, E.S., et al., 2018. The chemistry and potential reactivity of the CO<sub>2</sub>-H<sub>2</sub>S charged injected waters at the basaltic CarbFix2 site. *Iceland. Energ. Proced.* 146, 121–128.
- Clark, D.E., Oelkers, E.H., Gunnarsson, I., et al., 2020. CarbFix2: CO<sub>2</sub> and H<sub>2</sub>S mineralization during 3.5 years of continuous injection into basaltic rocks at more than 250 °C. *Geochim. Cosmochim. Acta* 279, 45–66.
- Craig, F.F., 1993. *The Reservoir Engineering Aspects of Waterflooding*. HL Doherty Memorial Fund of AIME, New York, USA.
- Delshad, M., Bhuyan, D., Pope, G.A., Lake, L.W., 1986. Effect of capillary number on the residual saturation of a three-phase micellar solution. In: *SPE Enhanced Oil Recovery Symposium*. Society of Petroleum Engineers, Tulsa, Oklahoma, USA, pp. 1–12.
- Donaldson, E.C., Thomas, R.D., 1971. *Microscopic Observations of Oil Displacement in Water-Wet and Oil-Wet Systems*. Fall Meeting of the Society of Petroleum Engineers of AIME. Society of Petroleum Engineers, New Orleans, Louisiana, USA.

- Donaldson, E.C., Thomas, R.D., Lorenz, P.B., 1969. Wettability determination and its effect on recovery efficiency. *Soc. Petrol. Eng. J.* 9, 13–20.
- Duan, Z.H., Møller, N., Weare, J.H., 1996. A general equation of state for supercritical fluid mixtures and molecular dynamics simulation of mixture PVTX properties. *Geochem. Cosmochim. Acta* 60 (7), 1209–1216.
- Dumore, J.M., Schols, R.S., 1974. Drainage capillary-pressure functions and the influence of connate water. *Soc. Petrol. Eng. J.* 14 (5), 437–444.
- Espinoza, D.N., Santamarina, J.C., 2010. Water-CO<sub>2</sub>-mineral systems: interfacial tension, contact angle, and diffusion-implications to CO<sub>2</sub> geological storage. *Water Resour. Res.* 46 (7), W07537.
- Farokhpour, R., Bjørkvik, B.J.A., Lindeberg, E., Torsæter, O., 2013. Wettability behaviour of CO<sub>2</sub> at storage conditions. *Int. J. Greenh. Gas Control* 12, 18–25.
- Fenghour, A., Wakeham, W.A., Vesovic, V., 1998. The viscosity of carbon dioxide. *J. Phys. Chem. Ref. Data* 27 (1), 31–44.
- Fulcher, R.A., Ertekin, T., Stahl, C.D., 1985. Effect of capillary number and its constituents on two-phase relative permeability curves. *J. Petrol. Technol.* 37 (2), 249–260.
- Garnes, J.M., Mathisen, A.M., Scheie, A., Skauge, A., 1990. Capillary number relations for some north, sea reservoir sandstones. In: *SPE/DOE Enhanced Oil Recovery Symposium*. Society of Petroleum Engineers, Tulsa, Oklahoma, USA, pp. 1–12.
- Georgiadis, A., Maitland, G., Trusler, J.P.M., Bismarck, A., 2010. Interfacial tension measurements of the (H<sub>2</sub>O + CO<sub>2</sub>) system at elevated pressures and temperatures. *J. Chem. Eng. Data* 55 (10), 4168–4175.
- Giri, B.R., Blais, P., Marriott, R.A., 2011. Viscosity and density measurements for sour gas fluids at high temperatures and pressures. In: Wu, Y., Carroll, J.J., Du, Z.M. (Eds.), *Carbon Dioxide Sequestration and Related Technologies*. John Wiley & Sons, Inc., New Jersey, USA, pp. 23–39.
- Gunnarsson, I., Aradóttir, E.S., Oelkers, E.H., Clark, D.E., Arnarson, M.þ., Sigfússon, B., Snæbjörnsdóttir, S.O., Matter, J.M., Stute, M., Júlíusson, B.M., Gíslason, S.R., 2018. The rapid and cost-effective capture and subsurface mineral storage of carbon and sulfur at the CarbFix2 site. *Int. J. Greenh. Gas Control* 79, 117–126.
- Gunnarsson, I., Aradóttir, E.S., Sigfússon, B., Gunnlaugsson, E., Júlíusson, B.M., 2013. Geothermal gas emission from Hellisheiði and Nesjavellir power plants. *Iceland. CRC T.* 37, 785–789.
- Gupta, S.P., Trushenski, S.P., 1979. Micellar flooding-compositional effects on oil displacement. *Soc. Petrol. Eng. J.* 19 (2), 116–128.
- Harbert, L.W., 1983. Low interfacial tension relative permeability. In: *SPE Annual Technical Conference and Exhibition*. Society of Petroleum Engineers, San Francisco, California, USA, pp. 1–8. <https://doi.org/10.2118/12171-MS>.
- Harris, C.C., Jowett, A., Morrow, N.R., 1963. Effect of contact angle on the capillary properties of porous masses. *Trans. Inst. Min. Metall.* 73 (5), 335–351.
- Hebach, A., Oberhof, A., Dahmen, N., Kögel, A., Ederer, H., Dinjus, E., 2002. Interfacial tension at elevated pressures measurements and correlations in the water + carbon dioxide system. *J. Chem. Eng. Data* 47 (6), 1540–1546.
- Herrick, C.S., Gaines, G.L., 1973. Surface tension of saturated anhydrous hydrogen sulfide and the effect of hydrogen sulfide pressure on the surface tension of water. *J. Phys. Chem.* 77 (22), 2703–2707.
- Huang, D.D., Honarpour, M.M., Al-Hussainy, R., 1997. An improved model for relative permeability and capillary pressure incorporating wettability. In: *SCA International Symposium*. Calgary, Canada, pp. 7–10.
- Iglauer, S., 2017. CO<sub>2</sub>-water-rock wettability: variability, influencing factors, and implications for CO<sub>2</sub> geostorage. *Accounts Chem. Res.* 50 (5), 1134–1142.
- Iglauer, S., Favretto, S., Spinelli, G., Schena, G., Blunt, M.J., 2010. X-ray tomography measurements of power-law cluster size distributions for the nonwetting phase in sandstones. *Phys. Rev. E* 82 (5), 056315.
- Iglauer, S., Mathew, M.S., Bresme, F., 2012. Molecular dynamics computations of brine-CO<sub>2</sub> interfacial tensions and brine-CO<sub>2</sub>-quartz contact angles and their effects on structural and residual trapping mechanisms in carbon geo-sequestration. *J. Colloid Interface Sci.* 386 (1), 405–414.
- Iglauer, S., Paluszny, A., Pentland, C.H., Blunt, M.J., 2011. Residual CO<sub>2</sub> imaged with X-ray micro-tomography. *Geophys. Res. Lett.* 38 (21), L21403.
- Iglauer, S., Pentland, C.H., Busch, A., 2015. CO<sub>2</sub> wettability of seal and reservoir rocks and the implications for carbon geo-sequestration. *Water Resour. Res.* 51 (1), 729–774.
- Iglauer, S., Salamah, A., Sarmadivaleh, M., Liu, K.Y., Phan, C., 2014. Contamination of silica surfaces: impact on water-CO<sub>2</sub>-quartz and glass contact angle measurements. *Int. J. Greenh. Gas Control* 22, 325–328.
- Jacquemet, N., Pironon, J., Lagneau, V., Saint-Marc, J., 2012. Armouring of well cement in H<sub>2</sub>S-CO<sub>2</sub> saturated brine by calcite coating - experiments and numerical modelling. *Appl. Geochem.* 27 (3), 782–795.
- Jung, J.-W., Wan, J.M., 2012. Supercritical CO<sub>2</sub> and ionic strength effects on wettability of silica surfaces: equilibrium contact angle measurements. *Energy Fuel* 26 (9), 6053–6059.
- Kamath, J., Meyer, R.F., Nakagawa, F.M., 2001. Understanding waterflood residual oil saturation of four carbonate rock types. In: *SPE Annual Technical Conference and Exhibition*. Society of Petroleum Engineers, New Orleans, Louisiana, USA, pp. 1–10.
- Klewicki, K.J., Kobelski, B., Karimjee, A., Sham, C.H., 2006. Acid Gas Injection in the united states. *Carbon Capture & Sequestration*, Alexandria, VA, USA.
- Kvamme, B., Kuznetsova, T., Hebach, A., Oberhof, A., Lunde, E., 2007. Measurements and modelling of interfacial tension for water + carbon dioxide systems at elevated pressures. *Comput. Mater. Sci.* 38 (3), 506–513.
- Laesecke, A., Muzny, C.D., 2017. Reference correlation for the viscosity of carbon dioxide. *J. Phys. Chem. Ref. Data* 46 (1), 013107.
- Lake, L.W., 1989. *Enhanced Oil Recovery*. Old Tappan. Prentice Hall Inc., United States, NJ.
- Lau, W.W.R., Hwang, C.A., Holste, J.C., Hall, K.R., 1997. Densities of carbon dioxide + ethane mixtures from 240 K to 450 K at pressures up to 35 MPa. *J. Chem. Eng. Data* 42, 900–902.
- Lefebvre, E.J., 1973. Factors affecting liquid-liquid relative permeabilities of a consolidated porous medium. *Soc. Petrol. Eng. J.* 13 (1), 39–47.
- Lemmon, E.W., Span, R., 2006. Short fundamental equations of state for 20 industrial fluids. *J. Chem. Eng. Data* 51 (3), 785–850.
- Li, C., Zhang, F., Lyu, C., Hao, J., Song, J., Zhang, S., 2016. Effects of H<sub>2</sub>S injection on the CO<sub>2</sub>-brine-sandstone interaction under 21 MPa and 70 °C. *Mar. Pollut. Bull.* 106 (1), 17–24.
- Li, H.L., Jakobsen, J.P., Wilhelmsen, Ø., Yan, J.Y., 2011. PVTxy properties of CO<sub>2</sub> mixtures relevant for CO<sub>2</sub> capture, transport and storage: review of available experimental data and theoretical models. *Appl. Energy* 88 (11), 3567–3579.
- Li, H., Yan, J., 2008. Impact of impurities in CO<sub>2</sub>-fluids on CO<sub>2</sub> transport process. In: *ASME Turbo Expo 2006: Power for Land, Sea, and Air*. Barcelona, Spain, pp. 367–375.
- Li, H., Yan, J., 2009a. Evaluating cubic equations of state for calculation of vapor-liquid equilibrium of CO<sub>2</sub> and CO<sub>2</sub>-mixtures for CO<sub>2</sub> capture and storage processes. *Appl. Energy* 86 (6), 826–836.
- Li, H., Yan, J., 2009b. Impacts of equations of state (EOS) and impurities on the volume calculation of CO<sub>2</sub> mixtures in the applications of CO<sub>2</sub> capture and storage (CCS) processes. *Appl. Energy* 86 (12), 2760–2770.
- Li, Q., Kuang, D., Liu, G., Liu, X., 2014. Acid gas injection: a suitability evaluation for sequestration site in Amu Darya Basin, Turkmenistan. *Geol. Rev.* 60 (5), 1133–1146.
- Li, Q., Li, X.C., Du, L., Liu, G.Z., Liu, X.H., Wei, N., 2012a. Potential sites and early opportunities of acid gas re-injection in China. In: Wu, Y., Carroll, J.J., Zhu, W. (Eds.), *Sour Gas and Related Technologies*. Wiley Scrivener, New York, USA, pp. 131–140.
- Li, Q., Liu, X., Du, L., Bai, B., Fang, Z., Jing, M., Li, X., 2013. Economics of acid gas reinjection with comparison to sulfur recovery in China. *Energy Proc.* 37, 2505–2510.
- Li, X.S., Boek, E., Maitland, G.C., Trusler, J.P.M., 2012b. Interfacial tension of (brines + CO<sub>2</sub>): (0.864 NaCl + 0.136 KCl) at temperatures between (298 and 448) K, pressures between (2 and 50) MPa, and total molalities of (1 to 5) mol·kg<sup>-1</sup>. *J. Chem. Eng. Data* 57 (4), 1078–1088.
- Liu, S.Y., Yang, X.N., Qin, Y., 2010. Molecular dynamics simulation of wetting behavior at CO<sub>2</sub>/water/solid interfaces. *Chin. Sci. Bull.* 55 (21), 2252–2257.
- Lorenz, P.B., Donaldson, E.C., Thomas, R.D., 1974. Use of Centrifugal Measurements of Wettability to Predict Oil Recovery. United States Department of the Interior, Bureau of Mines, Bartlesville Energy Research Center, Bartlesville, Oklahoma, USA.
- Ma, J.L., Li, Q., Kühn, M., Nakaten, N., 2018. Power-to-gas based subsurface energy storage: a review. *Renew. Sustain. Energy Rev.* 97, 478–496.
- Mahadevan, J., 2012. Comments on the paper titled “Contact angle measurements of CO<sub>2</sub>-water-quartz/calcite systems in the perspective of carbon sequestration”: a case of contamination? *Int. J. Greenh. Gas Control* 7, 261–262.
- Mantilla, I.D., Cristancho, D.E., Ejaz, S., Hall, K.R., Atilhan, M., Iglesias-Silva, G.A., 2010. P-ρ-T data for carbon dioxide from (310 to 450) K up to 160 MPa. *J. Chem. Eng. Data* 55 (11), 4611–4613.
- Mathias, S.A., Gluyas, J.G., González Martínez de Miguel, G.J., Bryant, S.L., Wilson, D., 2013. On relative permeability data uncertainty and CO<sub>2</sub> injectivity estimation for brine aquifers. *Int. J. Greenh. Gas Control* 12, 200–212.
- Matthew, R., 2006. *WebGasEOS 1.0 User Guide*. LBNL/PUB-3188, Lawrence Berkeley National Laboratory, Berkeley, CA, USA.
- McCaffery, F.G., Bennion, D.W., 1974. The effect of wettability on two-phase relative permeabilities. *J. Can. Petrol. Technol.* 13 (4), 42–53.
- McCaughan, J., Iglauer, S., Bresme, F., 2013. Molecular dynamics simulation of water/CO<sub>2</sub>-quartz interfacial properties: application to subsurface gas injection. *Energy Proc.* 37, 5387–5402.
- Miwa, M., Shiozawa, Y., Saito, Y., Tarmoom, I.O., 2002. Sour gas injection project. In: *10th Abu Dhabi International Petroleum Exhibition and Conference*. Society of Petroleum Engineers, pp. 1–11.
- Monastersky, R., 2013. Global carbon dioxide levels near worrisome milestone. *Nature* 497 (7447), 13–14.
- Morrow, N.R., 1970. Irreducible wetting-phase saturations in porous media. *Chem. Eng. Sci.* 25 (11), 1799–1815.
- Morrow, N.R., 1976. Capillary pressure correlations for uniformly wetted porous media. *J. Can. Petrol. Technol.* 15 (4), 49–69.
- Morrow, N.R., Cram, P.J., McCaffery, F.G., 1973. Displacement studies in dolomite with wettability control by octanoic acid. *Soc. Petrol. Eng. J.* 13 (4), 221–232.
- Morrow, N.R., Mungan, N., 1971. *Wettability and Capillarity in Porous Media*. Report RR-7. Petroleum Reservoir Research Institution, Calgary, Canada.
- Mungan, N., 1966. Interfacial effects in immiscible liquid-liquid displacement in porous media. *Soc. Petrol. Eng. J.* 6 (3), 247–253.
- Munkejord, S.T., Hammer, M., Løvseth, S.W., 2016. CO<sub>2</sub> transport: data and models - a review. *Appl. Energy* 169, 499–523.
- Mutailipu, M., Liu, Y., Jiang, L.L., Zhang, Y., 2019. Measurement and estimation of CO<sub>2</sub>-brine interfacial tension and rock wettability under CO<sub>2</sub> sub- and super-critical conditions. *J. Colloid Interface Sci.* 534, 605–617.

- Nazeri, M., Chapoy, A., Valtz, A., Coquelet, C., Tohidi, B., 2016. Densities and derived thermophysical properties of the 0.9505 CO<sub>2</sub> + 0.0495 H<sub>2</sub>S mixture from 273 K to 353 K and pressures up to 41 MPa. *Fluid Phase Equil.* 423, 156–171.
- Orr, F.M., 2007. *Theory of Gas Injection Processes*. Tie-Line Publications, Copenhagen, Denmark.
- Owens, W.W., Archer, D.L., 1971. The effect of rock wettability on oil-water relative permeability relationships. *J. Petrol. Technol.* 23 (7), 873–878.
- Patel, N.C., Teja, A.S., 1982. A new cubic equation of state for fluids and fluid mixtures. *Chem. Eng. Sci.* 37 (3), 463–473.
- Péneloux, A., Rauzy, E., Fréze, R., 1982. A consistent correction for Redlich-Kwong-Soave volumes. *Fluid Phase Equil.* 8 (1), 7–23.
- Peng, D.Y., Robinson, D.B., 1976. A new two-constant equation of state. *Ind. Eng. Chem. Fund.* 15 (1), 59–64.
- Pentland, C.H., El-Maghraby, R., Iglauer, S., Blunt, M.J., 2011. Measurements of the capillary trapping of supercritical carbon dioxide in Berea Sandstone. *Geophys. Res. Lett.* 38 (6), L06401.
- Pini, R., Benson, S.M., 2013. Simultaneous determination of capillary pressure and relative permeability curves from core-flooding experiments with various fluid pairs. *Water Resour. Res.* 49 (6), 3516–3530.
- Purcell, W.R., 1950. Interpretation of capillary pressure data. *J. Petrol. Technol.* 2 (8), 11–12.
- Quiñones-Cisneros, S.E., Schmidt, K.A.G., Giri, B.R., Blais, P., Marriott, R.A., 2012. Reference correlation for the viscosity surface of hydrogen sulfide. *J. Chem. Eng. Data* 57 (11), 3014–3018.
- Rahman, T., Lebedev, M., Barifcani, A., Iglauer, S., 2016. Residual trapping of supercritical CO<sub>2</sub> in oil-wet sandstone. *J. Colloid Interface Sci.* 469, 63–68.
- Redlich, O., Kwong, J.N.S., 1949. On the thermodynamics of solutions. V. An equation of state. *Fugacity of gaseous solutions*. *Chem. Rev.* 44 (1), 233–244.
- Sakoda, N., Uematsu, M., 2004. A thermodynamic property model for fluid phase hydrogen sulfide. *Int. J. Thermophys.* 25 (3), 709–737.
- Saraji, S., Goual, L., Piri, M., Plancher, H., 2013. Wettability of supercritical carbon dioxide/water/quartz systems: simultaneous measurement of contact angle and interfacial tension at reservoir conditions. *Langmuir* 29 (23), 6856–6866.
- Schaeff, H.T., McGrail, B.P., Owen, A.T., 2010. Carbonate mineralization of volcanic province basalts. *Int. J. Greenh. Gas Control* 4 (2), 249–261.
- Schaeff, H.T., McGrail, B.P., Owen, A.T., Arey, B.W., 2013. Mineralization of basalts in the CO<sub>2</sub>-H<sub>2</sub>O-H<sub>2</sub>S system. *Int. J. Greenh. Gas Control* 16 (4), 187–196.
- Schmidt, K.A.G., Quiñones-Cisneros, S.E., Carroll, J.J., Kvamme, B., 2008. Hydrogen sulfide viscosity modeling. *Energy Fuel* 22 (5), 3424–3434.
- Shah, V., Broseta, D., Mouronval, G., Montel, F., 2008a. Water/acid gas interfacial tensions and their impact on acid gas geological storage. *Int. J. Greenh. Gas Control* 2 (4), 594–604.
- Shah, V., Broseta, D.F., Mouronval, G., 2008b. Capillary alteration of caprocks by acid gases. In: *SPE Symposium on Improved Oil Recovery*. Society of Petroleum Engineers, Tulsa, Oklahoma, USA.
- Shen, P.P., Zhu, B., Li, X.B., Wu, Y.S., 2010. An experimental study of the influence of interfacial tension on water-oil two-phase relative permeability. *Transport Porous Media* 85 (2), 505–520.
- Shi, S.S., Belhaj, H., Bera, A., 2018. Capillary pressure and relative permeability correlations for transition zones of carbonate reservoirs. *J. Pet. Explor. Prod. Technol.* 8 (3), 767–784.
- Silin, D., Patzek, T., 2004. On barenblatt's model of spontaneous countercurrent imbibition. *Transport Porous Media* 54 (3), 297–322.
- Smith, S.A., Sorensen, J.A., Dobroskok, A.A., Jackson, B., Nimchuk, D., Steadman, E.N., Harju, J.A., 2008. Injection of Acid Gas (CO<sub>2</sub>/H<sub>2</sub>S) into a Devonian Pinnacle Reef at Zama, Alberta, for Enhanced Oil Recovery and Carbon Sequestration. 2008 Annual AAPG Convention. AAPG, San Antonio, TX, USA, pp. 1–11.
- Smith, S.A., Sorensen, J.A., Steadman, E.N., Harju, J.A., 2009. Acid gas injection and monitoring at the Zama oil field in Alberta, Canada: a case study in demonstration-scale carbon dioxide sequestration. *Energy Proc.* 1 (1), 1981–1988.
- Soave, G., 1972. Equilibrium constants from a modified Redlich-Kwong equation of state. *Chem. Eng. Sci.* 27 (6), 1197–1203.
- Sobocinski, D.P., Kurata, F., 1959. Heterogeneous phase equilibria of the hydrogen sulfide-carbon dioxide system. *AIChE J.* 5 (4), 545–551.
- Span, R., Wagner, W., 1996. A new equation of state for carbon dioxide covering the fluid region from the triple-point temperature to 1100 K at pressures up to 800 MPa. *J. Phys. Chem. Ref. Data* 25 (6), 1509–1596.
- Stopa, J., Lubas, J., Rychlicki, S., 2006. Underground Storage of Acid Gas in Poland - Experiences and Forecasts. 23rd World Gas Conference, Amsterdam, pp. 1–12.
- Stouffer, C.E., Kellerman, S.J., Hall, K.R., Holste, J.C., Gammon, B.E., Marsh, K.N., 2001. Densities of carbon dioxide + hydrogen sulfide mixtures from 220 K to 450 K at pressures up to 25 MPa. *J. Chem. Eng. Data* 46 (5), 1309–1318.
- Strathdee, G.G., Given, R.M., 1976. Adsorption of hydrogen sulfide at the aqueous solution interface. *J. Phys. Chem.* 80 (15), 1714–1719.
- Sutjiadi-Sia, Y., Jaeger, P., Eggers, R., 2008. Interfacial phenomena of aqueous systems in dense carbon dioxide. *J. Supercrit. Fluids* 46 (3), 272–279.
- Tadmor, R., 2004. Line energy and the relation between advancing, receding, and young contact angles. *Langmuir* 20 (18), 7659–7664.
- Talash, A.W., 1976. Experimental and calculated relative permeability data for systems containing tension additives. In: *SPE Improved Oil Recovery Symposium*. Society of Petroleum Engineers, Tulsa, Oklahoma, USA, pp. 1–12.
- Thomeer, J.H.M., 1960. Introduction of a pore geometrical factor defined by the capillary pressure curve. *J. Petrol. Technol.* 12 (3), 73–77.
- Torabzadey, S.J., Handy, L.L., 1984. The effect of temperature and interfacial tension on water/oil relative permeabilities of consolidated sands. In: *SPE Enhanced Oil Recovery Symposium*. Society of Petroleum Engineers, Tulsa, Oklahoma, USA.
- Trivedi, J.J., Babadagli, T., Lavoie, R.G., Nimchuk, D., 2005. Acid gas sequestration during tertiary oil recovery: optimal injection strategies and importance of operational parameters. In: *Canadian International Petroleum Conference*. Petroleum Society of Canada, Calgary, Alberta, Canada, pp. 1–17.
- Umeobi, H.I., Li, Q., Xu, L., Tan, Y., Onyekwena, C.C., 2021. Flow and structural analysis of sedimentary rocks by core flooding and nuclear magnetic resonance: a review. *Rev. Sci. Instrum.* 92 (7), 071501.
- Von Engelhardt, W., 1955. *Interstitial Water of Oil-Bearing Sands and Sandstones*. 4th World Petroleum Congress, Rome, Italy, pp. 399–416.
- Wei, Y.M., Kang, J.N., Liu, L.C., et al., 2021. A proposed global layout of carbon capture and storage in line with a 2 °C climate target. *Nat. Clim. Change* 11 (2), 112–118.
- Wesch, A., Dahmen, N., Ebert, K., Schön, J., 1997. Grenzflächenspannungen, tropfen-größen und kontaktwinkel im zweiphasensystem H<sub>2</sub>O/CO<sub>2</sub> bei Temperaturen von 298 bis 333 K und Drücken bis 30 MPa. *Chem. Ing. Tech.* 69 (7), 942–946.
- Wu, Y., Carroll, J.J., Li, Q., 2014. *Gas Injection for Disposal and Enhanced Recovery*. Hardcover ed. Wiley, New York, 2014.
- Xu, L., Li, Q., Myers, M., Chen, Q., Li, X., 2019. Application of nuclear magnetic resonance technology to carbon capture, utilization and storage: a review. *J. Rock Mech. Geotech. Eng.* 11 (4), 92–908.
- Yang, F., Bai, B.J., Tang, D.Z., Shari, D.N., David, W., 2010. Characteristics of CO<sub>2</sub> sequestration in saline aquifers. *Petrol. Sci.* 7 (1), 83–92.
- Young, T., 1805. III. An essay on the cohesion of fluids. *Phil. Trans. R. Soc.* 95, 65–87.
- Yu, T., Li, Q., Hu, H.X., Tan, Y.S., Xu, L., 2022. Molecular dynamics simulation of the interfacial wetting behavior of brine/sandstone with different salinities. *Colloids Surf. A Physicochem. Eng. Asp.* 632, 127807.
- Zhang, L., Hu, J.W., Guo, T., 2014. Evaluation of the pressure-volume-temperature (PVT) data of CO<sub>2</sub>. *Acta Geol. Sin. Engl.* 88, 1202–1203.
- Zhang, X.Y., Li, Q., Zheng, L.G., Li, X.Y., Xu, L., 2020. Numerical simulation and feasibility assessment of acid gas injection in a carbonate formation of the Tarim Basin, China. *Oil Gas Sci. Technol.* 75, 28.
- Zhang, Y., Li, H., Yang, D.Y., 2012. Simultaneous estimation of relative permeability and capillary pressure using ensemble-based history matching techniques. *Transport Porous Media* 94 (1), 259–276.
- Zhang, X.Y., Li, Q., Wei, X.C., 2021. Optimization of acid gas injection to improve solubility and residual trapping. *Greenhouse Gases: Sci. Technol.* 11 (5), 1001–1023.



**Xiaoyan Zhang** received her PhD in geotechnical engineering from Institute of Rock and Soil Mechanics, Chinese Academy of Sciences in 2022. She holds a B.Eng. degree in civil engineering from Wuhan University of Technology (2016), and a M.Eng. degree in architectural and civil engineering from Huazhong University of Science and Technology (2018). Her current research interests are focused on the percolation mechanism of multiphase fluid, multi-component reactive fluid flow and water-rock interaction associated with carbon dioxide capture, utilization and storage (CCUS).